MEMS RESONANT MASS SENSING WITH ENABLED OPTICAL INTERACTION FOR CELLULAR STUDY

Ethan Gary Keeler

A DISSERTATION
SUBMITTED IN PARTIAL FULLFILLMENT OF THE
REQUIREMENTS FOR THE DEGREE OF

DOCTOR OF PHILOSPHY

University of Washington
2018

READING COMMITTEE:
Lih Y. Lin (*Chair*)
Karl F. Böhringer
Jonathan T.C. Liu

PROGRAM AUTHORIZED TO OFFER DEGREE:

Department of Electrical Engineering

University of Washington

ABSTRACT

MEMS-Resonant Mass Sensing with Enabled Optical Interaction for Cellular Study

Ethan Gary Keeler

CHAIR OF SUPERVISORY COMMITTEE:
Professor Lih Y. Lin
Department of Electrical Engineering

The precision and mass sensitivity of nano- and micro-resonators is unmatched, revealing mechanical properties on progressively diminishing size-scales. Such lofty promises to deliver high resolution in robust and versatile applications require an equally precise method to observe and control nano- and micro-sized particles as they undergo mass and density characterization. This capability has profound implications in the fields of medicine and biology, in characterizing key parameters of the most basic unit of life, the cell. Observation of cell mass/density can answer many fundamental questions in biology and medical disease research, with the potential to investigate direct therapeutic interactions on the single-cell level and target rapid drug feedback. These meaningful results generally describe a distribution of measurements repeated for many cells over long experimental durations, where microfluidics can aid in serial sampling when integrated with resonant mass sensors. However, this fluidic environment is often isolated from

observation by the macro-scaled world, which imposes some critical challenges and limitations. Especially for repeated observations of samples with temporally-varying characteristics, sources of measurement error can defeat the resolution of small mass changes, indicative of cellular processes or perturbation effects. One such error source derives from the two-sided response of mass sensitivity in a resonator, involving both the position and mass of the added sample. Spatial fixation or careful observation of sample position can mitigate this effect for better measurement stability and repeatability. To this end, this dissertation investigates optical manipulation (trapping) and observation of particles and cells in fluid as a viable method to achieve better experimental fidelity and extend applications of this approach. Such a capability is not trivial; in fact, it imposes important challenges on both device and system development, and optical trapping itself mandates special design methods for integration with micro-electro-mechanical system (MEMS) mass-sensing platforms. With the introduction of manipulation, optical exposure becomes an especially important consideration when working with biological cells, organic matter, or other materials adversely affected by impinging high intensity laser light. Accordingly, inclusion of an integrated optical substrate (photonic crystal) can bolster high trap efficiency, and in this way, the devices can extend biological viability by reducing optical intensity, an important concern for experiments involving living cells. More global application of these devices also finds them compatible with other essential optical tools, such as fluorescence microscopy or flow cytometry. This work discloses design and fabrication development instrumental in uniting these important technologies, embodied by unique devices with maintained compatibility with MEMS processing. Accordingly, these devices demonstrate suitability for optical trapping, microscopy, and mass sensing, and the effects of optical manipulation on the measurement are disclosed, toward long-term biological mass monitoring and sensing.

Table of Contents

List of Figures

List of Tables

Acknowledgment

No research happens in the void of a vacuum—it is the culminated achievement from a collective of ideas and motivations, and no one gave me more footing in this endeavor than Professor Lin. I would like to thank her for her steadfast support and patience in times of success and most of all, during the aftermath of failures and delays. She has encouraged me every step of the way, with invaluable direction and feedback, and I cannot thank her enough for taking the risk on me as I journeyed to the PhD.

As yet another extension of her support, she assembled an incredible group of students, I am glad to call colleagues and friends. I would like to thank all the members of the Photonics Group, including Jingda Wu, Peifeng Jing, Chen Zou, Erin Sanehira, Conner Ballew, Yue Shi, and Matt Strathman. I would especially like to thank Peifeng for all of his assistance and foundational work on photonic-crystal mediated optical trapping; I would like to thank Jingda for teaching me the ins-and-outs of designing and building optical set-ups; and I would like to thank Chen for his help with electronic assembly and device characterization.

I would be remiss if I did not thank my undergraduate advisor, Professor Wataru Nakagawa, for his perpetual support and encouragement. Without his direction, I have no doubt the PhD would have been but a faint aspiration muddled by life and career. I owe him immensely for this strong research foundation and his illuminating guidance throughout my pursuit.

I recognize Professor Jonathan Liu, Professor Arvind Subramaniam, Professor Karl Böhringer, and Professor Suzie Pun for serving on my doctoral committee, and I cannot thank my

committee enough for taking time out of their busy schedules and accepting the associated responsibilities. I would specifically like to thank Professor Subramaniam for supplying our experiments with various cell types, and I would like to thank Professor Liu for extending his cell-culture facility for use in this research.

I would like to acknowledge the Washington Nanofabrication Facility for allowing me to toil endlessly in their well-maintained and well-equipped cleanroom. It was these capabilities that progressed this project from conceptual designs to real, physical devices, and I would certainly like to thank all of the staff for helping me work through numerous challenges.

I would like to recognize funding from the National Science Foundation for both our research grant (IDBR Program Grant No. DBI-1353718) and my graduate research fellowship (DGE-1256082).

Of course, I would not be writing this today without the unwavering support from my family and friends. They have shared in my successes and failures, and encouraged me in pursuance of all my dreams, no matter how lofty or untenable. In gratitude, I dedicate this dissertation to them:

To my parents,
deep-rooted in your selfless sacrifice,

To my family,
mediated by your strength,

To my friends,
inspired,

To Sara,
research fired by hope and love.

Chapter 1

Introduction

Silicon innovation has changed this world: its expansive versatility continues to mold our technological landscape, providing immense sensing, transduction, and computational power—becoming the cornerstone of many ubiquitous devices and systems available today. Silicon and derivative technologies underpin everything from medical devices to the internet of things (IoT).

Specifically in recent years, silicon and its fabrication methodologies have demonstrated great potential in bio-medical detection systems, integrated optics, and nano-scale technologies, and as a significant component of this progress, micro- and nano-electromechanical systems (MEMS, NEMS) have continued to prove their utility in numerous applications, realizing truly dynamic systems, especially given their complementary metal-oxide-semiconductor (CMOS) compatibility [1]. Of note, MEMS/NEMS resonant mass sensing devices, specifically cantilever and other beam structures, have seen impressive development over the past couple decades to the achievement of attogram [2] and zeptogram [3] resolutions toward single-molecule detection [4]. This class of devices has found especially important applications in biological characterization and sensing, through the use of bio-functionalized surfaces [5] [6] [7] and platforms capable of single cell and single bio-particle detection [7] [8] [9]. In stark contrast with other approaches, this technology does not necessitate labeling for detection, which can interfere with binding interactions or require prohibitive assays [8].

However, with the addition of mass labeling, this technology also promises direct recognition of pathogens including bacteria, viruses, and toxins.

By measuring resonant frequency shift in fine silicon structures, minute additions of mass or those mediated by changes in attached bio-samples can be readily observed, revealing important biophysical properties and processes. Biophysical characteristics at a cellular level can be indicative of human disease or abnormality [10]. For instance, the technology enables critical biological studies and can consider cell-growth size-dependency or unregulated growth applicable in understanding cancer mechanisms or those of other diseases [11]. One illustrative example is detection of circulating tumor cells in a cancer patient's blood exhibiting metastatic disease, which can indicate overall survival rate in cases of prostate, breast, colorectal, and certain lung cancers; specifically for ovarian cancer, these cells are challenging to detect with serum markers in early stage disease. These cells present with a decreased dry mass density compared to leukocytes, giving important insight into the disease [12]. This relationship between mass and cell growth is a fundamental question posed by biologists, and a high-resolution description could have great potential in medical detection and drug discovery, especially in a technological age that demands lab-on-a-chip capabilities.

A critical challenge for biological studies is maintaining physiological-support for the bio-material during measurement. Traditionally, MEMS sensors either operated in a fluid medium [13], or the samples were attached and dried [14] to enable sensing in air or vacuum. Operating in a liquid environment has a damping effect on the structural oscillation, generally leading to a degradation in the quality-factor (Q) and overall resonant-frequency measurement fidelity. Conversely, drying the material allows high-Q oscillation in air or vacuum environments, but prevents observation of life processes and real-time characterization. Burg *et al*. presented an elegant solution to this dichotomy by embedding a fluidic channel within a cantilever resonator, thereby operating the MEMS device in vacuum while suspending the bio-samples within the channel's inner fluid volume [6] [8] [15]. As mentioned, operating a MEMS resonant device in vacuum ensures

a high quality-factor, allowing for high-fidelity measurements of its natural frequency. Simultaneously, the fluidic channel provides a means to serially convey bio-samples onto the MEMS structure to conduct a continuous series of measurements in consideration of sample population or changing mass.

While the fluidic environment enables cell movement into and out of the device, it provokes measurement variability through added spatial complexity. Resonators can be highly sensitive to both added mass and its placement, giving rise to an empirically observed dependency [16]; furthermore, the mass sensitivity exhibits a linearly proportional relationship with the vibrational amplitude squared [17], which will be visited analytically in later chapters. This consequence encourages measurement error and uncertainty, and as resonant mass sensing technologies continue to pursue meaningful results on the resolution scales previously introduced, such consideration becomes progressively more essential. In the channel's fluid medium, the sample exhibits trajectory variance while propagating along the channel, leading to error in its perceived mass. The effect poses further challenges when exchanging the fluid medium of the channel, often required by pharmacology or other perturbation studies. Weng *et al.* describes using mechanical traps for this purpose [18]. However, these methods require physical interaction with the cell, typically necessitate pressure or flow changes that are susceptible to instability from pressure variations, and offer only temporary capture of the cell. Alternatively, optical trapping has been proposed as a solution [18] [19]; however, to our best knowledge, no developed platform has utilized this approach due to key challenges derived from multi-layered and complex fabrication flows that must integrate optically-clear materials for observation and manipulation (Figure 1.1 illustrates the concept).

In response to the prescribed literature void, this research investigates such a platform, incorporating optical trapping techniques into this powerful class of MEMS devices, and in this way, can readily capture and release cells. Optical trapping also promises the potential for long-term, precise monitoring of cells or temporally-varying particles by fixing their relative position, further enhancing accuracy and control in timed

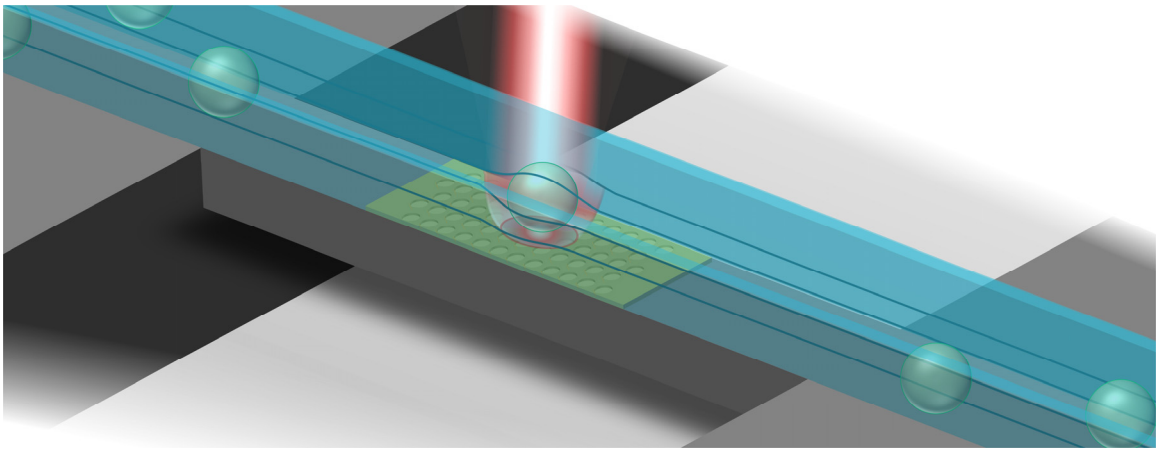

Figure 1.1. Illustration showing a MEMS bridge resonator with a PhC, the trapping/detection lasers, a trapped cell, and the fluidic channel.

experiments. Recent studies have targeted long-term characterization by measuring cell growth rates [17] [20] and monitoring cell response to therapeutics and interventions, but lacked a method of fine position control. The optical availability that trapping requires renders this an excellent platform for integrating other optical technologies including fluorescent imaging and flow cytometry.

Optical tweezers are accompanied by their own set of challenges: traditional optical trapping for biological studies is limited by the susceptibility of the target cells to damage from interaction with the required high-intensity laser light. Tinevez *et al.* found that even for fluorescence-based imaging, living specimens can experience phototoxicity or disruption from the excitation light source [21]. Clearly, the optical power necessitated for trapping can result in bio-material degradation, phototoxicity, and cell death over a short time span thereby reducing measurement utility; this outcome is attributed to the absorption of optical energy and cell heating [22]. Fortunately, the trapping force is directly related to the gradient of the intensity profile. While increasing the optical energy increases the trapping force, so does narrowing the intensity distribution. By using a photonic crystal (PhC) to modulate the intensity profile, the required laser energy can be significantly reduced along with the laser's threat to cell life [23]. With the photonic-crystal

enhancement employed in this work, the laser can position samples for longer durations for potential long-term bio-monitoring.

This dissertation will first address the current state-of-the-art in review of historical technologies and their evolution. In doing so, we will clarify the gap filled by this work. Then, by transitioning this concept of an optically-transparent mass sensor from first principles through design and simulation, we present the fabrication strategy and process flow that forged the path to final, realized structures. In validation of these devices, we describe performance evaluation and characterization of error, to the achievement of cell mass measurement, demonstrated trapping, and optical compatibility.

Chapter 2

Background

This section first reviews existing technologies and methodologies employed in characterizing single cells, broadly covering the various probing approaches. In isolating the technique that is foundational for this work, a detailed background is presented to discuss resonant structures and their utility in mass sensing. To this end, this chapter considers basic beam theory and extends it to position-dependent resonant sensing, in view of resolution and sensitivity. Finally, an overview of PhC-mediated optical trapping is presented along with the required compatibilities for MEMS technologies and optical system integration.

Section 2.1: Prior Arts

The measurement of mass has been an inspective parameter throughout the history of science, and as the targets for scientific inquiry and associated technologies continue to shrink, we must develop tools to keep pace. The need to understand characteristics on the single-cell, micron-particle, or even nano-scale level has driven important advancements over the past couple decades. Early attempts to understand simple cell types, including yeast and bacterial cells, employed impedance measurements and microscopy to observe changes in morphology. Impedance counters, such as the Coulter counter [24], and microscopy, including confocal laser scanning [25], can determine cell volume and have

delivered estimates of cell size; however, mass can better describe cell constitution and its constituent components, revealing more precise and meaningful cell information [26]. To fully understand these cellular processes, especially to quantify individual cell growth and its mechanisms, high precision and high throughput remain critical and characterizing specifications for this technology [11]. Popescu *et al.* enumerate the following key device criteria:

A) The mass measurement method should have a mass resolution less than 1 pg (1%), given that cells typically fall in the 100 – 1000 pg range;
B) The measurement apparatus should allow cell monitoring over a period of 20 hours to a few days, as cells double their mass over the course of 20 hours;
C) The measurement must separate changes in cell morphology from changes in mass; and
D) The throughput must reach a level of statistical significance with the capability to describe a population or variations among cells.

Besides these key developments, enabling technologies should be capable of sampling single cells or confluent populations in parallel, and they should also ensure compatibility with traditional microscopy techniques and fluorescence measurements to characterize morphology and bio-chemical composition. It is these requirements that spurred more advanced techniques, which employ MEMS technologies or sophisticated optical methods. The subsequent sections will survey several of these emerging technologies and review established methods.

Section 2.1.1: Electrical Probing

Focused on the rich information provided by red-blood-cell counting and sizing, in 1949 Coulter filed a patent [27] for a novel apparatus that provided fluid constriction

wherein suspended cells intersect an electrical current. The fluid generally comprises an electrolyte level sufficient to afford conductivity and correspondingly, a measurable current. As the cell passes into this region, it displaces the conductive medium and thereby induces a change in the circuit's impedance. Careful calibration of these impedance shifts yields a signal proportional to the cell volume and its surface area.

Since the inception of the Coulter counter, many configurations and commercialized systems matured as viable approaches for cell volume evaluation. In an attempt to miniaturize the method and extend its applications, Koch *et al.* developed a micromachined implementation utilizing silicon trenching and subsequent electrode deposition to produce a Coulter counter [28]. While informative, it does have limits as this technique requires special experimental conditions and assumes that the suspended cells are spherically shaped [29].

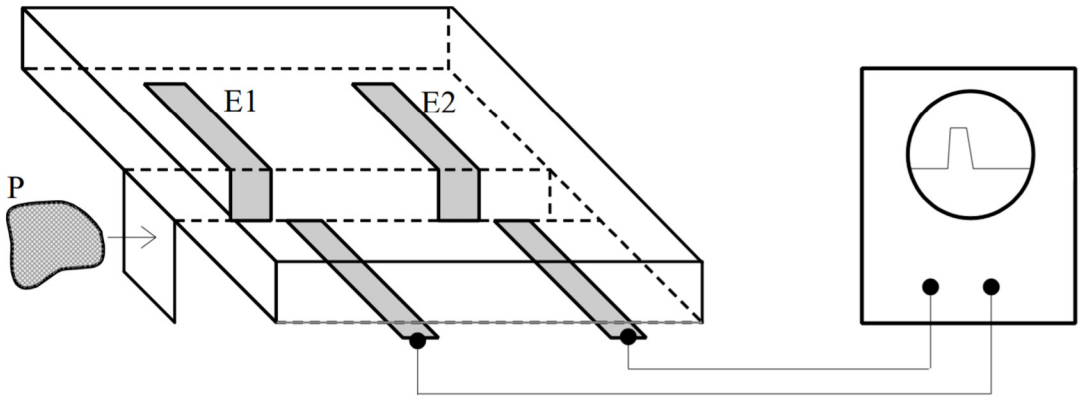

Figure 2.1. Micromachined Coulter counter schematic showing a sample, a trench, and two electrodes. [28] [Adapted with permission from the Institute of Physics Publishing.]

By extending this to other electrical characteristics, developed methods have instead observed the capacitance across the cell membrane. The scientific community has generally accepted that most cells exhibit a specific membrane capacitance in the range of

0.5–1.0 μF/cm^2 [30]. By observing the time constant of the measured voltage response, one can estimate the total capacitance and derive the cell's surface area, and volume by extension, assuming knowledge of its specific capacitance [31] [32]. This method requires isopotential cells, which can be an exclusive requirement for some biological investigations, especially regarding neurons, and can also depend on cell shape and configuration.

Korchev *et al.* envisioned a method that could accommodate arbitrary cell shapes with less imposing experimental conditions. To this end, they utilized a micropipette that could determine cell height over a varied profile enabled by a precision three-axis stage. The proximity of the probe to the cell's membrane controlled measured ion flow, with decreasing signal as the probe contacted the cell surface. By feedback-controlled scanning, the technique could map cell surface and estimate its volume [29]. This technique can give a very detailed contour of the cell, but is challenged by sample suspension and requires an appreciable scan time.

These measurement modalities can analyze cell volume and surface area and can certainly serve to distinguish cell types and provide informative parameters on a global perspective, but they lack the precision to determine changing composition within the cell.

Section 2.1.2: Optical Methods

Fluorescence imaging and confocal microscopy have served as pillars in biological research, illuminating the world on the single- and sub-cellular levels. Among their many important utilities, these methods can characterize cells with high resolution, and it is not a far stretch to implicate the techniques in cell volume and growth analysis [33] [34]. Satoh *et al.* employed confocal sectioning of a cell over its entire volume, producing a stack of cellular fluorescence images [35]. Analysis of these images and ensuing reconstruction yielded three-dimensional representations of the cell, to reveal its volume and to consider the relationship between cell volume and membrane capacitance.

Aside from probing cells through microscopy and fluorescence imaging, purely optical methods generally rely on the relationship between cell concentration and refractive index. In general, this relationship proves a linear trend, termed the specific refractive increment. Therefore, the retrieval of a cell's refractive index distribution can map the cell's dry mass (m) through the relation [36]:

$$m = \frac{1}{\alpha}\iint \phi \cdot \lambda \cdot dA \tag{2.1}$$

where α is the specific refractive increment (dn/dc); ϕ represents the measured phase shift; and λ is the interrogation wavelength. This method has found useful applications in observing pluripotent stem cells [37] and single and colonized breast cancer cells [38]. While interference is known as an extremely accurate technique to measure phase shift and refractive index, this approach is highly dependent on the specific refractive increment value linking the measurement to concentration and mass.

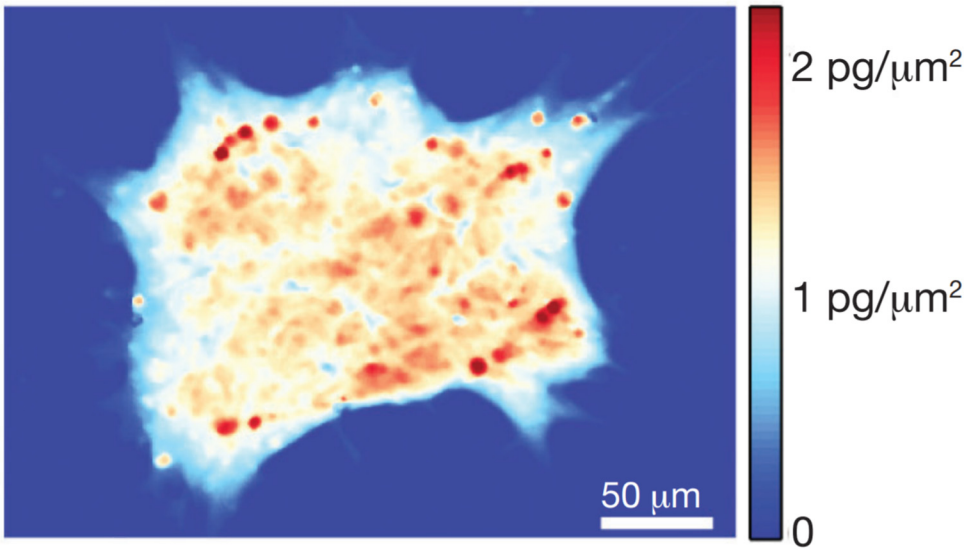

Figure 2.2. Mass measurement of a multicellular human pluripotent stem cell colony utilizing phase-shifting interferometry. [36] [Reprinted with permission from Springer Nature.]

On a final note, evanescent wave sensing has proven a viable avenue for biomolecular and cellular detection [39] as has surface plasmon resonance sensing [40]. These devices have very high sensitivity; however, their measurement extent is limited to thin layers of biomaterial or shallow cell penetration.

Section 2.1.3: Mechanical Technologies

Since mass and mechanical motion share an intimate coupling, technological feasibility was the only obstacle to its implementation on the cellular- or protein-size scale. One common approach that emerged in this arena was the quartz crystal microbalance (QCM) that utilizes the piezo-electric effect in certain solid materials where an applied electrical field can induce a mechanical strain in the material. Modulation of this applied field establishes a resonant oscillation within the crystal; the addition of mass to its surface, causing a change of thickness, induces a resolvable shift in the oscillation, thereby providing a means for measurement. Marx *et al.* employed such a sensor while observing the attachment of living endothelial cells and imposed drug effects [41]. QCM can serve as a great vehicle for label-free detection [42] [43]; however, miniaturization and batch processing pose notable challenges for this technology [6].

In its infancy, the field of resonant silicon sensors started with force [44], flow [45], and pressure transducers [46], and it has observed tremendous growth over the past fifty years. With modern fabrication capabilities and novel applications, MEMS have proven an excellent platform for cell analysis and detection. This foundation spurred two notable resonant structures, each offering different strengths.

As briefly introduced, Burg *et al.* cleverly integrated a fluidic channel within a silicon cantilever device, offering both the benefits of operation in a vacuum environment as well as the integration of a fluidic chamber to support cell life and convey targets onto and off of the resonant structure.

Figure 2.3 illustrates the structure concept of the suspended micro-channel, with resonant shifting either by molecule binding through immobilized receptors or observations of a discrete mass navigating the cantilever channel [8]. This device boasts the highest mass sensitivity, capable of resolving 0.05% of a cell's buoyant mass (dry mass) [11] on femtogram levels.

This device is not infallible, however. Due to a swift change in the vibration profile of the cantilever as traversed from base to tip, position of the sample mass has a significant influence on the mass measurement. For these particular devices, consisting of 8-µm channel widths, experiments observed an 8% larger frequency shift for cells following the centerline versus the wall of the channel. This especially becomes a compounding problem with dynamic trapping. By alternating the direction of fluid flow, a single particle can travel back and forth across the cantilever tip to achieve temporal measurements. This uncertainty broadens the data for a population and can lead to degraded resolution or inaccurate conclusions [47].

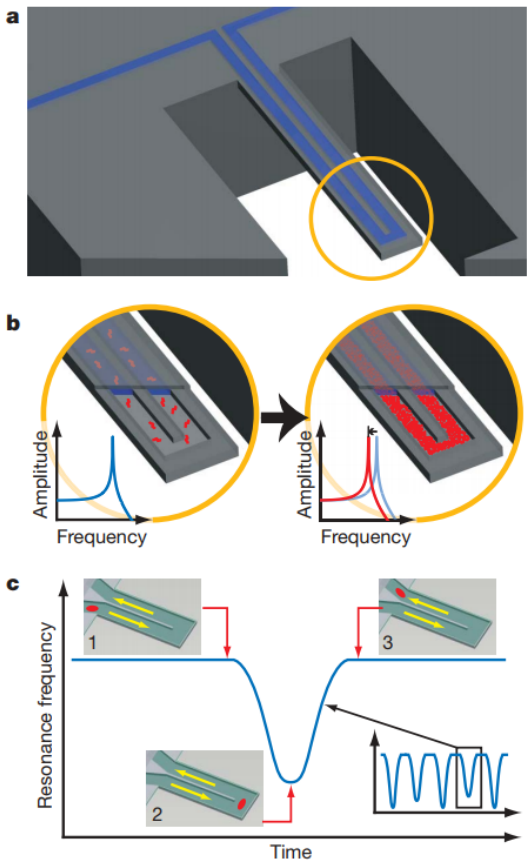

Figure 2.3. (A) An Illustration of the cantilever device with an embedded fluidic channel. (B) A Frequency shift induced by binding to immobilized receptors. (C) The time series measurement of an unbound particle traversing the channel, where the peak frequency dictates the measured mass. [7] [Reprinted with permission from Springer Nature.]

As briefly introduced, researchers have considered methods to alleviate this constraint by employing mechanical traps [18], comprising various hydrodynamic configurations and embedded physical structures within the channel. While offering some control over sample position, these approaches can exhibit instability with mechanically invasive treatment of the cell. Since the lateral displacement along the tip poses the greatest consequence, efforts have considered utilizing the second resonant mode of the cantilever, where displacement across the channel width has little to no effect at the structure's antinodes away from the apex of the cantilever. The findings of this work showed that there was a trade-off between the precision of higher-mode sensing and mass resolution for specific frequency ranges. Additionally, higher-mode operation achieved lower quality-factors than fundamental mode operation due the unique fluid damping mechanisms observed by these devices [48].

Park *et al.* sought to engineer a device to directly observe adherent mammalian cell growth rates and mass in longer-term experiments by culturing cells on cantilever arrays [49]. Subsequently, with the target of human colorectal carcinoma cells (HT29), the group developed a novel resonant pedestal design that promised far better mass uniformity than observed for the cantilever-class devices [17]. Figure 2.4(A) shows a simulation comparing the mass uniformity for the pedestal and cantilever devices, with the latter demonstrating an error greater than 100%, and the former experiencing only a variation less than 4%. Figure 2.4(B) and Figure 2.4(C) show a scanning electron microscope (SEM) image and a schematic of the measurement setup comprising the pedestal device, with an illustrated shift in the resonator's frequency response.

The device operated with a magnetic Lorentz-force drive to allow submersion into fluid, enabling cell culture on the structure for living-cell assessment. While accurate and long-term qualified, a core challenge for this technology is throughput, since there is no controlled means by which to convey cells onto and off of the structure for the commencement or termination of experiments. To consider a larger sample population, the approach instead requires an array of sensors for parallel monitoring.

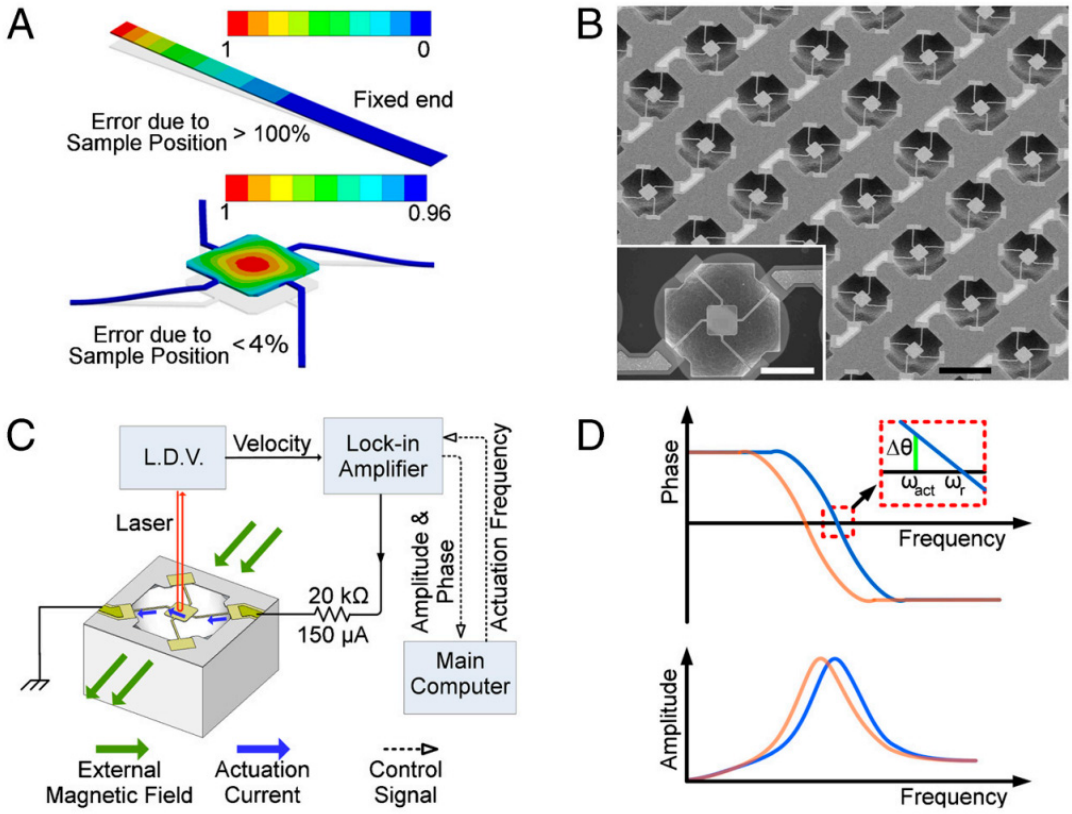

Figure 2.4. (A) Comparison of positional error between the novel pedestal design and a conventional cantilever; (B) SEM image of the pedestal sensor array; (C) diagram of the measurement setup; and (D) phase and amplitude response versus frequency. [17]

Section 2.2: Resonant Beam Principles

To gain insight into the underpinning beam mechanics of positional variance, one can look to classical Euler-Bernoulli beam theory to consider bending effects in a transversely vibrating beam [50] [51]. The Euler-Bernoulli theory excludes shear distortion effects and rotation of the cross-section and as a result can overestimate the structure's natural frequency; however, the theory can give a first order picture of resonant position dependency.

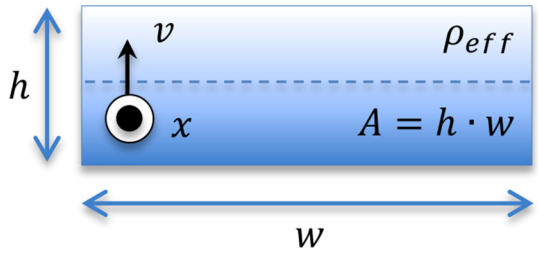

Figure 2.5. Properties and dimensions of the beam under consideration.

Consider a beam of dimensions L, w, and h with a cross-sectional area A (as depicted in Figure 2.5). To study the effects of added mass, we will define an effective beam density ρ_{eff} to include an added mass term, which is uniformly distributed over the entire solid for simplification:

$$\rho_{eff} = \rho + \frac{m_{eff}}{A \cdot L} \tag{2.2}$$

The effective mass can be represented in the following expression where m is the actual added mass, and $\alpha(x_o)$ is a spatially dependent parameter at $x = x_o$ that we will revisit further on.

$$m_{eff} = m + \alpha(x_o) \cdot m \tag{2.3}$$

The potential energy due to beam bending is given by:

$$PE = \frac{1}{2}\int_0^L E \cdot I \cdot \left(\frac{\partial^2 v(x,t)}{\partial x^2}\right)^2 dx \tag{2.4}$$

where E is the Young's modulus; I is the area moment of inertia; v is the transverse deflection; and x points axially along the beam. Analogously, the kinetic energy takes the form:

$$KE = \frac{1}{2}\int_0^L \rho_{eff} \cdot A \cdot \left(\frac{\partial v(x,t)}{\partial t}\right)^2 dx \tag{2.5}$$

The third contributing component is load $F(x)$, which does work to introduce energy to the system:

$$W = \int_0^L F(x) \cdot \Delta v(x,t)\, dx \tag{2.6}$$

Together, these terms form the Lagrangian equation:

$$S = \int_0^L \left[F(x) \cdot \Delta v(x,t) + \frac{1}{2} A \rho_{eff} \left(\frac{\partial v(x,t)}{\partial t} \right)^2 - \frac{1}{2} EI \left(\frac{\partial^2 v(x,t)}{\partial x^2} \right)^2 \right] dx \tag{2.7}$$

$$\mathcal{L}(t, x, v, \dot{v}, v_{xx}) \equiv F(x) \cdot \Delta v(x,t) + \frac{1}{2} A \rho_{eff} \cdot \dot{v}^2 - \frac{1}{2} EI \cdot {v_{xx}}^2 \tag{2.8}$$

The solution to this equation seeks to minimize the functional S according to Hamilton's principle, and the partial differential equation can be found as:

$$\frac{\partial \mathcal{L}}{\partial v} - \frac{\partial}{\partial t}\left(\frac{\partial \mathcal{L}}{\partial \dot{v}} \right) + \frac{\partial^2}{\partial x^2}\left(\frac{\partial \mathcal{L}}{\partial v_{xx}} \right) = 0 \tag{2.9}$$

$$F(x) - \frac{\partial}{\partial t}\left(\rho_{eff} \cdot A \cdot \dot{v} \right) - \frac{\partial^2}{\partial x^2}\left(EI \cdot v_{xx} \right) = 0 \tag{2.10}$$

$$F(x) - A \rho_{eff} \frac{\partial^2 v(x,t)}{\partial t^2} - EI \frac{\partial^4 v(x,t)}{\partial x^4} = 0 \tag{2.11}$$

The clamped-clamped beam structure introduced previously cannot deflect or rotate at its extremes, and its two-ended boundary conditions take the form of Equation (2.12).

$$v = 0; \quad \frac{\partial v}{\partial x} = 0 \tag{2.12}$$

We can arrive at an analytical solution by separation of variables and an assumed solution form:

$$v(x,t) = W(x) \cdot T(t) \tag{2.13}$$

where $T(t)$ describes the frequency response of the beam vibration in terms of the frequency ω:

$$T(t) = e^{j\omega t} \tag{2.14}$$

If we consider a free beam ($F(x) = 0$), the equation describing deflection and spatial characteristics becomes:

$$\frac{\partial^4 W(x)}{\partial x^4} - a^4 \cdot W(x) = 0 \tag{2.15}$$

$$a^4 = \frac{A \cdot \rho_{eff} \cdot \omega^2}{EI} \tag{2.16}$$

To solve the differential equation, we know that the solution comprises both non-hyperbolic and hyperbolic sines and cosines (with coefficients C_1, C_2, C_3, and C_4):

$$W(x) = C_1 \sinh(a \cdot x) + C_2 \cosh(a \cdot x) + C_3 \sin(a \cdot x) + C_4 \cos(a \cdot x) \tag{2.17}$$

Solving for these coefficients will deliver insight into the modal shapes of the clamped-clamped beam by utilizing the previously enumerated boundary conditions. However, the particular solution for this boundary-valued problem is beyond the scope of this analysis; instead, Figure 2.6 shows the shape of the first four modes for the clamped-clamped beam.

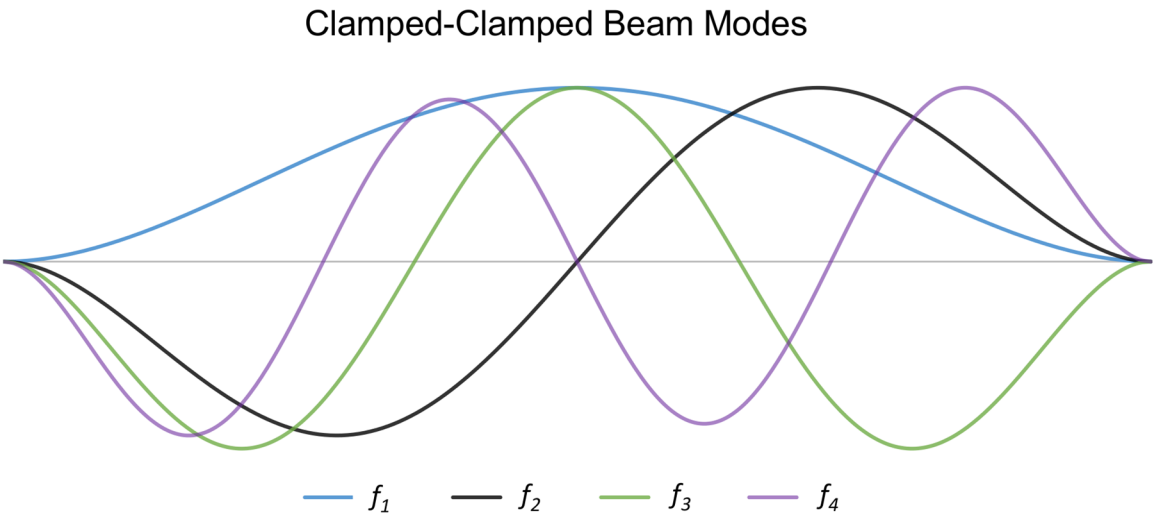

Figure 2.6. The four lowest modal shapes for the clamped-clamped beam configuration. The lowest natural frequency is the main concern in this work.

More importantly, we must review the eigenvalues of the system to understand the effect of mass placement. Finding the coefficients can arrive at the characteristic equation through calculation of the determinant:

$$\begin{bmatrix} \sinh(a \cdot L) - \sin(a \cdot L) & \cosh(a \cdot L) - cos(a \cdot L) \\ \cosh(a \cdot L) - \cos(a \cdot L) & \sinh(a \cdot L) + \sin(a \cdot L) \end{bmatrix} \begin{bmatrix} C_1 \\ C_2 \end{bmatrix} = \begin{bmatrix} 0 \\ 0 \end{bmatrix} \tag{2.18}$$

thereby obtaining the following equation with its first four corresponding solutions:

$$\cosh(a \cdot L) \cdot \cos(a \cdot L) = 1$$

$$\begin{aligned} a_1 \cdot L &= 4.73 \\ a_2 \cdot L &= 7.85 \\ a_3 \cdot L &= 11.00 \\ a_4 \cdot L &= 14.14 \\ &\vdots \end{aligned} \tag{2.19}$$

Therefore, we can determine the natural frequencies of the structure with the result given in Equation (2.20). Generalizing for a moment, a resonant sensor exploits perturbations to resonant system equilibrium in order to induce a measurable resonant frequency shift that has a well-defined relationship with the perturbation, encompassing a change in the system's chemical or physical parameters [52]. In this particular case, a change in mass leads to a shift in the resonant frequency. Here we understand the resonant frequency f_n of the structure is a function of its stiffness k and its mass m. To measure mass as a result of a resonant frequency shift, it is important to decouple the stiffness and mass of the structure when probing the sample, based on beam configuration and mass position.

$$f_n = \frac{1}{2\pi}\sqrt{\frac{E \cdot I \cdot {a_n}^4}{A \cdot \rho_{eff}}} = \frac{1}{2\pi}\sqrt{\frac{k}{m + \alpha(x_o) \cdot \Delta m}} \tag{2.20}$$

By differentiating Equation (2.20) with respect to mass, we can obtain an approximately linear relationship between mass and frequency change for small variations, shown in Equation (2.23).

$$\frac{df_n}{dm} = -\frac{1}{4\pi}\sqrt{k} \cdot (m)^{-\frac{3}{2}} \tag{2.21}$$

Around the operating point $m = m_o$, we can simplify, if we enforce only small changes in mass, i.e. $m_o + \Delta m \approx m_o$:

$$\sqrt{k} = 2\pi \cdot \sqrt{m_o} \cdot f_o \tag{2.22}$$

$$\frac{\Delta f_n}{f_o} \approx -\frac{1}{2}\frac{\Delta m}{m_o} \tag{2.23}$$

With a similar treatment we can now consider a mass m at a point $x = x_o$, and the resulting values of m_{eff} and ρ_{eff}. In order to determine the effective mass experienced by the system, we must study the kinetic and potential energy of the added mass. If we assume an ideal structure, absent of damping and energy dissipation, it is important to note that:

$$KE + PE = constant = C \tag{2.24}$$

From this relation, we can write the following expression for the added mass by observing that potential energy derives from the work done on the mass by the system:

$$\frac{1}{2} m_{eff} \left(\frac{dv(x_o,t)}{dt} \right)^2 + \int m_{eff} \frac{d^2 v(x_o,t)}{dt^2} \cdot \frac{dv(x_o,t)}{dt} dt = C \tag{2.25}$$

$$m_{eff} = m[1 + \alpha(x_o)] = C \left[\frac{1}{2} \left(\frac{dv(x_o,t)}{dt} \right)^2 + \int \frac{d^2 v(x_o,t)}{dt^2} \cdot \frac{dv(x_o,t)}{dt} dt \right]^{-1} \tag{2.26}$$

$$\alpha(x_o) = \frac{C}{m} \left[\frac{1}{2} \left(\frac{dv(x_o,t)}{dt} \right)^2 + \int \frac{d^2 v(x_o,t)}{dt^2} \cdot \frac{dv(x_o,t)}{dt} dt \right]^{-1} + 1 \tag{2.27}$$

This formulation shows that α varies on the interval $[0, L]$ as function of x_o, contributing an effective mass to the system. Clearly, the mass's placement can suppress or enhance its contribution to the system's resonant frequency.

Section 2.3: Mass Sensing

Of course, the devices presented in this work involve more than just a simple beam with its constituent mass. For fluid assisted devices that incorporate a channel for introduction of samples under test, the response has a dependency on several additional

dynamic parameters. In addition to the structure itself, overall mass includes both the fluid and the sample producing a total effective mass:

$$m^* = m^*_{structure} + m^*_{fluid} + m^*_{sample} \tag{2.28}$$

Each mass carries with it a qualified contribution to the structure's resonant frequency that is determined by distribution and material properties. If we assume that the mass of the structure remains unchanged during an experiment and it is an isolated system, we must consider the dynamic between the sample and its suspension fluid. In a general formulation for a volume (V) of two materials with densities d_{sample} and d_{fluid}, we have a difference in mass:

$$\Delta m = V \cdot d_{sample} - V \cdot d_{fluid} \tag{2.29}$$

This expression represents a phenomenon that is very familiar, as it implies the buoyant force that occurs when fluids become subjected to a gravitational field. In terms of mass sensing (for small fluctuations), this difference in mass (Δm) is the calculated parameter measured by frequency shift. Sensitivity relates resonant frequency to mass change by a proportionality constant (s), defined as:

$$s = \frac{\Delta f}{\Delta m} \approx -\frac{1}{2}\frac{f_o}{m_o} \ \left[{}^{Hz}/_{pg}\right] \tag{2.30}$$

This illuminating relationship shows very clearly that high resonant frequency improves sensitivity, whereas increased structure mass degrades it. We can now rewrite Equation (2.29) in the following way:

$$\Delta m = \Delta f \cdot s = V \cdot d_{sample} - V \cdot d_{fluid} \tag{2.31}$$

This relationship is very useful for observation of dynamic mass change in the sample; however, as will become clear, absolute mass (m) determination requires either additional measurement/assumptions or special conditions. For absolute mass, we can reformulate the expression:

$$m = \Delta f \cdot s + V \cdot d_{fluid} \tag{2.32}$$

This is a simple, yet important, formula that requires not only a measurement of resonant frequency shift and a calibration on sensitivity, but it mandates accurate knowledge of both the volume of the sample (which is simultaneously the volume of the displaced fluid) and the fluid's density.

In the particular case of cell mass sensing in the presence of water/media, these assumptions/prior knowledge are not necessary to measure the cell's "dry mass" (m_{dry}). Since cells consist of a membrane which encloses both fluid and constituent materials, an important parameter is their weight excluding contributions from water (or more specifically the cell media). This measurement gives good insight into growth and development of the cell and its cellular structures. In this case, fluid-integrated resonators can measure dry mass without additional measurements/assumptions:

$$\Delta m = \Delta f \cdot s = V \cdot d_{cell} - V \cdot d_{media} \tag{2.33}$$

$$\Delta m = V(d_{cell} - d_{media}) \tag{2.34}$$

$$\Delta m = V\left(\left(d_{dry} + d_{media}\right) - d_{media}\right) \tag{2.35}$$

$$\Delta f \cdot s = V d_{dry} = m_{dry} \tag{2.36}$$

This result substantiates the capability to detect the dry mass of a cell without prior knowledge of the cell's volume or the density of water. It is important to note that this

approach is only valid if the fluid density inside of the cell reaches an equilibrium with the external medium. If a significant difference exists, the generalized approach discussed by Equation (2.36) is more appropriate, which more formally takes the form:

$$m_{dry} = \Delta f \cdot s - V(d_{fluid} - d_{media}) \tag{2.37}$$

Even further, instead of measuring mass by making assumptions or explicit measurements of the volume, the sample can be suspended in two solutions with differing densities [53]. This could readily be enabled by optical positioning of the cell and exchanging the fluid, requiring very precise control of the fluid and its drag force. Still assuming a linear response to mass, measurement of cell density (d_{cell}) can be made according to the following expression, involving the density difference (Δd) between the first fluid (d_{f1}) followed by the density of the second (d_{f2}), the cell volume (V_{cell}), and the measured change in mass ($\Delta m_d = m_2 - m_1 = \Delta f_2 \cdot s - \Delta f_1 \cdot s$) between solutions:

$$d_{cell} = d_1 - m_1\left(\frac{\Delta d}{\Delta m_d}\right) \tag{2.38}$$

In a complementary result, the absolute mass of the cell can be determined by the relationship:

$$m_{cell} = m_1 - d_1\left(\frac{\Delta m_d}{\Delta d}\right) \tag{2.39}$$

Pursuant to this relationship between fluid density and perceived mass, if we take the derivative of Equation (2.37) with respect to fluid density, we find that the rate of change in determined mass is dependent on the volume of the cell. In this way, the volume of the cell can be determined by Equation (2.40).

$$V_{cell} = \left|\frac{\Delta m_d}{\Delta d}\right| \tag{2.40}$$

These relationships derive from the linear relation between mass and density, and their effect on the resonant frequency of the structure. Figure 2.7 illustrates this linear association, where the y-intercept yields cell mass, the x-intercept describes cell density, and the slope of the line delivers information about the cell volume. From these equations and figures, measurements with varying density can reveal multiple parameters for the cell or sample.

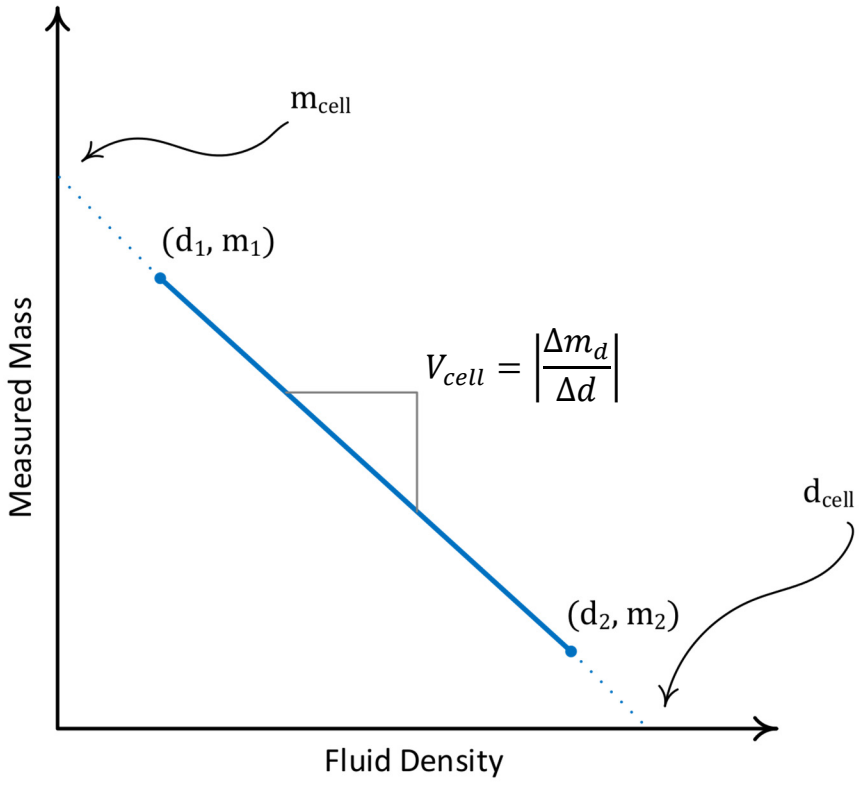

Figure 2.7. Two sample-mass measurements (from observation of resonant frequency change and knowledge of device sensitivity) at different fluid densities. With this information, the volume, actual cell mass, and density of the cell can be determined.

Of course, these mass measurements are highly dependent on cell position. With assumptions that the mode-shape remains unaffected by the additional mass m, the relationship for device sensitivity at a point x_o along the structure can be approximated [54]:

$$s(x_o) = \frac{2\pi f_o}{m}\left(\sqrt{1 + v(x_o)\cdot\frac{m}{m_o}}^{-1} - 1\right) \tag{2.41}$$

Section 2.5: Structural Damping and Resolution

Optical trapping can ensure measurement precision, but the final resolution of the system is a product of numerous working fragments, including the electronic/optical detection method, the electrostatic drive, and the resonator itself. The resonator exhibits behavior described by a harmonic oscillator, derived classically from Newton's second law of motion (neglecting other external forces):

$$m\frac{d^2x}{dt^2} = \sum F = -c\frac{dx}{dt} - kx - F_{actuation} \tag{2.42}$$

where c represents damping from internal or external processes that exhibits proportionality to speed; m introduces mass; k is the stiffness parameter for the restoring force on the oscillator; and x is the displacement of the resonator. In a more applicable representation, the equation can be recast in terms of its frequency characteristics:

$$\frac{d^2x}{dt^2} + \frac{\omega_o}{Q}\frac{dx}{dt} + {\omega_o}^2 x = {-F_{actuation}}/{m} \tag{2.43}$$

As discussed in Section 2.2: Resonant Beam Principles, the solution describing the resultant harmonic response involves a magnitude and phase component. Using this understanding to solve Equation (2.43) obtains the transfer function for the resonator shown in Equation (2.46).

$$x(t) = A(f) \cdot e^{j \cdot 2\pi f \cdot t} \tag{2.44}$$

$$F_{actuation} = F \cdot e^{j \cdot 2\pi f \cdot t} \tag{2.45}$$

$$H(f) = \frac{A(f)}{F} = \frac{C \cdot {f_o}^2}{{f_o}^2 + f\frac{f_o}{Q}j - f^2} \tag{2.46}$$

$$|H(f)| = \left|\frac{A(f)}{F}\right| = \frac{C \cdot {f_o}^2}{\sqrt{\left({f_o}^2 - f^2\right)^2 + \left(\frac{f_o}{Q} \cdot f\right)^2}} \tag{2.47}$$

where f is the forcing frequency; f_o is the natural frequency; Q is the quality factor of the resonator; and C is a scaling parameter based on the mass, stiffness, and the driving force. This equation is important in fitting measurement data for more accurate parameter estimation.

Regarding the characteristics of the resonator, the quality-factor Q is a description of the purity with which the resonator oscillates around its natural frequency. As Q increases, the damping term in Equation (2.46) diminishes. It is this term, together with the many damping sources of the system, that dictate the frequency-bandwidth in the structure's frequency response:

$$Q = \frac{f_r}{\Delta f_{bandwidth}} \tag{2.48}$$

One can also define the quality-factor in terms of its ability to store energy, as it continually transfers it back-and-forth between kinetic and potential energy. By taking the ratio of the energy stored to the energy dissipated with each cycle [55], the resulting expression clearly conveys the effect that damping has on the Q-factor: as opposing forces draw energy away from the resonator, its quality-factor diminishes.

$$Q = 2\pi \cdot \frac{energy\ stored}{energy\ dissipated\ per\ cycle} \tag{2.49}$$

To better illustrate the importance of the structural quality-factor, Figure 2.8 shows a set of frequency responses with increasing Q. It becomes clear from the figure, that a high Q-factor ensures high-fidelity determination of the structure's resonant frequency, with a highly filtered, pure output, and a low Q-factor introduces considerable noise into the measurement. With adequate detection frequency stability and bandwidth considerations, the Q-factor has a dominating effect on the system's ability to resolve frequency shifts, and thereby restricts observation of changing mass on the structure.

There are many underpinning mechanisms that lead to damping or energy loss from the structure. Virtually all external interactions lead to an energy exchange, accompanied by intrinsic and internal effects. Air damping, both viscous and squeeze-film, is a significant energy dissipation mechanism at this size scale and can severely limit the quality of the resonator. To mitigate this effect, a vacuum environment proves essential to device performance, ensuring desirable stability and frequency-fidelity characteristics. In an adequate vacuum environment, other effects become significant including losses to the supporting structure through anchor points, thermo-elastic damping (TED) caused by irreversible heat flow within the structure (internal friction), and surface losses [56]. These internal loss mechanisms can become especially significant for composite structures, at the

interface between materials with differing properties. There is certainly a trade-off that exists when using composite structures for additional functionality, such as optical integration, when compared with the performance of pure, high-quality materials, such as single-crystalline silicon. The overall quality factor is comprised of many dissipative mechanisms and can be easily dominated by the most offending [57]:

$$\frac{1}{Q} = \frac{1}{Q_{air}} + \frac{1}{Q_{anchor}} + \frac{1}{Q_{TED}} + \frac{1}{Q_{surface}} + \cdots \tag{2.50}$$

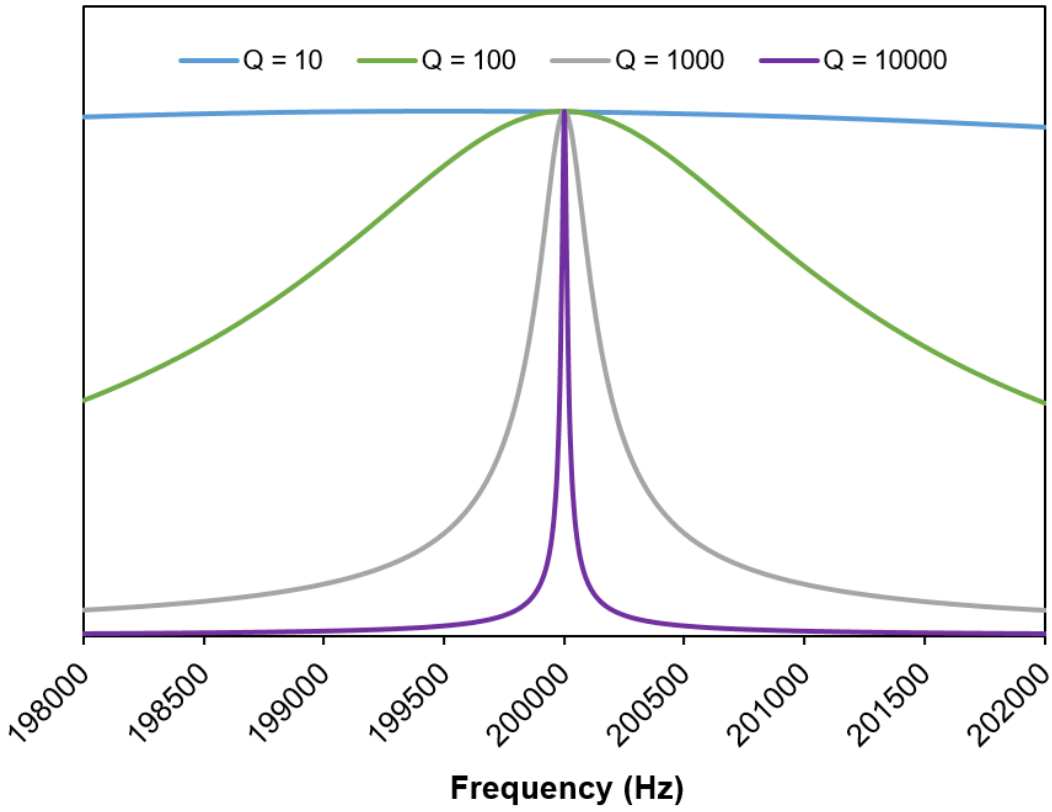

Figure 2.8. Normalized frequency response for a damped harmonic oscillator with a swept Q-factor value. Higher Q-factors clearly convey sharp definition of the resonant frequency.

Fortunately, the value of the mechanical quality-factor (determined by the structure and its physical interaction with external factors) by itself is not the ultimate limit to device performance. When utilized in a system that employs closed-loop feedback, such as that depicted in Figure 2.9, the topology can drive the resonator to an effective Q_{eff}, thereby increasing the mechanical quality-factor by several orders of magnitude.

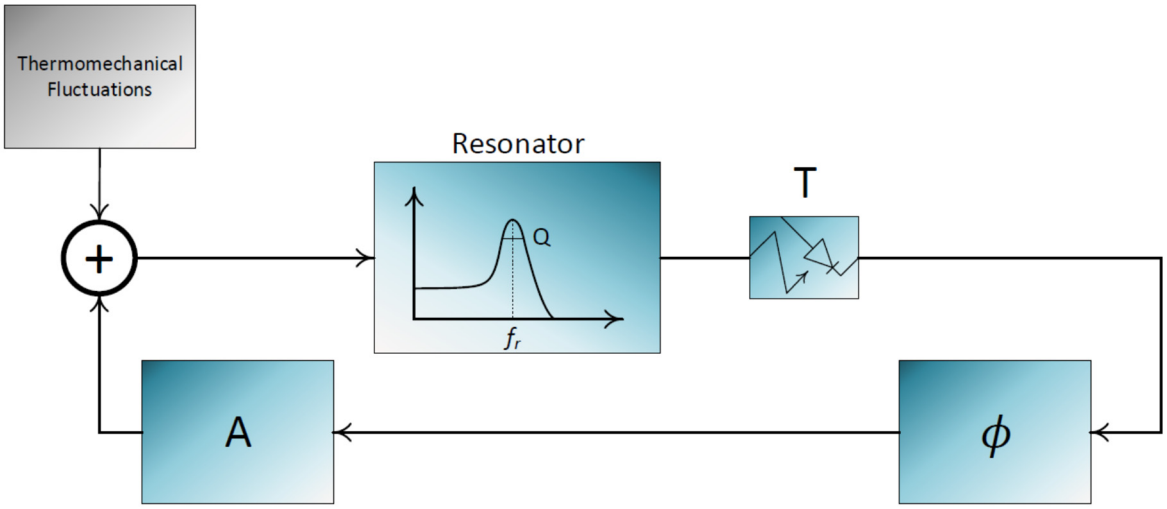

Figure 2.9. Block diagram showing the resonator in a closed-loop topology for enhanced performance.

In such a self-oscillating deployment, the thermomechanical fluctuations native to the structure are detected by a photodiode sensing circuit and fed back to the input drive of the resonator. The feedback signal acquires a transduction gain T, a phase shift ϕ, and an amplification A. Given this positive feedback, the minute thermomechanical fluctuations lead to large relative deflections of the structure, determined by the gain and phase characteristics of the feedback. The closed-loop transfer function becomes:

$$T(f) = \frac{H(f)}{1 - H(f) \cdot T \cdot e^{j\phi} \cdot A} \tag{2.51}$$

$$T(f) = \frac{C \cdot T \cdot {f_o}^2}{{f_o}^2 + \frac{f_o f}{Q} j - f^2 - A \cdot T \cdot C \cdot {f_o}^2 \cdot e^{j\phi}} \tag{2.52}$$

If we enforce that $\phi = {}^{\pi}/_{2}$, the closed loop transfer function assumes the form of a harmonic oscillator around f_o, now with additional variables in its damping term.

$$T(f) = \frac{C \cdot T \cdot {f_o}^2}{{f_o}^2 + f_o f \left(\frac{1}{Q} - A \cdot T \cdot C \cdot \frac{f_o}{f}\right) j - f^2} \tag{2.53}$$

With an actuation potential around the natural frequency ($f \approx f_o$), we find that the system experiences an effective quality factor given by Equation (2.54). With set device parameters and a fixed transduction gain, variation in gain *A* can produce an effective quality factor that can increase by several orders of magnitude [58] [59].

$$Q_{eff} = \left(\frac{1}{Q} - A \cdot T \cdot C\right)^{-1} \tag{2.54}$$

Absent of extrinsic noise sources to the resonator, the ultimate resolution becomes limited by intrinsic processes that lead to the minimal resolvable mass based on mass sensitivity, which become progressively important as the structure size reduces into the NEMS regime to target diminishing sample size. This underlying physical limit spurs from thermomechanical fluctuations as well as adsorption-desorption noise and momentum exchange with gas molecules [60]. This limit depends on the mechanical Q, regardless of the feedback enhancement and effective quality factor, since this noise is always present

in the feedback loop and the mechanical quality factor determines how well the resonator filters this noise at its output.

Section 2.4: Optical Manipulation and Trapping

The previous sections illuminate the dynamics that give rise to positional dependent mass measurement and insight into the resolution threshold with which this becomes observable and important. To reduce the variance in x_o and accompanying fluctuation in measured mass m, we seek to incorporate laser trapping for positional stability and suppression of random motion, in a device that allows for external optical probing and integrated photonics.

Optical trapping hinges on the behavior of a dielectric particle in an inhomogeneous electromagnetic field. This environment produces a gradient force, denoted as F_{grad}, which tracks the gradient of the optical intensity, I_o. The Gaussian profile of a focused laser beam meets this condition with its gradient reducing to zero at the center of the beam, thereby creating a "trap" or a low-energy state. The following equation defines this phenomenon more rigorously [61]:

$$F_{grad} = \frac{2\pi a}{c{n_m}^2} \cdot \nabla I_o \tag{2.55}$$

$$\text{where } a = {n_m}^2 \cdot r^3 \left(\frac{\left(\frac{n_p}{n_m}\right)^2 - 1}{\left(\frac{n_p}{n_m}\right)^2 + 2} \right) \tag{2.56}$$

In the equation, c is the speed of light in a vacuum; n_m is the surrounding medium's index of refraction; n_p is the particle's index of refraction; and r is the radius of the spherical particle.

When employing optical trapping, another important force participates in sample manipulation, specifically in the axial direction. The scattering force, F_{scatt}, develops as a consequence of absorption and re-emission of optical energy by the particle, and the force can be described by [50]:

$$F_{scatt} = \frac{I_o \cdot \sigma \cdot n_m}{c} \tag{2.57}$$

$$\text{where } \sigma = \frac{128 \cdot \pi^5 \cdot r^6}{3\lambda^4} \left(\frac{\left(\frac{n_p}{n_m}\right)^2 - 1}{\left(\frac{n_p}{n_m}\right)^2 + 2} \right)^2 \tag{2.58}$$

It is important to note that this analytical description of the scattering force requires the conditions for Rayleigh scattering, which imposes that r is much smaller than the wavelength λ, which is a reasonable assumption given trapped particle sizes. This force gives rise to a radiation pressure, which drives the particle downward into the substrate. The phenomenon can increase the particle's interaction with the substrate surface and spurs a resulting friction force that is an important consideration in moving the particle along the surface.

These equations can give us critical insight into the forces that enable optical trapping techniques. Since the force is proportional to the intensity gradient (∇I_o) and assuming that particle and medium properties are invariant, improving the trapping force either requires an increase in the optical intensity I_o or a modification to the intensity profile and its resulting gradient. As previously introduced, increasing the intensity poses a threat to the viability of cells captured by the trap especially over the course of long-term trapping experiments. Therefore, engineering the intensity profile becomes the viable approach.

The design and approach in this work centers on silicon, due to its versatile optical properties and its precise machinability. Furthermore, silicon supports the fabrication of a PhC surface that modulates the incident laser intensity profile to achieve a higher gradient force. Figure 2.10 shows the focal enhancement just above the PhC, calculated through

finite-difference time-domain (FDTD) simulation [23] [62]. By affecting the field and focal spot, the PhC increases the optical trapping force for a given optical power, ultimately, allowing for a reduction in overall optical energy that is beneficial for cells and other biological explorations [23] [63] [64]. Furthermore, the PhC's diffraction properties ensure that the trapped cell is always attached to the PhC surface and resonates with the silicon beam, satisfying a necessary condition of resonant mass sensing.

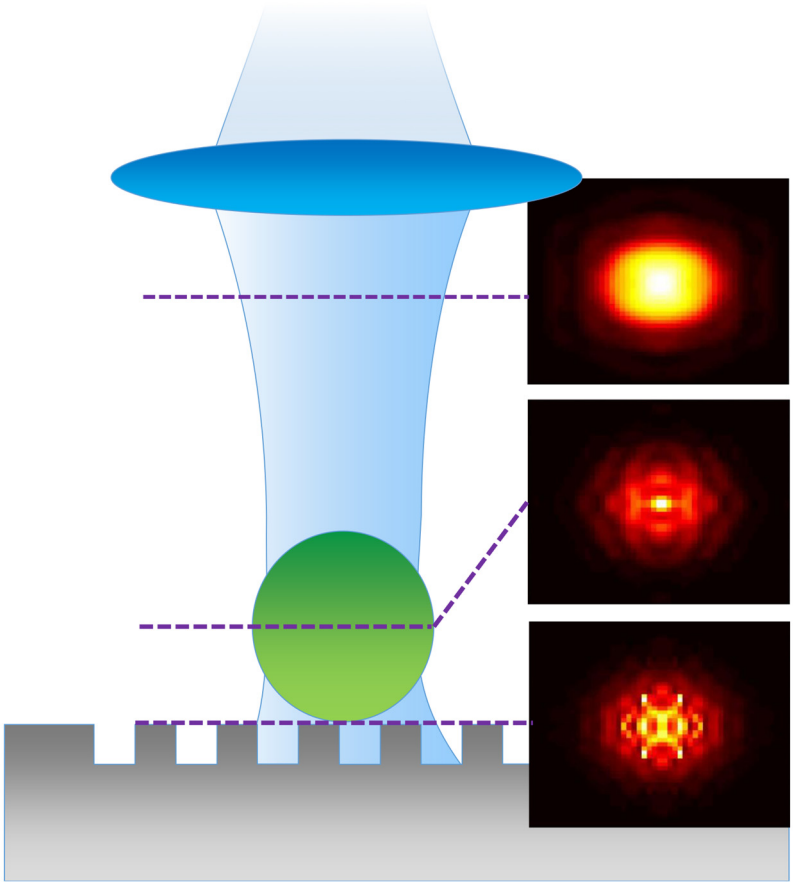

Figure 2.10. An illustration showing finite-difference time-domain (FDTD) numerical simulations demonstrating the optical focal enhancement just above the PhC surface. This enhancement increases the optical trapping force without requiring greater overall optical power [62].

Chapter 3

Design

Implementing the underpinning theory presented in the preceding chapter requires many design approaches necessary to realize the physical devices and supporting metrology system. The hybrid silicon-channel MEMS structure, further described in Figure 3.1, comprises a PhC optimized for trapping (discussed in more detail in the preceding section) that is imbedded in the silicon bridge layer. The bridge supports a polymer channel as the integrated fluidic design element, and beneath the silicon structure, in close proximity, is a silicon substrate electrode to facilitate resonant, electrostatic-actuation of the device. This scheme lends itself to resonant-frequency determination through optical deflection or capacitive sensing and a feedback-loop drive to track the resonant frequency in real-time with improved fidelity. This section will first visit the design constraints and methodologies for the fluid-integrated resonant sensor to arrive at key dimensions and topological considerations. These simulations and designs are embodied by physical devices described in the next chapter, in the context of their fabrication.

Beyond the structure itself, there are several critical subcomponents required to enable the measurement, embodied by a system for both operation and acquisition of data. This supporting system employs a vacuum chamber to mitigate air damping on the structure, a fluorescence microscope for utility with cell labeling, microfluidics for sample delivery, an optical setup for particle trapping and combined resonant frequency detection,

feedback/detection electronics for stable measurement, and acquisition/processing software to obtain the final result and data.

Section 3.1: Device Structure

Section 3.1.1: Structural Topology

As explored in Chapter 2, there are several important considerations essential in fine-resolution mass measurement, including the quality-factor and sensitivity. First, a high quality-factor for the beam resonator, aided by a high resonant frequency, is critical to frequency stability and resolution of mass-induced frequency shifts. Secondly, the ratio between the sample mass and the structural mass must be maximized in the name of sensitivity, i.e. a small mass change will induce a greater resonant frequency shift on a lighter, thinner structure. This is more rigorously addressed in Section 2.3: Mass Sensing. In the limit that devices become prohibitively fragile, this design seeks to reduce the

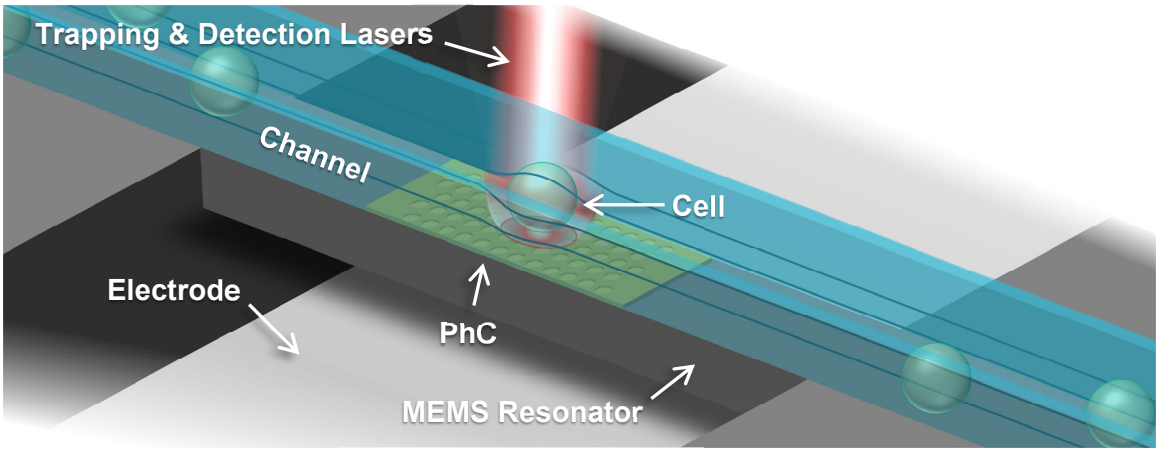

Figure 3.1. Labeled illustration of the resonator design showing the main components of the system, including the electrostatic drive electrodes, transparent fluidic channel, and the incorporated PhC.

resonator's mass, bounded only when it becomes incapable of microfluidic flow or unable to accommodate target samples with required inner-channel dimensions. Experiments with mammalian cells can impose channel requirements exceeding 15–20 μm.

There are many micro-resonator configurations including cantilevers (fixed-free), bridges (fixed-fixed), torsional, paddle, and others. The main design adopted in this work involves a MEMS resonator consisting of a fixed-fixed silicon-beam structure to support the optically-clear fluidic channel that delivers bio-samples or particles for mass measurement. As a true engineering challenge, the bridge structure is accompanied by a set of tradeoffs. The fixed-fixed topology does yield to a few notable drawbacks, when compared with a cantilever design, including increased mass, increased coupling between stiffness and mass addition, and to some extent, increased damping when compared to fixed-free topologies. In spite of these disadvantages, the clamped-clamped arrangement does simplify the internal fluidic geometry toward the achievement of one aim of this work: targeting enhanced control of the cells as they propagate along the channel and undergo mass measurement. The simplification of this geometry excludes ninety-degree corners otherwise required by a cantilever or torsional design, which leads to a critical improvement in positional sensitivity and sample control.

In a simulation-driven design approach, the following discussion utilizes a finite element analysis (FEA) package (COMSOL Multiphysics®) with simulations based on Navier's equations to ultimately obtain the structural eigenvalues necessary for understanding resonant characteristics. Given target sizing for cells with the goal for a high-frequency, actuatable device, FEA simulations led to a bridge structure that is described by the dimensions 1.5 μm × 33 μm × 250 μm, which supports an integrated channel measuring 7 μm (height) × 10 μm (width), with a 5-μm thick wall. The structure simulation indicated a resonant frequency in the range of 200 kHz, with a modal representation of the structure in Figure 3.2, showing both the fundamental mode and the channel configuration.

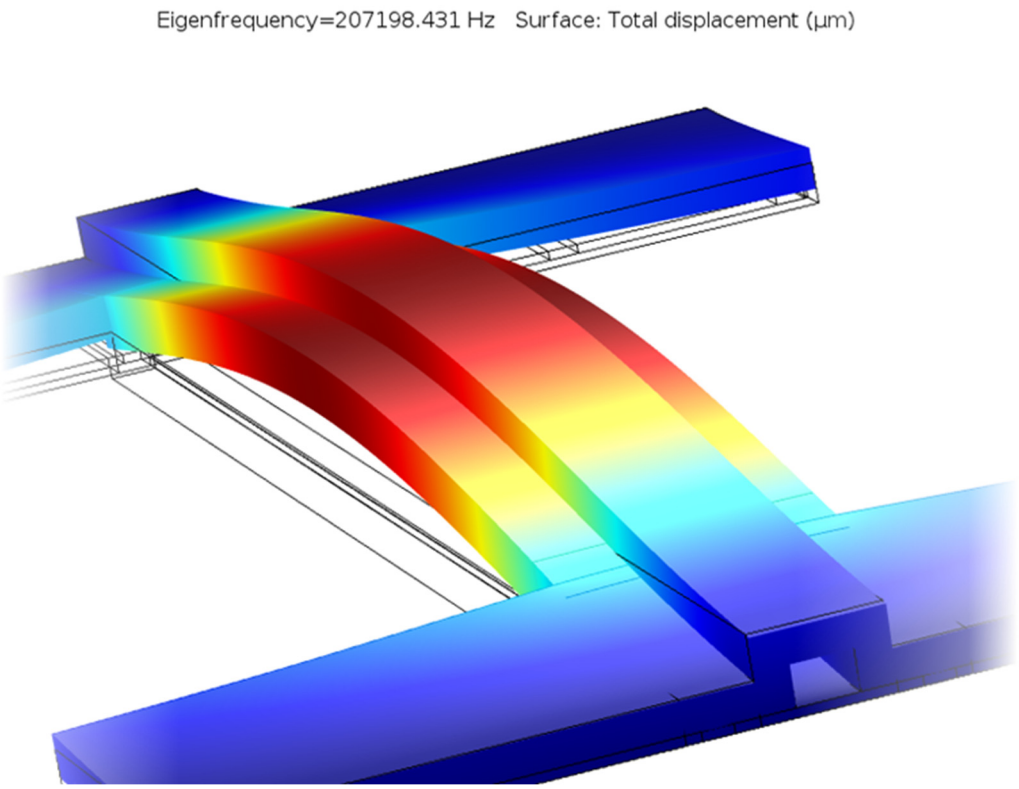

Figure 3.2. This surface plot shows the total displacement of the structure resulting from an Eigenfrequency simulation, described by a resonant frequency of 207 kHz as the fundamental structural mode.

This simulation validated the positional dependency of mass measurement. To obtain the relative error in the frequency shift as a function of displacement, the simulation shifted a one nanogram mass parallel to the direction of major fluid flow. Figure 3.3 plots the relative error around the center mass position for both cantilever and bridge devices, observed as a variance in resonant frequency shift. The simulation defines the center position in the middle of the mass sensing area (at the tip of the cantilever or the vertex of the bridge). Due to the complement between flow directionality and modal deformations respecting the beam's transverse axis, the bridge device substantiates a stark improvement over the positional dependent mass sensing exhibited by non-symmetric or cantilever structures.

Specific to the bridge-channel structure of this work, Figure 3.4 demonstrates more clearly the need for precise cell position control, showing the error (frequency shift variability) due to lateral movements in mass. Given the selected bridge resonator, lateral shifts along the channel length accumulate significant error, with higher immunity to variation along the width. This insight can guide optical trapping control and illuminate the role Brownian motion plays in measurement accuracy. With the described trapping scheme, lateral position control of bio-samples can be accomplished through high-precision PhC trapping promising an adequate trapping force to restrict Brownian motion below 500 nm, with potential for even greater reductions for larger cells and particles.

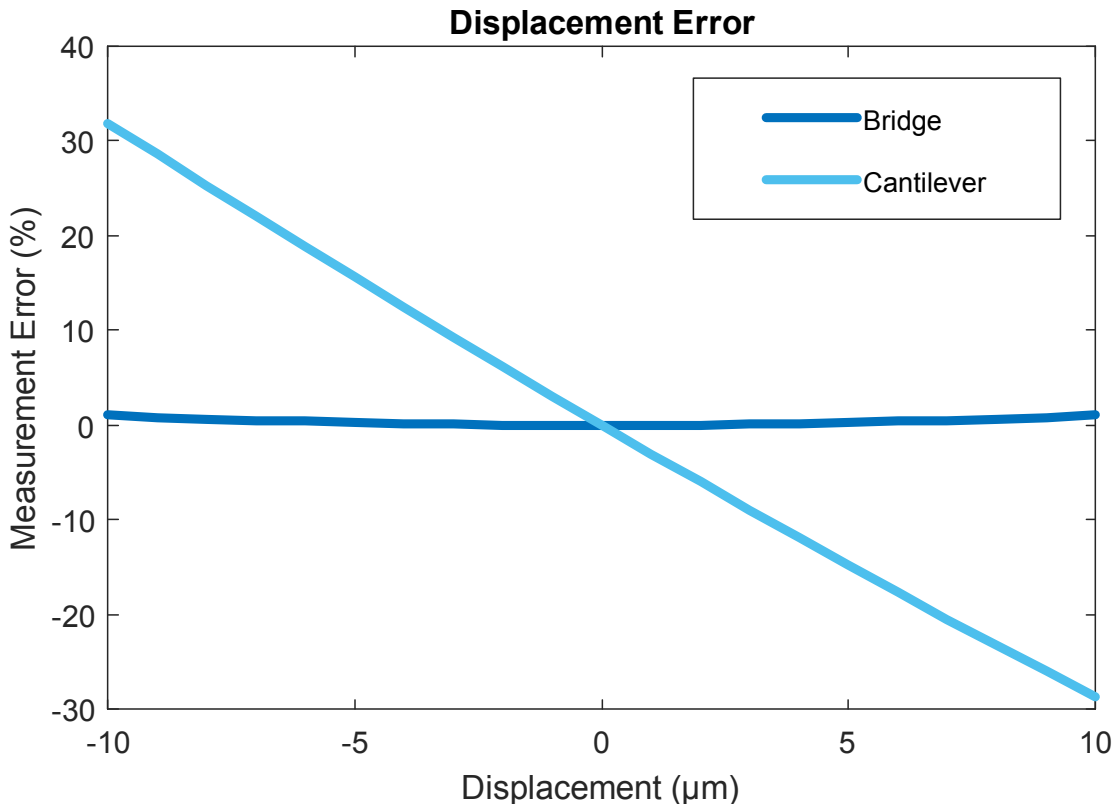

Figure 3.3. Simulated displacement error comparing the responses of a bridge structure with that of a cantilever device. The error becomes significant with displacement from the center position of the cantilever.

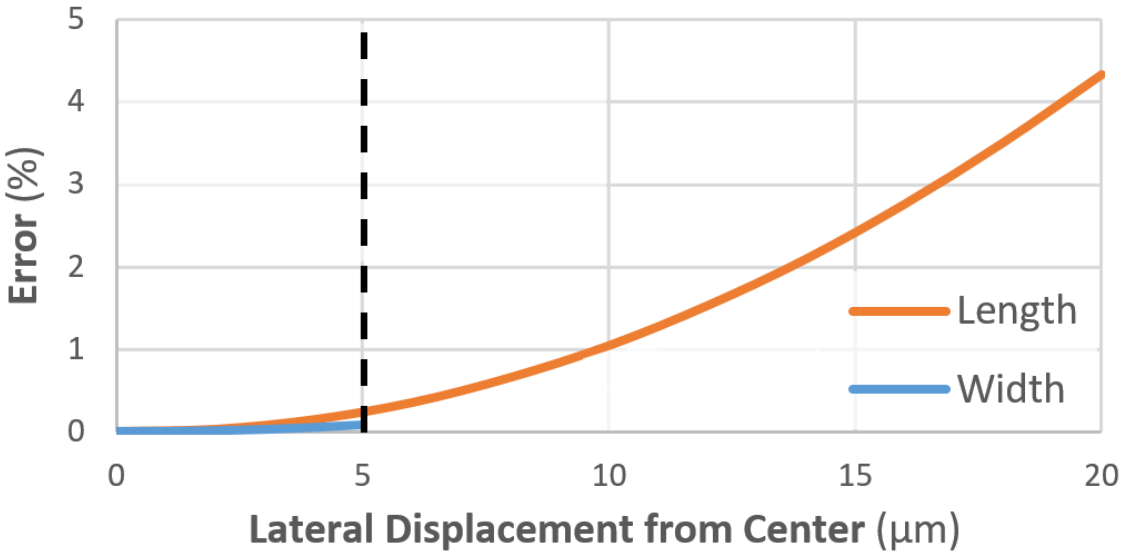

Figure 3.4. Numerical simulations observing mass error from lateral position change along the channel length and width.

Section 3.1.2: Channel Structure

Affixed atop the silicon bridge is an encapsulating fluidic channel comprising walls of parylene, known more formally by its chemical name poly(p-xylylene) and classified as a very bio-compatible and transparent material, two essential properties for this work. It encompasses a family of long-chain polymers, boasting a unique capability of low-temperature deposition through vapor-phase pyrolysis and vapor condensation [65]. More generally, parylene serves as an important barrier in many devices, including flexible [66] and organic electronics [67], even applied in solar cells. More relevantly, parylene has seen application in a number of implantable or biological sensing applications, such as neural probes [68] [69], intraocular pressure sensors [70], and ocular muscle stimulation [71].

Parylene-C is a member of the parylene family that provides useful mechanical properties and electrical isolation, but even more importantly, it has a very low permeability to moisture, which lends itself well for microfluidics. Researchers have applied parylene in numerous fluidic devices, including a self-pressure-regulating valve [72], a microfluidic-integrated neural probe [67], a micro-electrophoresis system [73], and an impedance-based fluid-filled force transducer [74]. Parylene also has a high chemical stability and inertness [75], which makes it a good candidate for integration into MEMS processing. Table 3.1 enumerates some key properties of the employed parylene-C.

Table 3.1. Material Properties of Parylene-C [76]

Tensile strength (psi)	10,000
Yield strength (psi)	8,000
Young's Modulus (psi)	400,000
Density (g/cm^3)	1.289
Index of Refraction	1.639
Linear Coefficient of Thermal Expansion at 25 °C (ppm)	35
Thermal Conductivity at 25 °C (W/m·K)	0.084
Melting Point (°C)	290
Glass Transition Temperature (°C) [77]	80 – 100
Poisson Ratio utilized for Simulation [78]	0.4

These properties make parylene a good candidate for inclusion in the channel-resonator devices. It allows for integration of the trap-enhancing silicon PhC and it maintains compatibility with microscopy, flow cytometry, and other diagnostic optical

methods. This is a marked advantage over other embedded fluidic mass sensing structures, where the sample is concealed by opaque materials utized in resonator fabrication. Figure 3.5 compares the transmittance for parylene with that of silicon, which is a standard material in resonator fabrication due to established fabrication processes and excellent mechanical properties. A clear advantage of parylene is its high transmittance over the visible spectrum and at important biological wavelengths including those for the trapping laser (1064 nm).

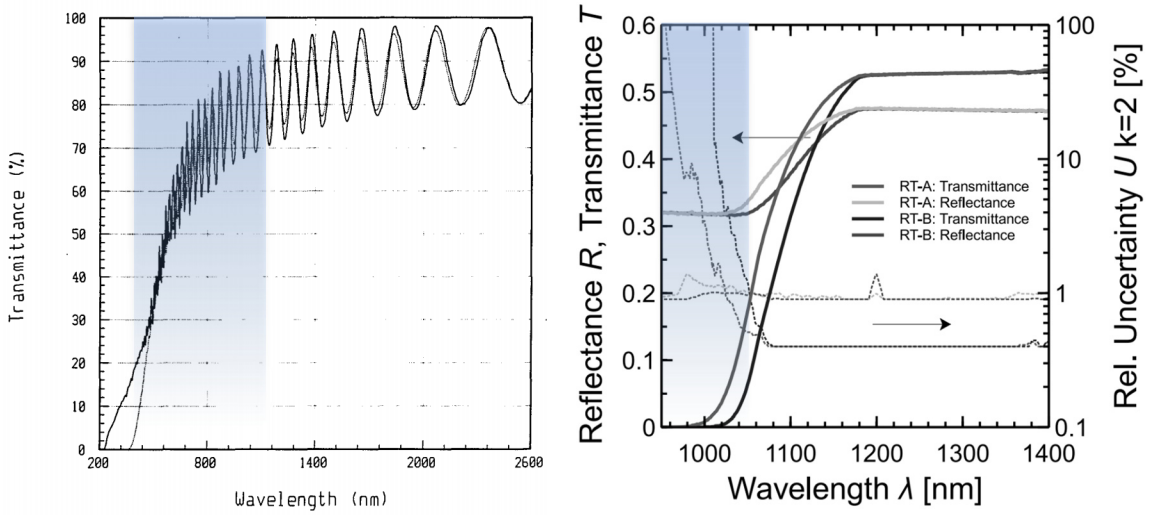

Figure 3.5. (A) Experimental transmittance spectrum for parylene showing transparency over the optical and near-infrared bands. [Adapted with permission from [79], OSA Publishing.] (B) Measured reflectance and transmittance for chemo-mechanically polished, monocrystalline silicon wafers. [Adapted from [80], AIP Advances, Vol. 5, Article ID 067168, 2015; licensed under a Creative Commons Attribution (CC BY) license.]

Clearly, the mechanical strength of the parylene and its fixation with the silicon substrate dictate its pressure and fluid flow specifications. This work investigated two methods of attaching and porting to the fluidic channel (a frontside and a backside process

that are discussed in more detail by Chapter 4). High pressure is only attainable with the backside process, and warrants design of the supported fluidic pressure. Maximum pressure can be determined by consideration of the stress that forms in the parylene layer. The tensile or fracture strength (as listed in Table 3.1) for parylene-C is around 69 MPa (10,000 psi) and serves as a merit of structural failure. From the port simulation shown in Figure 3.6, a loading pressure of ~330 psi approaches this material limit.

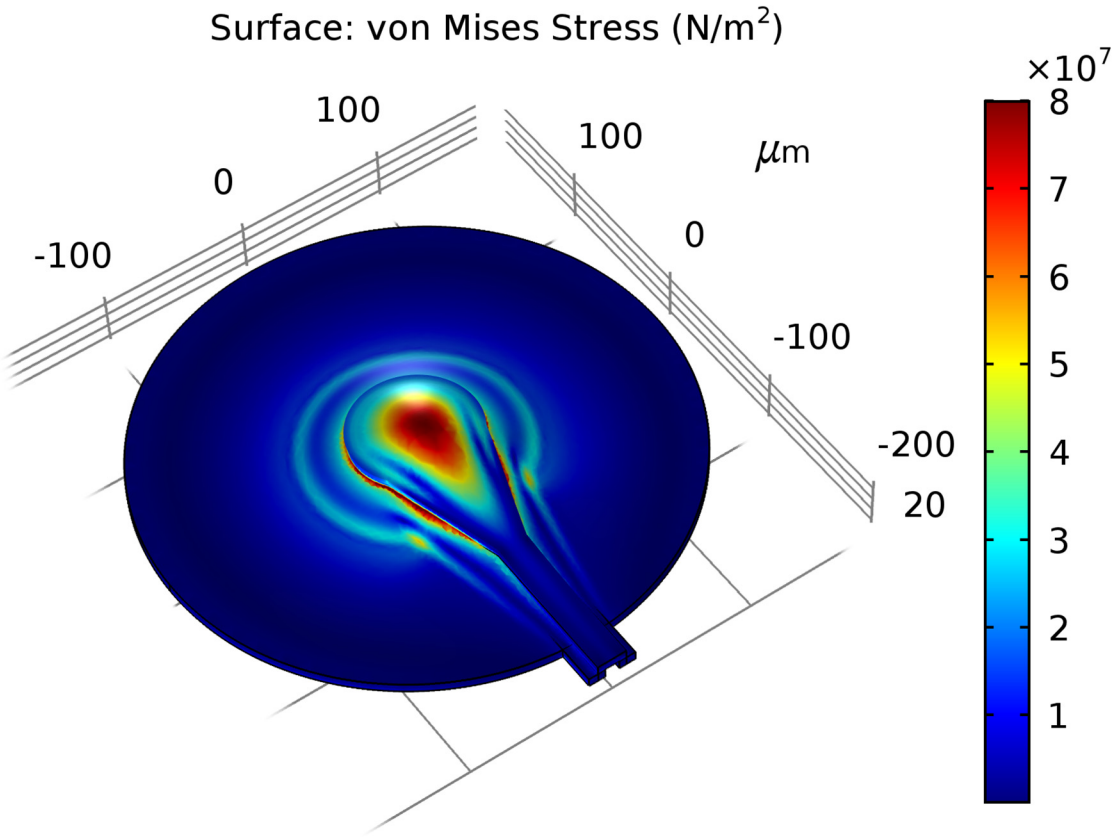

Figure 3.6. A stress simulation for the parylene port structure simulation at the limit of parylene fracture, driven at a pressure of ~330 psi.

While pressure describes the overall force required for failure, another critical, dependent parameter is flow through the channel. This becomes especially important in flow-driven operation. The velocity of the flow in the channel is given by Equation (3.1).

$$v = \frac{r}{A} \tag{3.1}$$

where r is the flow rate, and A is the cross-sectional area of the channel. The velocity and characteristic dimensions of the fluidics are important in determining the flow behavior. The Reynolds number describes the relationship between inertial and viscous forces; at low Reynolds numbers, the viscous forces dominate, and the resulting flow is very linear (laminar), and conversely, high values observe turbulent flow. The regime transition occurs at a value between 2000 and 3000, for a circular pipe [81]. The Reynolds number can be found by the following expression, where ρ is the fluid density, D is the channel diameter, and μ is the dynamic viscosity:

$$Re = \frac{\rho \cdot v \cdot D}{\mu} \tag{3.2}$$

Flow through the channel experiences friction as the constituent fluid molecules interact with each other and the channel wall. This reduces the pressure of the fluid as it propagates, analogous to the voltage drop observed by electrical current encountering a resistance. The generalized description of this behavior takes the form of Darcy's formula for a horizontal pipe, describing head loss (H_L) in the fluid [82]:

$$H_L = f \frac{L}{D} \frac{v^2}{2g} \tag{3.3}$$

where L is the length of the channel, f is the friction factor, and g is the acceleration of gravity. When the flow is laminar ($Re < 2000$), the friction factor can be approximated by Equation (3.4).

$$f = \frac{64}{Re} \tag{3.4}$$

Finally, the change in pressure along the pipe can be found:

$$\Delta P = \rho \cdot H_L \cdot g \tag{3.5}$$

By obtaining the pressure differential for a given flow rate, the specified rating of the channel can be determined by linking the flow rate to pressure, and pressure to structural failure. The measured flow rate limit (discussed in Chapter 4) matches well with the pressure limitation shown by this simulation and analytical calculation. It is important to note that the channel is assumed of circular cross-section for this calculation, which is more closely embodied by a fully inflated channel approaching its structural integrity limit.

Section 3.1.3: Sensitivity and Resolution

As clarified in Section 2.5: Structural Damping and Resolution, structural sensitivity and quality factor are important device characteristics. It is therefore essential to simulate the device based on these performance metrics. The design described in this section shows the potential to resolve mass changes with a sensitivity of about ~1.1 Hz/pg at the beam center. Figure 3.7 portrays the relationship between mass and frequency shift; the simulation verifies the linear relationship for small mass variations and gives us a tractable method for relating resonant frequency with absolute mass measurement or observation of relative mass changes. Figure 3.8 explores the sensitivity dependence on structural mass (length) and sample mass at two positions, the beam center and the anchor sites, to demonstrate positional variation in sensitivity. The addition of several measured data points serves to validate the simulation results. The overall mass of the structure is

estimated to be about ~140 ng based on design dimensions and established material properties.

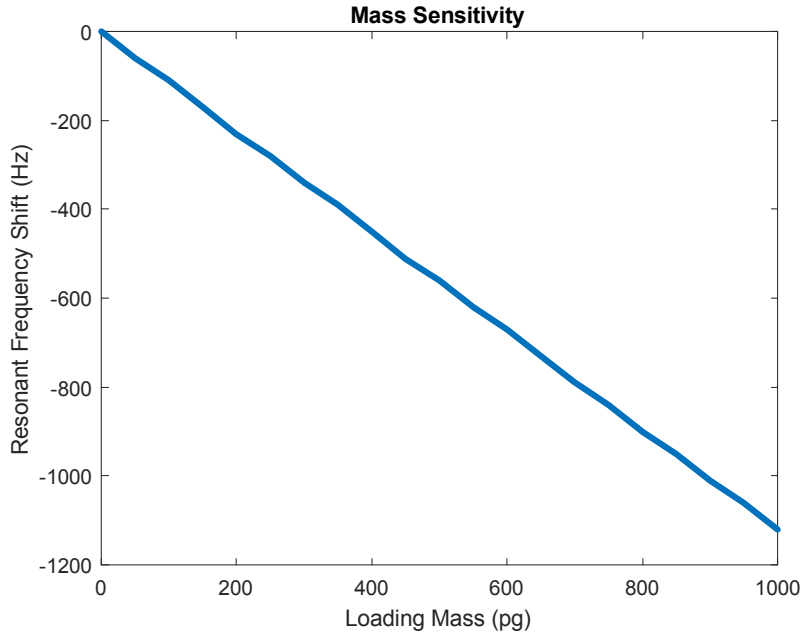

Figure 3.7. Mass sensitivity of the bridge-channel resonator showing the relative resonant-frequency shift resulting from mass loading, demonstrating a sensitivity around 1.1 Hz/pg.

Upon determining device sensitivity, we must consider the resolution with which we can observe these shifts in frequency that depends on the fidelity and stability of the resonator, determined in large part by the quality factor. There are many underlying processes that lead to structural damping, and it is the reciprocal sum of all those contributions that determine the overall quality factor. In atmosphere, air damping often becomes the most significant energy dissipation mechanism and severely limits the quality of the resonator, as discussed earlier. Figure 3.9 shows an upper limit of the quality-factor, as determined by pressure, squeeze-film, and thermo-elastic contributing terms. From the figure, it is clear that a medium-vacuum environment can push the quality-factor limit upwards into the 10,000 range, giving desirable stability characteristics. As will be

addressed later, the actual fabricated devices do not reach this limit: once transitioning into the low-pressure regime, other effects begin to dominate, including support, friction, and surface losses, which prevent realization of this limit. However, this simulation insight agrees with the well-known relationship between pressure and quality-factor [83]:

$$Q_{air} \propto \frac{\sqrt{k_b \cdot T}}{P} \tag{3.6}$$

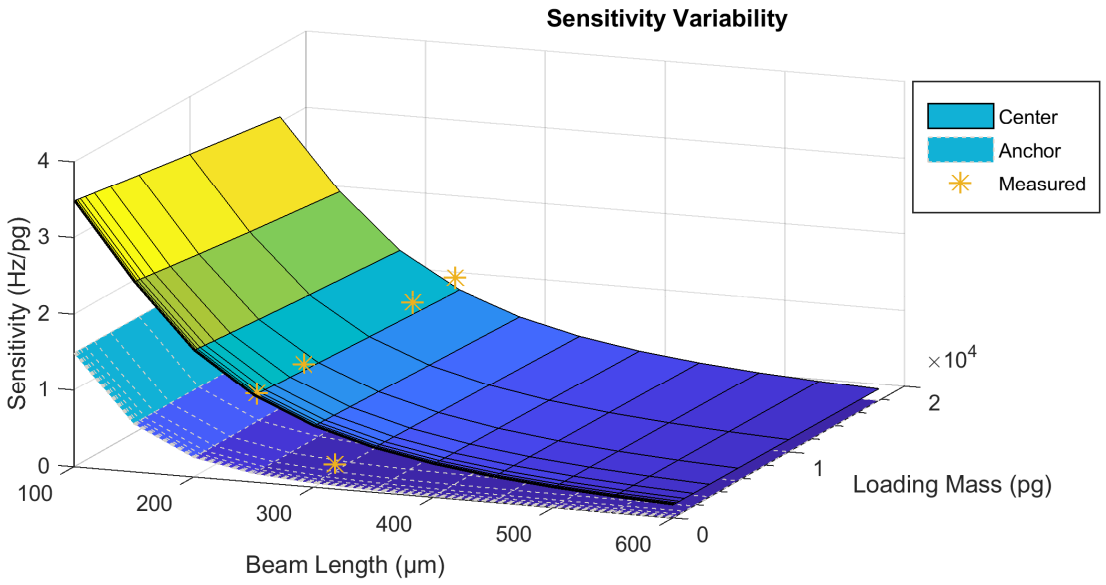

Figure 3.8. Surface plots depicting sensitivity variation of structure mass, sample mass, and position (at its two boundary cases). The orange points indicate measured data and serve to unify simulation and measurement. Optical trapping serves to close the vertical gap in sensitivity, and structural design renders a device suitable for the appropriate mass responsivity.

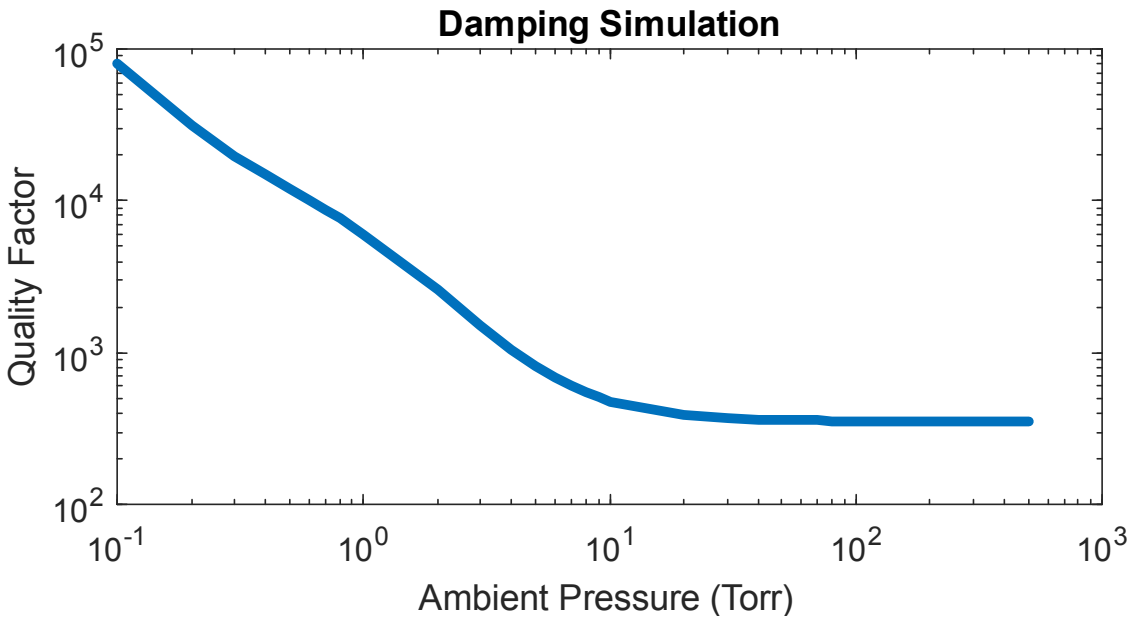

Figure 3.9. Simulated quality-factor with respect to ambient pressure. Under lower vacuum, the quality-factor is of the hundreds order, and under a medium vacuum the quality-factor limit reaches the 10,000s range. This limit does not consider all sources of damping.

Section 3.1.4: Electrostatic Actuation

Due to its simplicity and straightforward integration in silicon devices, an electrostatic drive served as a viable method of actuation. It can be introduced either through high silicon doping levels or metal electrode deposition. Other MEMS actuation methods, such as optical, piezoelectric, or electromagnetic [84], can boast benefits regarding compact electrode configurations or operation in conductive fluids; however, the electrostatic drive serves as the most appropriate option for this work as it does not mandate special materials, additional fabrication complexity, or external magnetic fields. Utilizing electrostatic actuation can pose prohibitive challenges when operating in a conductive

medium, such as cell culture media, but fluid integration inside of the structure removes this limitation.

Electrostatic actuation relies on the Coulombic force that develops between charges with proportionality to the inverse of their separation squared. In mathematical terms, the force can be represented as:

$$\mathrm{F} = \mathrm{k}\frac{q_1 q_2}{r^2} \tag{3.7}$$

To utilize this phenomenon in a coordinated and useful effort, MEMS devices develop a capacitance between two adjacent surfaces. In doing so, the opposite charges on each capacitor node attract their counterparts, thereby producing an attractive force between them. If we assume that the capacitor comprises two simple, parallel plates and that the force produces only one-dimensional motion, we can arrive at a simple expression for the force.

Voltage (V) is the potential that relates charge (Q), and its implicit displacement, to energy (U); capacitance C describes an ability to store charge per a prescribed voltage. By integrating this potential over charge, we can obtain the energy stored by a capacitor:

$$\mathrm{U} = \int_0^Q V \cdot dq = \int_0^Q \frac{q}{C} \cdot dq = \frac{1}{2}\frac{Q^2}{C} = \frac{1}{2}QV = \frac{1}{2}CV^2 \tag{3.8}$$

For a simple parallel plate capacitor, we can assert the expression shown by Equation (3.9) in for capacitance.

$$\mathrm{C} = \frac{\varepsilon A}{s} \tag{3.9}$$

where ε is the permittivity of the medium between the plates; A is the area of the plate surfaces; and s is their spacing. We know that energy can serve to accomplish work by applying a force over a distance; therefore, the derivative of the capacitor energy gives an equation for force:

$$\mathrm{F} = \frac{dU}{ds} = \frac{d}{ds}\left(\frac{1}{2}\frac{\varepsilon A}{d}V^2\right) = -\frac{\varepsilon A V^2}{2d^2} \tag{3.10}$$

From the result in Equation (3.10), it becomes clear that given a fixed structural geometry (determined rather by resonant frequency, mass, or damping considerations), surface proximity or voltage become deterministic parameters, which must additionally appease device size and stiffness to achieve a measurable deflection. As a matter of good engineering practice, the design sought a minimized actuation voltage, to simplify electronic drive circuitry and mitigate other challenges associated with high-voltage systems, including breakdown and operational hazards.

Briefly, to gain insight into electrostatic actuation specific to the beam structure, we can consider the non-dimensional differential relationship shown in Equation (3.11) that governs the electrostatic resonant response of the beam, where $w(x,t)$ is the normalized transverse deflection along the beam, respecting displacement x and time t; $v(t)$ is the actuation voltage; and c, $\propto_1$, $\propto_2$, and N are parameters that describe material properties, dimensions, and loading of the structure [85]:

$$\frac{\partial^4 w}{\partial x^4} + \frac{\partial^2 w}{\partial t^2} + c\frac{\partial w}{\partial t} = [\propto_1 \Gamma(w,w) + N] \times \frac{\partial^2 w}{\partial x^2} + \frac{\propto_2 v^2(t)}{(1-w)^2} \tag{3.11}$$

$$\text{where } \Gamma(f_1(x,t), f_2(x,t)) = \int_0^1 \frac{\partial f_1}{\partial x}\frac{\partial f_2}{\partial x}\,dx$$

In review of the clamped-clamped configuration, the differential equation is subject to the boundary conditions shown in Equation (3.12).

$$\mathrm{w}(0,\mathrm{t}) = \mathrm{w}(1,\mathrm{t}) = 0 \tag{3.12}$$

$$\frac{\partial \mathrm{w}}{\partial \mathrm{x}}(0,\mathrm{t}) = \frac{\partial \mathrm{w}}{\partial \mathrm{x}}(1,\mathrm{t}) = 0$$

By reducing the forcing voltage to only a static component and setting the time derivative to zero, the resulting static solution analytically aids in determining beam dimensions and electrode spacing, which led to a sensible spacing design between 5 and 10 μm. This spacing is also reasonably within standard silicon-on-insulator (SOI) manufacturing specifications.

Section 3.2: Vacuum Chamber Design

Attainment of a high-quality resonator is of paramount importance in measuring the mass of single cells. As detailed in the previous and background sections, vacuum is critical to this end. As the most appropriate solution, we devised a specialized vacuum chamber that attached directly below the objective lens of a fluorescent microscope on a two-dimensional motorized stage. The chamber was capable of mounting resonator devices by providing necessary electrical and fluidic connections.

Figure 3.10 shows a representative three-dimensional, computer-aided design (CAD) model. The chamber is sealed by an O-ring assembly and a glass plate that features anti-reflective coatings optimized for the resonant frequency detection laser (633 nm) and suitable for the optical trapping wavelength (1064 nm), since the optical trapping laser makes only one pass through the window.

There are four external fluidic ports that allow fluid to bypass the device. This is essential when loading the sample into the devices; since the resonant channel is highly constricted allowing only micro-liters of flow, it would be impractical to wait for macro-scale volumes of fluid to pass through the channel. Instead, the sample can be loaded by bypassing the device and continuing into a waste channel. The chamber allows fluid

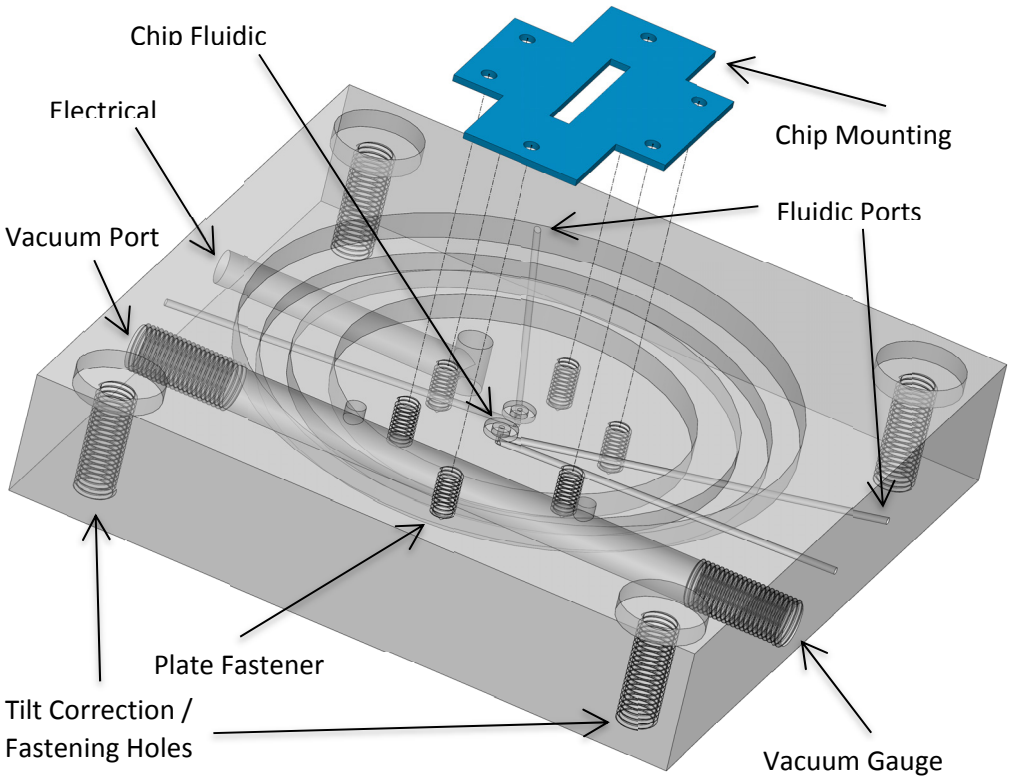

Figure 3.10. A CAD model of the vacuum chamber mount, illustrating the chip mounting plate, and various ports for fluid, probing, and vacuum.

connection from the bottom of the chamber with small O-ring seals that mate with etched port holes in the back of the silicon chip. A plate is fastened over the device to ensure adequate compressive pressure to form a seal and fix device position. The plate has a slit opening to reveal the MEMS structure and has six holes that mate with threaded holes in the bottom of the chamber. A solid plate (without a slit) can be used for devices not requiring fluidics and with backside-deposited electrodes.

A larger port is dedicated to the electrical assembly, consisting of two wires to probe each electrode of the device. The ground electrode is attached to the mounting plate, and contacts the substrate layer through gold pads deposited around the edge of the chip.

The second wire forms an electrode which is held in place by the mounting plate against gold electrodes on the device layer surface. The electrodes are housed in a 1/8 NPT threaded fitting, which is sealed by a vacuum grade epoxy.

There are four holes at each corner for attaching the chamber to a base. They also serve as tilt-correction adjustments to ensure a proper angle with the microscope. The chamber itself is made of an acrylic plastic for two reasons: the first is so that the chamber itself is not conductive and will therefore not present additional challenges for probing the sample, and second, the polished acrylic is optically transparent, which yields tremendous aid in port alignment and monitoring the fluid lines for bubbles or other obstructions. However, one drawback for acrylic is its chemical stability; many solvents, including acetone, dissolve acrylic plastics, and this can make cleaning the channel challenging given these chemical constraints.

The chamber integrates two 1/8 NPT threaded holes: one connects to the vacuum pump and the other connects to a vacuum gauge for observation of chamber pressure. The chamber can achieve a vacuum level below 30 mTorr, and with a more powerful vacuum pump this pressure may be further reduced. Figure 3.11 shows a device mounted within the chamber with the pump, gauge, fluidics, and probing peripherals attached to the chamber. The vacuum chamber and ensuing vacuum environment achieved at least a factor ten enhancement for the Q-factor.

One practical challenge for chamber design was the close proximity between the device surface and the sealing window. Due to the short working distance of the microscope objectives (~9 mm) and the existence of increased index of refraction in the beam path, the chamber had to possess a very shallow depth, which did not allow for tall electrical probes or mounting structures. Therefore, window thickness was important for both spatial and optical-clarity considerations.

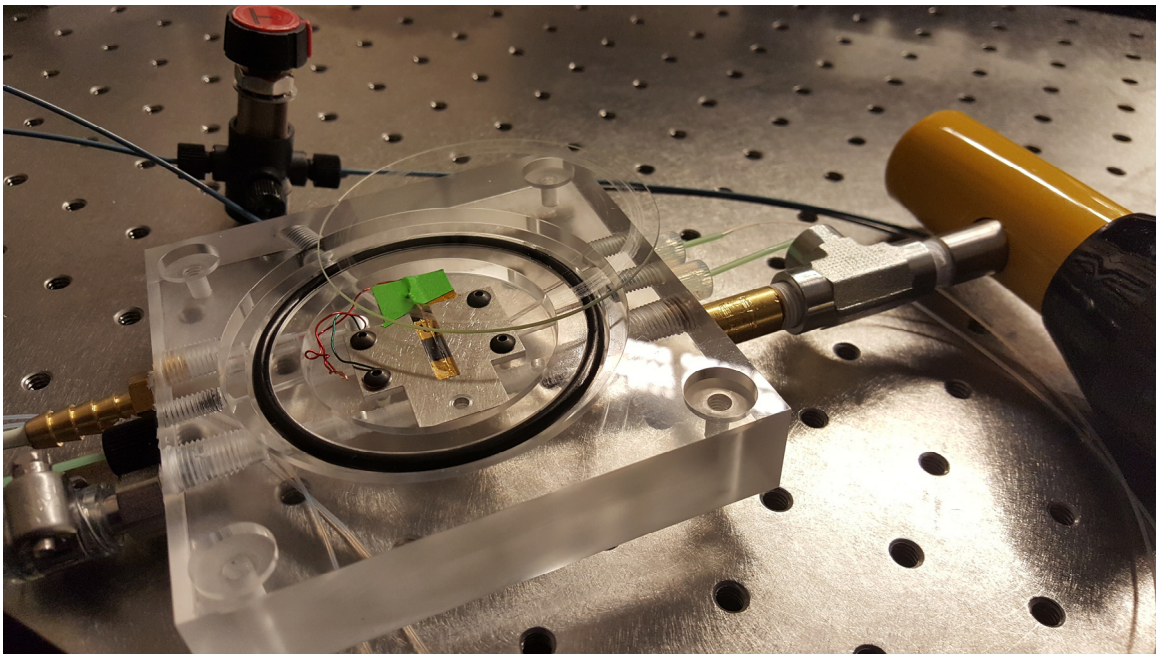

Figure 3.11. Shown is a picture of the vacuum chamber with attached vacuum, probing, and fluidic peripherals with a device mounted inside.

Section 3.3: Microfluidic Setup

The microfluidic setup serves several functions critical to loading the channel with sample cells and controlling the fluid flow across the device. For better controllability, the fluidics adopted a pressure-driven approach as detailed in the fluidic schematic of Figure 3.12. The setup employs microfluidic tubing (~250 μm cross-section) for operation with small sample volumes, which is an important characteristic for efficient cellular study. Fluid is contained in pressurized bottles that possess ports for both the microfluidic tubing and compressed air to push the fluid, and pressure is maintained by pressure regulators. This topology is a common approach in microfluidics. With this setup, it was determined that the channel could endure pressures greater than 30 psi, which was only limited by the compression level of the air introduced to the system.

The setup employs bypass channels for practical loading of both fluid and sample. By controlling the relative pressures between corresponding pressure vessels, the direction and rate of flow can be controlled. A U-style value enabled switching between the pressure-driven flow and an input port for manually loading the sample into the channel through a syringe. The bypass directed much of the sample into the waste path to ensure that the sample had adequately reached the inlet ports on the back of the silicon chip. The corresponding T-valve was employed to seal off the waste container and build pressure as determined by the driving pressure vessel.

On the other side of the device on the second port is another pressure vessel and a syringe pump. Another T-valve allowed for selection between pressure-vessel driven flow and involvement of the pump. By controlling the relative pressures across the microfluidic channel in the resonator device, flow could be controlled and sample introduced (with some limitations addressed further on). Rather than maintaining a set pressure as contributed by the pressure vessels, a syringe pump delivers a continuous flow rate. Since the flow rate in the syringe pump can be controlled on a minute scale (on the order of micro-liters per minute), the pressure differential appearing at the output port of the device can be controlled with high accuracy.

To stop flow and pressurize the channel, for calibration and testing, the syringe pump and waste channels could be removed (through their respective valve), and the pressure set by closely matching each pressure vessel.

Section 3.4: Optical Trapping and Detection Set-up

To implement both optical trapping and resonance detection, the system employs two independent lasers. Trapping and optical detection occur under microscope with 20–50X objective lenses, and the two beams are co-incident on the resonator through combination by a hot mirror, which transmits visible wavelengths and reflects infrared

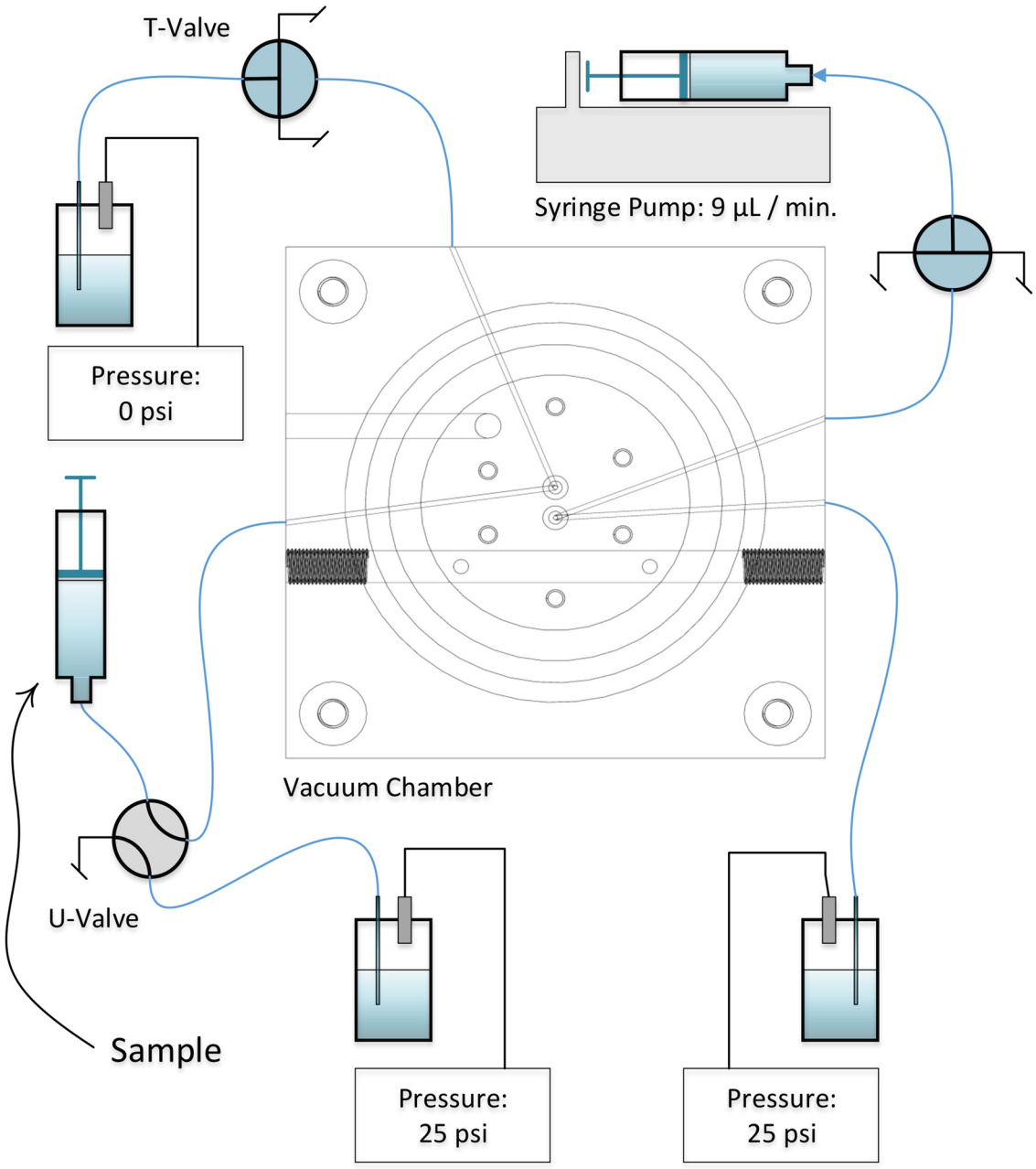

Figure 3.12. Microfluidic schematic showing four inlet and outlet ports and the peripheral connections to fluidic components.

(IR). The optical set-up is illustrated by Figure 3.13, showing two separate arms for resonance detection and optical trapping, along with the microscope.

A laser diode (<100 mW, nominally operated around 20 mW), temperature-controlled at 25°C by a thermoelectric cooler (TEC), serves in the detection of the structure's resonant frequency. After collimation and attenuation (or control of the laser diode current), the setup utilizes a linear polarizer, a quarter-waveplate (λ/4), and a polarizing-beam splitter (PBS) to maximize the intensity transmitted to the photodiode detector. By ensuring the correct orientation of the linear polarization, most of the light is transmitted through the PBS to the waveplate, which then converts the laser's polarization to a circularly polarized beam. After undergoing reflection from the resonant structure and propagating in the opposite direction, the handedness of circular polarization rotates the

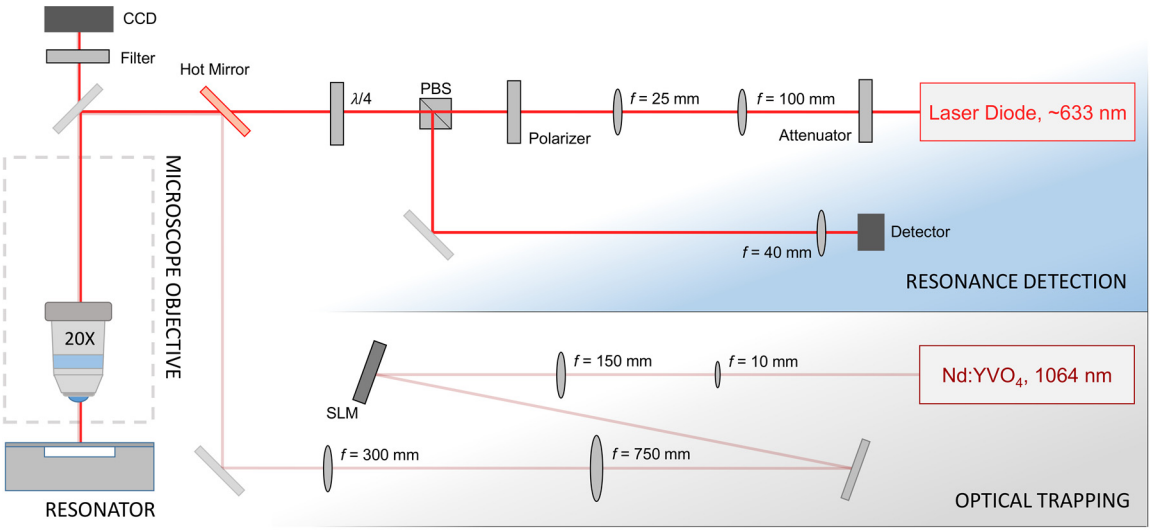

Figure 3.13. Optical detection and laser trapping scheme showing a laser diode (for resonance detection) and a Nd:YVO_4 laser (for trapping) co-incident under microscope on the resonator device. A spatial light modulator (SLM) is included for holographic trapping capabilities.

output linear orientation by 90° to maximize light reflection at the PBS and intensity at the photodiode. This ensures a better signal-to-noise ratio (SNR) of the detected output.

The second sub-setup involves a Nd:YVO_4 laser (5 W, 1064 nm) to enable optical trapping (laser tweezers) in manipulation of cells and particles on the resonator. A series of collimating and magnifying lenses combined with a spatial light modulator (SLM) shape and size the trapping beam. The SLM can holographically create arbitrary beam patterns at the focal plane of the microscope to allow for additional functionality and adaptability of the implemented trapping approach. Once the beam reaches the sample at the focal plane of the microscope, it has an intensity on the order of 10^3 $\mu W/\mu m^2$, depending on the utilized objective and laser current level.

Both lasers are introduced to the sample by a beam splitter adapted for both trapping and detection wavelengths. After collection by the objective lens, the light passed through a filter to a charge-coupled device (CCD) for digital image acquisition. The filter functions to reduce and block both lasers to maintain the microscope's imaging capability to see both the location of the resonator and the particles undergoing measurement.

Section 3.5: Electronic Detection, Feedback, and Control

The instrumentation system employs the conventional split-photodiode technique, often integrated in some derivative form for atomic force microscopy, to detect optical deflection in the resonant channel-beam structure. Optical readout promises a reduction in noise when compared to fully electrical-mechanical schemes that utilize capacitive sensing or similar methods. The photodiode serves to transduce the optical readout into the electrical domain with improved noise characteristics.

Due to a high level of diffraction from the structure, given the underlying photonic crystal platform, one active region of the diode is sufficient to detect the position of the highly sensitive diffraction pattern, and this movement can be proportionally related to the

structure's physical deflection. The drive voltage moves the structure only nanometers, and intrinsic thermomechanical fluctuations (when undriven) exhibit even further reduced movement. To detect this small signal, and ultimately amplifying it in a positive feedback loop, the detection circuit had to provide very high gain (on the order of 10^6) and demonstrate good noise and stability characteristics. Figure 3.14 describes a block diagram for the implemented signal detection, and the full circuit schematic can be found in the appendix (Appendix C: Detection and Feedback Circuit).

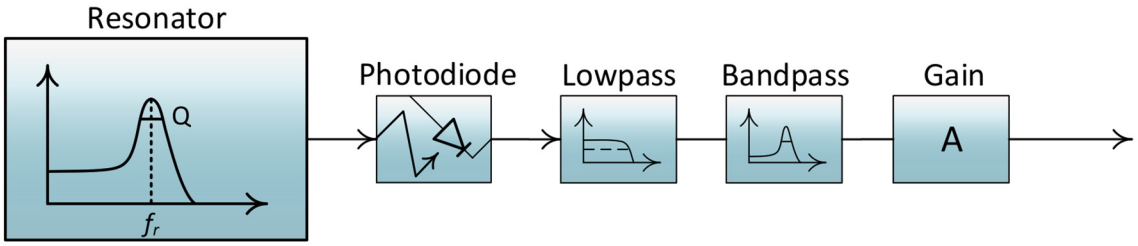

Figure 3.14. The optical detection circuit utilizes a photodiode and transimpedance amplifier with high gain, followed by additional stages for low-pass/band-pass filtering and amplification.

There are important tradeoffs between gain, noise, and bandwidth that require careful attention. The overall gain of the circuit is distributed across multiple stages for the sake of bandwidth, at the cost of overall circuit noise performance that accompanies an increasing number of sources. Resultantly, the circuit comprises adequate gain filtering and a bandpass filter to attenuate both low- and high-frequency noise signals around the structure's resonant frequency, especially those arising from ambient sources. Additionally, the circuit is well-decoupled from power source feedback and noise, while also utilizing a number of low-noise amplifiers with associated noise mitigation considerations.

In addition to designing for performance, the detection circuit had to interact with a feedback loop for driving the resonator. The feedback circuit is tasked with maintaining suitable and adjustable open loop gain and phase shift. In the closed-loop system, the MEMS resonator is the frequency determining element in the resulting oscillator, and the loop initializes through the detection of thermomechanical fluctuations in the structure. This signal is highly amplified and phase shifted by 90°, as discussed in the background (Section 2.5: Structural Damping and Resolution), and the conditioned signal is then fed back to the resonator electrostatic drive along with a necessary bias voltage to complete the loop. Given that the implementation is an unstable feedback loop and deflection amplitude stability is essential, the feedback gain is managed by a proportional-integral-derivative (PID) controller around some amplitude set point. This setup drives the structure to its natural resonant frequency with a fixed deflection; in this way, the resonator is continuously driven at its resonant frequency which shifts according to mass changes during measurement. Operating in closed-loop feedback, Figure 3.16 records the detected signal, its phase-shifted output, the root-mean-square (RMS) voltage of the signal, and the control level for the variable-gain amplifier; for this particular structure, the resonant frequency is tracked around 250 kHz. Finally, Figure 3.15 shows the block diagram composed of components for detection, feedback, control, signal conditioning/protection, and data acquisition.

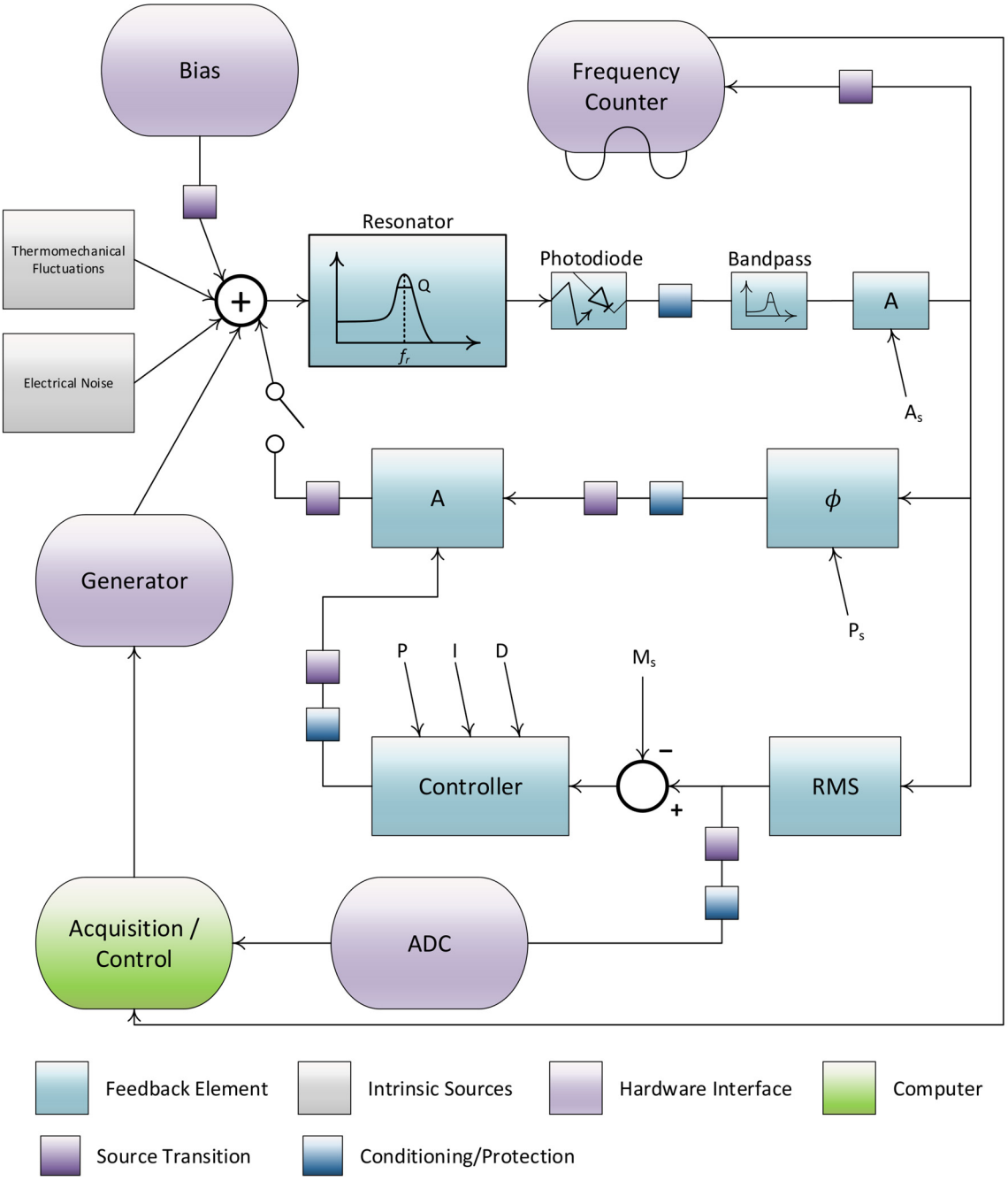

Figure 3.15. A block diagram showing the full system comprising detection, a gain-controlled feedback drive, monitoring, and signal conditioning. (The complete circuit can be found in the appendix.)

Given that feedback perpetually operates the device at resonance, all that is left to do is observe the frequency of the signal output. Addition of a frequency counter gives a stable and precise frequency reading that depends on the set gating time. Through serial communication with acquisition software, the resonant frequency can be monitored in real-time to show the response of the structure to changes in mass induced from sample measurements.

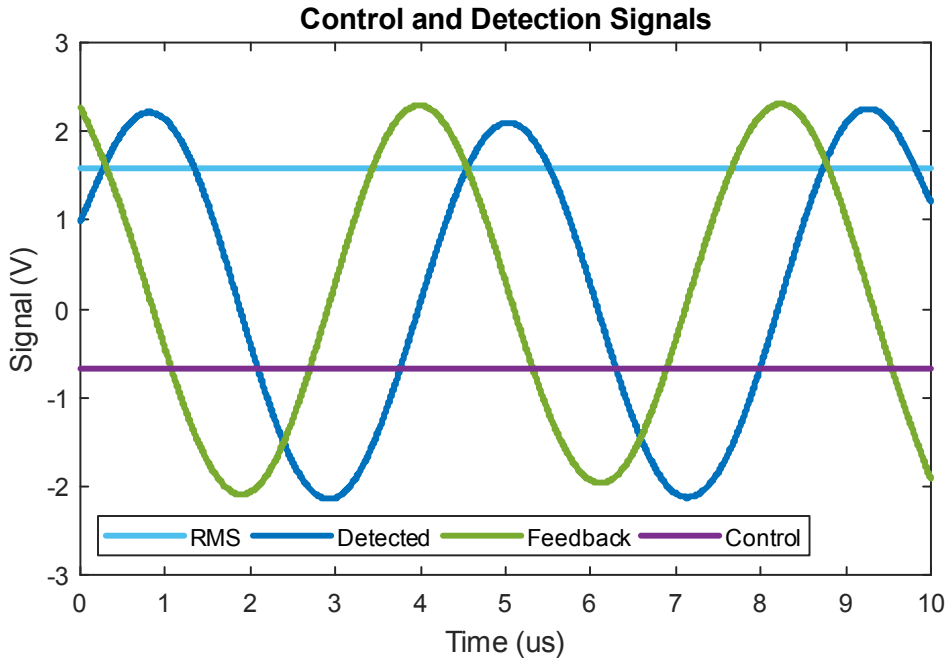

Figure 3.16. Resonator response under feedback. The blue curve shows the output of the photodiode and gain stages; the green curve shows the phase-modulated signal, shifted by approximately 90°; the light blue curve indicates the measured RMS value of the detected signal; and the purple curve is the control signal output from the PID controller

For purposes of testing and frequency-domain analysis, especially important in characterizing the quality factor and response, the circuit can accommodate a direct drive topology. By utilizing a stable frequency source, such as an arbitrary function generator, the resonator can be driven at frequencies around its resonance to obtain the frequency

response and aid in obtaining alignment/conditioning with sufficient SNR for closed-loop operation. The RMS value of the signal is digitized by an analog-to-digital converter (ADC) and plotted against frequency.

Section 3.6: Complete Set-up and Data Acquisition

The complete setup involves the combination of all sub-systems described in the preceding sections. Figure 3.17 shows two video frames depicting the resonant-bridge device filled with fluid, substantiating maintained channel visibility and transparency. The red readout laser is visible on the structure; since fluid changes in the channel incite significant refractive index changes, an offset of the laser avoids signal intensity changes due to the presence, or lack thereof, fluid. The inset plot shows a real-time characterization of the resonant frequency, validating frequency shifts arising from fluid movement in and out of the structure. The signal is monitored, processed, and plotted by software written in C#, provided in the appendix (Appendix D: Setup Control and Data Acquisition Software).

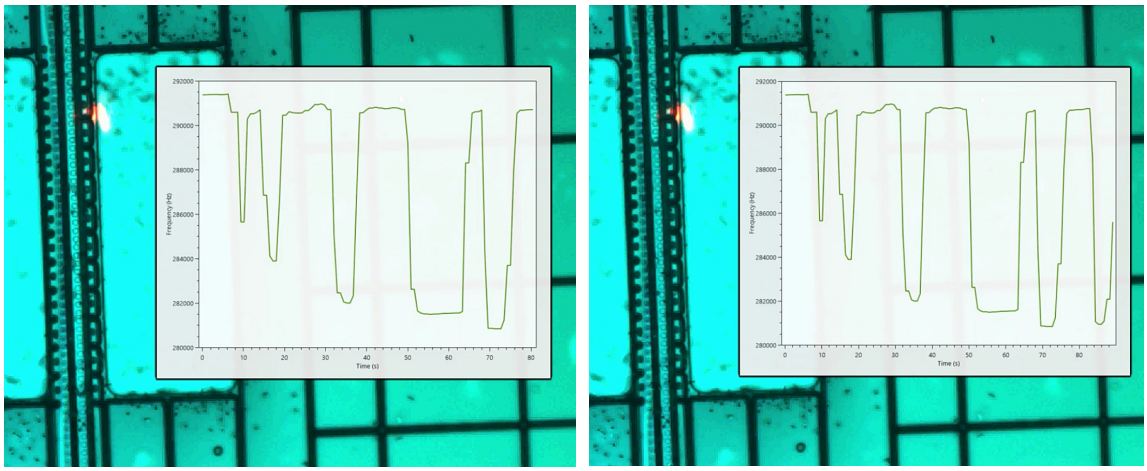

Figure 3.17. Real-time resonant frequency measurement of water propagating along the device channel at two instants in time. An empty structure has a higher resonant frequency, and as water fills the device, the resonant frequency decreases, with increasing mass.

Figure 3.18 shows a sample loaded in the vacuum chamber fixed underneath the microscope; the image also shows the microfluidic, optical, and electronic peripherals that enable measurement and support structure operation.

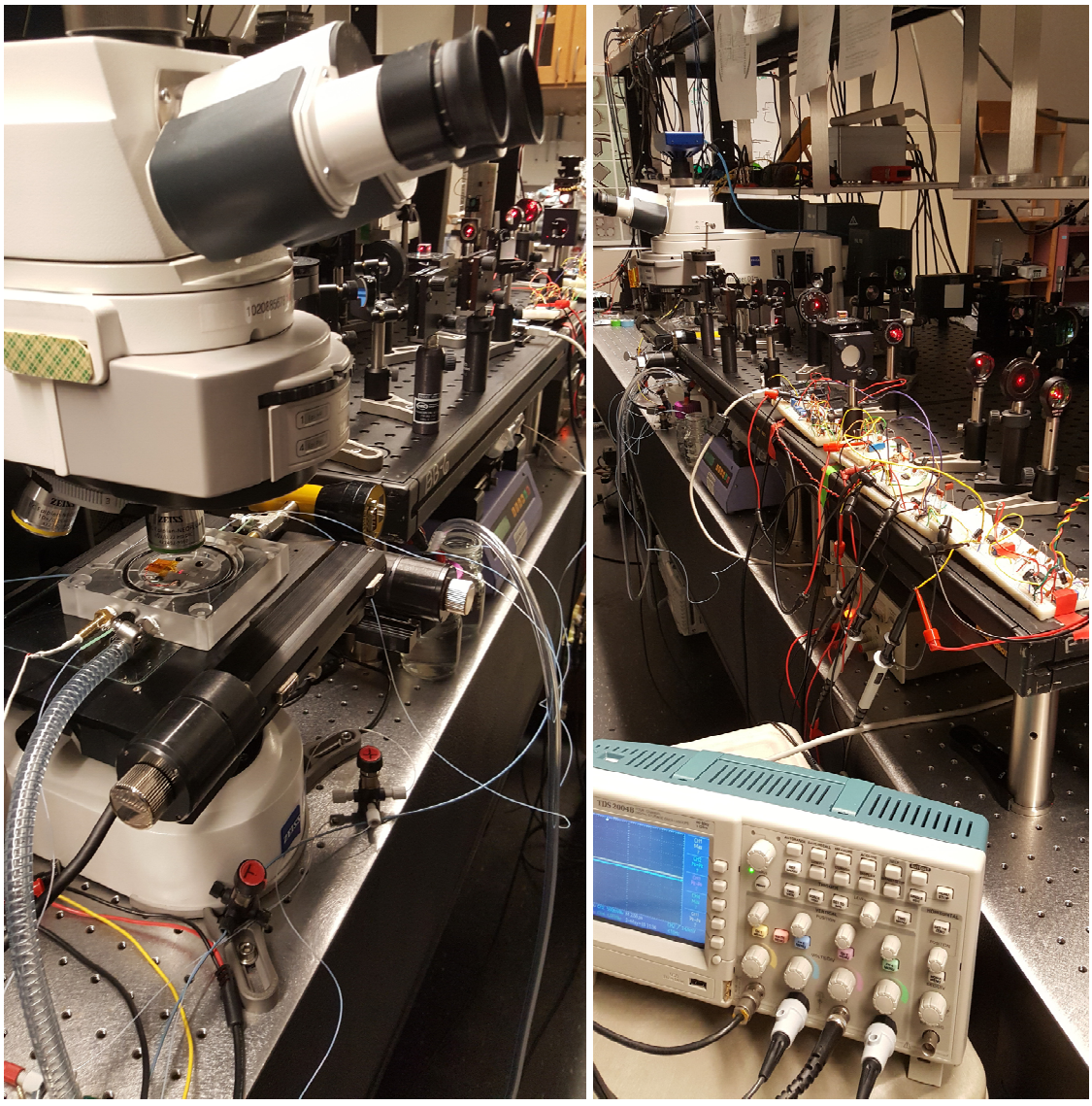

Figure 3.18. The complete setup showing the vacuum chamber with a device, the microfluidic connections, the optical set-up, and feedback/ detection circuitry.

With the hardware and software systems implemented, the first test sought measurement of samples injected onto the structure. Since oil has a significant mass when compared to water, oil droplets were guided onto the structure. Figure 3.19 shows the resulting resonant frequency shifts that produced large downward shifts as the droplets passed over the structure, demonstrating successful measurement and validating the system and its sub-components.

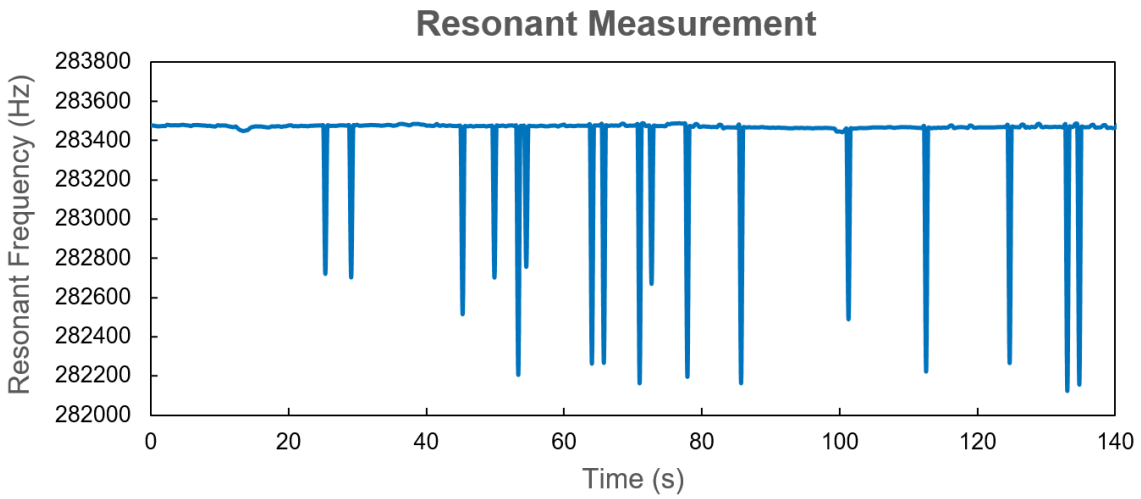

Figure 3.19. Real-time resonant frequency data showing the response from oil droplets (displacing water as a higher density medium) that create observable resonant-frequency downshifts.

Of course, density contrast in the case of cells/particles results in a significantly reduced response, when compared with fluid or oil-droplet loading. Therefore, frequency stability becomes essential in their observation. Figure 3.20 shows the stability progression of the system. Without feedback, employing only direct drive, early data acquisition software and necessary sample averaging was only capable of measurements with a sampling rate of minutes, which is effectively useless for the required dynamic measurements. Improvement to both the circuit and software greatly improved the sampling rate, but still demonstrated high frequency variance. As is clear in the final plot

(and error distribution) showing the results of feedback, data acquisition becomes nearly real-time depending on implementation with a couple-order quality factor enhancement and a stability on the order of single Hertz.

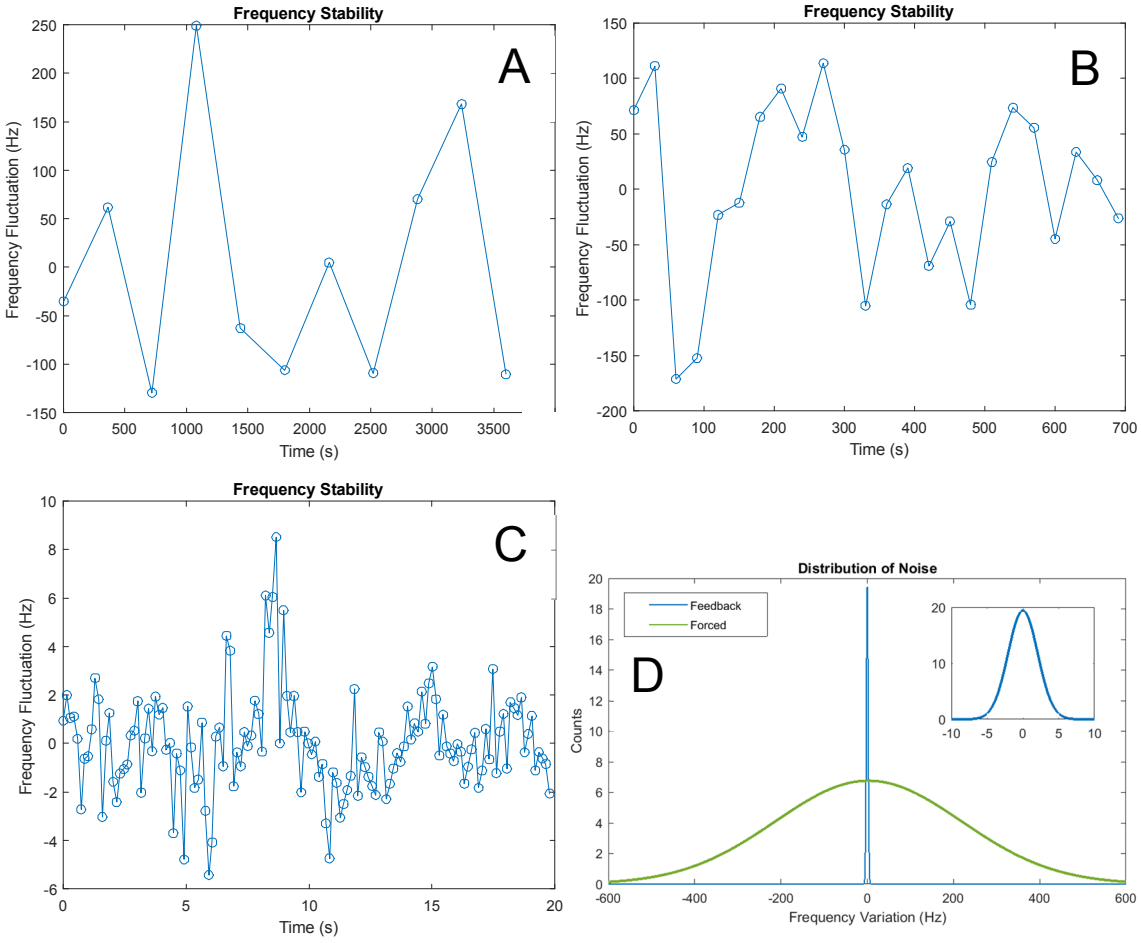

Figure 3.20. Each plot shows frequency stability over time. The first two figures show the result of direct-drive frequency measurements. The original acquisition system (A) acquired data rather slowly, which impeded practical characterization experiments. (B) Improvements to the system allowed for a slight improvement to stability, but greatly increased the rate of data acquisition. (C) Feedback-drive allowed for real-time measurement of the resonant frequency with a couple-order enhancement to frequency stability. (D) Feedback-drive improves frequency stability by a couple-orders when compared to direct drive.

Chapter 4

Fabrication

Fabrication of a suspended silicon structure is relatively straightforward with silicon-on-insulator (SOI) techniques [86] [87] [88]; a simple masked dry etch of the device layer and a subsequent wet etch of the oxide sub-layer can produced released, suspended structures. A SOI approach is especially prescribed when tight uniformity and dimension control is of concern. The single-crystalline silicon comprising the device layer offers excellent mechanical properties (including low intrinsic stress) over amorphous materials such as silicon nitride or polysilicon. Furthermore, single-crystal silicon has a low intrinsic loss, and from a material standpoint, it promises potential for high Q-factor devices [89].

SOI processing is not without its challenges and considerations, however. Given the requirement of perfectly smooth bonding surfaces during the formation of SOI wafers, one limitation on device dimension and available process strategies is stiction [90], where the two highly defect-free surfaces permanently stick together after release [87]. The subsequent fabrication process empirically optimizes viable dimension ranges and implements various stiction mitigation strategies, detailed further on. Departing from the work of others and common methods, a unique fabrication challenge arises from the optical configuration necessitated by this research, which requires surface-machined, transparent microfluidics extending over a silicon PhC as part of a released silicon-bridge structure and actuatable via electrostatics.

Previous resonant and hollow devices resulted from silicon nitride and a polysilicon sacrificial process [6] [91]. While silicon nitride is optically transparent, it requires deposition of opaque metal electrodes to electrostatically actuate the structure. Additionally, depositing thick polysilicon layers that approach the scale of mammalian cells can pose significant challenges, and the stability of nitride in many processing chemicals, its method of deposition/formation, and its etch selectivity limit the number of viable sacrificial materials. Additionally, a sub-micrometer, suspended nanochannel microbridge was fabricated using complementary metal-oxide-semiconductor (CMOS) technology [92]. To exploit the desirable properties of single-crystal silicon and achieve significantly larger channels, devices were developed through the creation of buried channels in bonded SOI wafers, to produce a hollow silicon cantilever [8]. The structural simplicity of this approach boasts a very high quality factor and excellent mechanical properties. However, as previously discussed, silicon is not transparent in the visible wavelength band or at optimal biological wavelengths, including those for trapping.

Section 4.1: Device and Channel Process

The target of this work is the achievement of a platform compatible with arbitrarily sized cells providing optical accessibility inside of the resonator at optical and near-infrared frequencies. This constraint excludes common methods of forming and connecting microfluidics, including various bonding and burying methodologies. At the same time, more appropriate surface-machined channels impose inhibitive constraints in macroscale fluidic integration. To address this concern, the fabrication process has observed two opposing configurations in an investigation into the viability of such a platform, described in the next sections.

A simplified, top-view architecture is shown in Figure 4.1, in large part shared by the two processes. The layout describes the fluidic channel spanning between two fluidic

inlet and outlet ports (to be discussed in the subsequent sections). This channel extends across a micro-scale bridge structure equipped with PhC surface structuring, and the entire fluidic geometry is surrounded by parylene anchor sites that are necessary for attachment and fluid confinement. Later sections will address the design and layout of these anchor fields for optimum reliability. Finally, electrode pads are shown on the device layer to establish an electrical connection to the silicon bridge structure to facilitate electrostatic actuation. The complementing electrodes for the substrate layer are not shown.

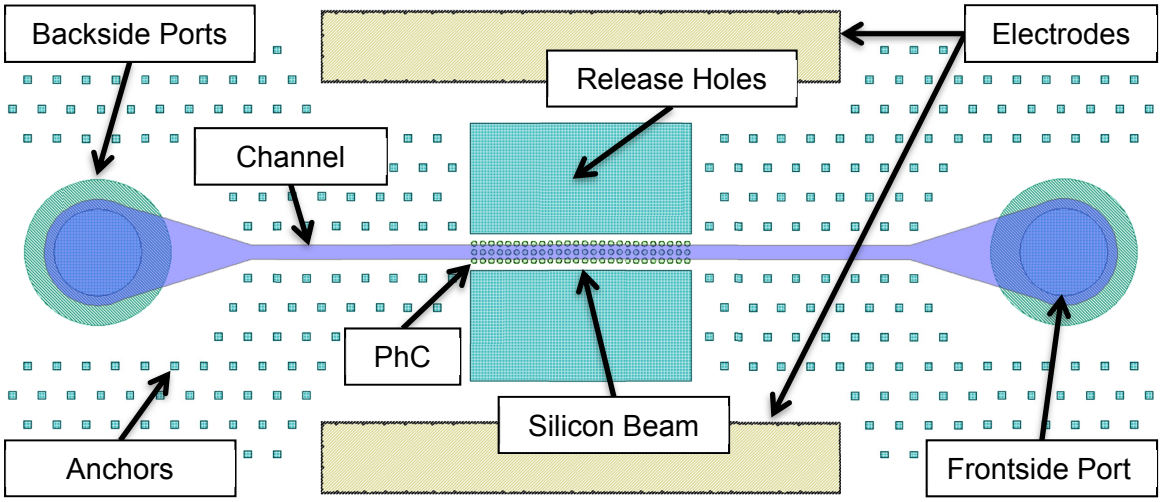

Figure 4.1. A simplified top-view architecture showing the fluidic channel in blue, parylene anchors, gold electrodes, and port release holes on both the front and backside.

The device layer of the SOI wafer determines the thickness of the fabricated beam, with nominal 2-µm device and 5-µm oxide layers to achieve the desired resonant frequency and electrostatic spacing. The silicon device layer supports a photolithographically defined PhC pattern, consisting of shallow holes imposed by an inductively-coupled plasma reactive-ion etch (ICP-RIE). This etch process transfers the PhC pattern into the silicon device layer with a vertical side-wall profile and a depth of about ~250 µm. Following this step is a reactive ion-etch (RIE) stopping on the buried oxide layer to define the beam

structure and anchor sites, that facilitate later beam release and parylene deposition, respectively.

While silicon serves as the structural, integrated-optical component, parylene-C confines fluid on the structure as the fluidic channel material. On its own, parylene-C typically has poor adhesion to other materials, including silicon, and cannot withstand severe or abrasive environments [93], rendering parylene a challenging material to process. A mitigating strategy adopted in this work to ensure reliable, robust fluidic channels, employs mechanical anchors below the silicon device layer for attachment of the parylene, which is important in determining the maximum fluidic pressure supported by the device and its reliability. This work utilizes the conducive structure of the SOI wafer to construct these anchors, but other published approaches have implemented them using a modified Bosch process [94]. The buried oxide lends itself readily, where etching exposes the oxide and a timed hydrofluoric (HF) etch creates inverted mushroom-like cavities, without the need for implementing a more involved plasma etch process. Parylene then fills these voids to generate points of fixation for the layer. This mechanical attachment is the most vulnerable link in the fluidic structure, and therefore, becomes the determining factor in fluid pressure ratings for the device. Figure 4.2 shows a cross-section of an undercut anchor cavity and its structural reliability during abrasion testing. Parylene adhesion is not only a consideration for substrate attachment, but also affects subsequent processing steps. A layer of parylene can impair photoresist spinning, notably for severe surface topologies, and it has a comparably low thermal budget, prohibiting many etching and baking process steps. The addition of a patterned aluminum layer can help with some of these thermal issues as well as ensure sufficient masking on highly topological features.

Given a method of securing the parylene, channel formation requires a sacrificial process. Such processing has seen important development over the past couple decades [95] [96] [97] and has critical utility in this work. Photoresist is easily patterned and readily dissolved in a host of solvents, and its cross-sectional profile can even be controlled through resist reflow [98]. To this end, patterned thick photoresist defined the height and

width of the channel; as a result, these dimensions are easily adaptable to suit various application requirements and cell types. Upon establishing this layer, chemical-vapor-deposited parylene then coated the structure, encapsulating the beam resonator and the sacrificial photoresist, while simultaneously filling the cavity anchor sites for attachment. A long HF etch removes the supporting buried oxide sublayer to fully release the beam-channel structure, followed by a final solvent release of the sacrificial photoresist. There is an optimization required during the HF etch step, one that minimizes etch time. The process has to ensure a long enough etch duration to fully release the structure; however, the longer the etch time, the deeper the adjacent substrate becomes undercut, which is unavoidable with a wet etch process. This undercutting leads to increased damping on the structure and an increase in effective structural mass, both detrimental effects in terms of mass sensing and frequency resolution. Therefore, careful etching is warranted for increased device performance.

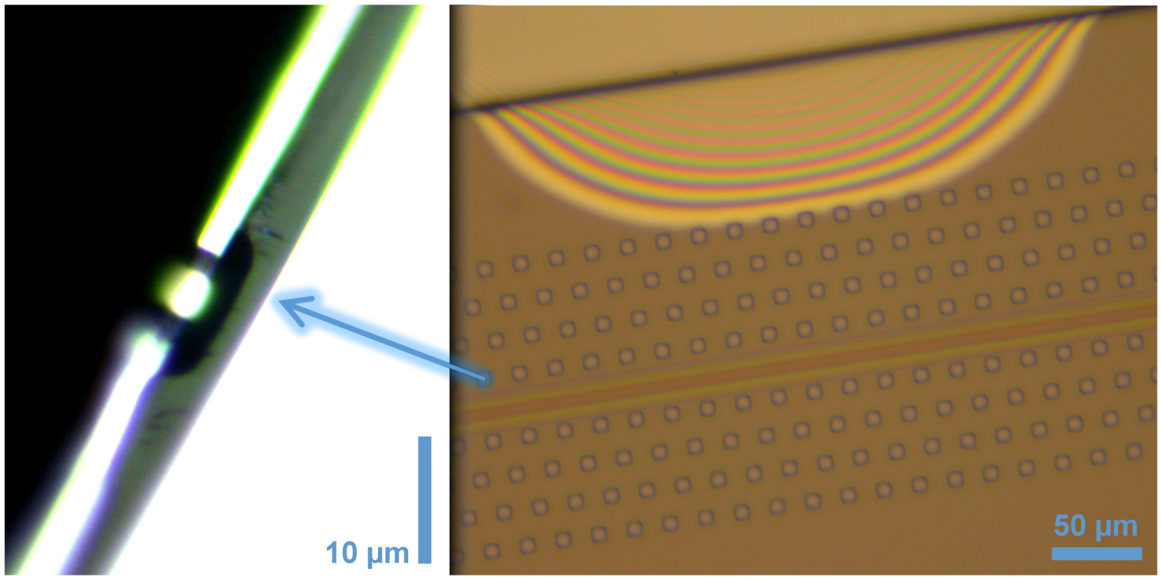

Figure 4.2. The left cross-sectional image (A) shows HF undercutting of the oxide layer at each anchor site in the right image (B), which demonstrates maintained parylene adhesion during abrasion.

The preceding fabrication methodologies can produce viable channel structures integrated on a bridge resonator that possess optical clarity; however, porting to this microchannel and erecting the necessary structures posed significant integration challenges, especially when interfacing with the macroscopic world of fluidic connectors, samples, and pumps.

Section 4.2: Frontside Porting

The first approach sought port structures on the surface of the device, to reduce cost and complexity of the fabrication process. Figure 4.3 represents the critical fabrication stages, excluding standard photolithography or conditioning/cleaning steps. A more detailed process is included in the appendix (Appendix B: Detailed Frontside Process Flow). In linear review, photolithography defines the PhC etch mask for the ICP-RIE process. Especially for adherent cell measurements, surface depressions arising from the photonic crystal can be non-ideal. To circumvent this surface roughness, a planarizing layer can be deposited and patterned. Upon first pass, silicon nitride appears a suitable candidate for this purpose given its optical characteristics and compatible deposition through plasma-enhanced chemical-vapor deposition (PECVD). However, silicon nitride has poor stability in HF acid, and results in a rapid undercutting of the parylene channel during final release. Therefore, a more stable, chemically-deposited, and patternable material is warranted. Parylene serves this purpose well and can find its implementation during general processing steps or in a final internal parylene deposition with appropriate inlet and channel design.

A frontside RIE then establishes the beam structure and parylene anchors by etching to the oxide stop layer. Utilizing this sublayer oxide, a subsequent timed HF wet etch creates cavities, followed by spinning and patterning a thick photoresist for sacrificial development of the parylene channel. Parylene is then chemical-vapor deposited,

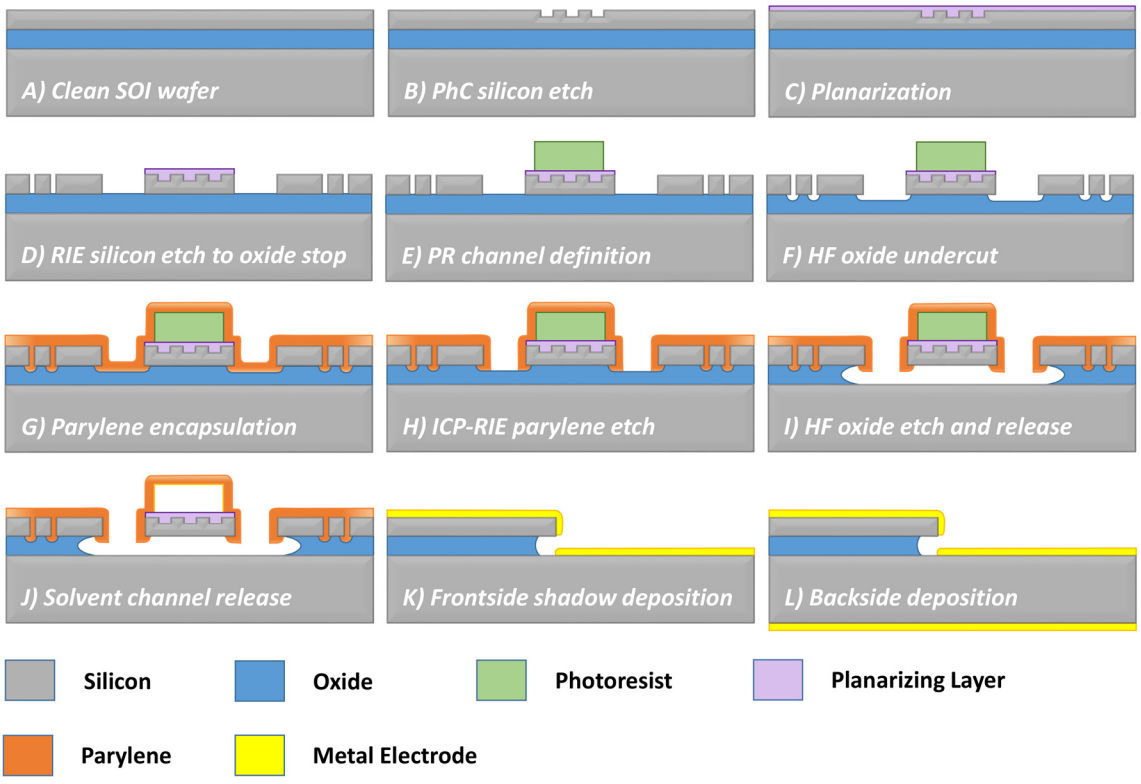

Figure 4.3. Fabricate diagram where feature dimensions are not drawn to scale and exaggerated for clarity. (A) The process starts with a clean SOI wafer. (B) An ICP-RIE silicon etch transfers the PhC pattern to the silicon device layer. (C) A planarizing layer is deposited on the structure. (D) A RIE process etches the silicon down to the oxide stop layer to define the resonator and the parylene anchors. The planarizing layer is patterned in an additional step. (E) A photolithography process utilizing thick photoresist defines the device's channel structures. (F) A short HF etch of the oxide undercuts the silicon device layer to create anchor points for subsequent parylene processing. (G) A conformal parylene deposition encapsulates the photoresist and resonating structure. (H) An ICP-RIE etch through the parylene reveals the underlying oxide layer and opens ports to the channel structure. (I) A HF wet etch fully undercuts and releases the structure to produce the free-standing resonator, and (J) the channel is released in acetone. Finally, electrodes are deposited on the frontside using a shadow mask and inherent isolation (K) and on the backside (L).

encapsulating the beam resonator and the sacrificial photoresist, forming strong anchors in the SOI wafer. An oxygen ICP-RIE etch opens access through the parylene layer to the exposed oxide while simultaneously defining input and output ports for the fluidic channel on the wafer's topside. HF wet etching then fully releases the structure, and a final solvent release of the photoresist leaves freestanding, transparent fluidic channels atop the integrated PhC and silicon beam resonator.

The port pictured in Figure 4.4 was surface machined according to this prescribed process. Due to its deformability, it prohibited surface attachment techniques, instead experiencing abrasion or channel pinching. Additionally, due to parylene's weak surface bond and the released MEMS structure, additional processing required for a SU-8 (or similar) interfacing layer become intractable.

As a final step, metal electrodes (gold pads with a chrome intermediate layer) were deposited using a shadow mask over the structure. By virtue of the oxide undercutting and the separation between the device and oxide layers, the substrate and device electrodes could be implicitly isolated. To facilitate contact with the chip holder, a metal electrode layer was also deposited on the backside. While convenient for electrode isolation, this overhanging edge could become very fragile depending on the amount of undercut. If this edge fractured, it could easily short the two layers due to a high level of silicon doping and prevent electrostatic actuation, an especially imposing problem for biasing the device. To mitigate this issue, the device layer and substrate layer could be specified to have separate doping impurities such that one is n-doped and the other p-doped. In this way, if a break in the structure brings the two layers into contact, a p-n diode junction results. Careful selection of the bias polarity can then reduce shorting between the layers.

With these early port structures, the most reliable method of filling the microchannels exploited capillary action and surface tension to draw fluid from one port through the fluidic channel to the opposing port. While this capability was important to demonstrate the channel's fluidic seal and potential; it was unsuitable for fluid-mediated

experiments, requiring prior evaporation to accommodate the vacuum environment. Moreover, dictated by microfluidic dimensions, the channel was incompatible with certain characteristic fluids including water, due to their high surface tension. Fluids exhibiting lower tension, such as isopropyl alcohol, enabled channel testing utilizing the capillary approach, but was limited by its rapid evaporation rate. This restricted control did allow for short-term optical trapping tests and particle placement on the structure during evaporation for subsequent vacuum chamber experiments, leading to validating and guiding results.

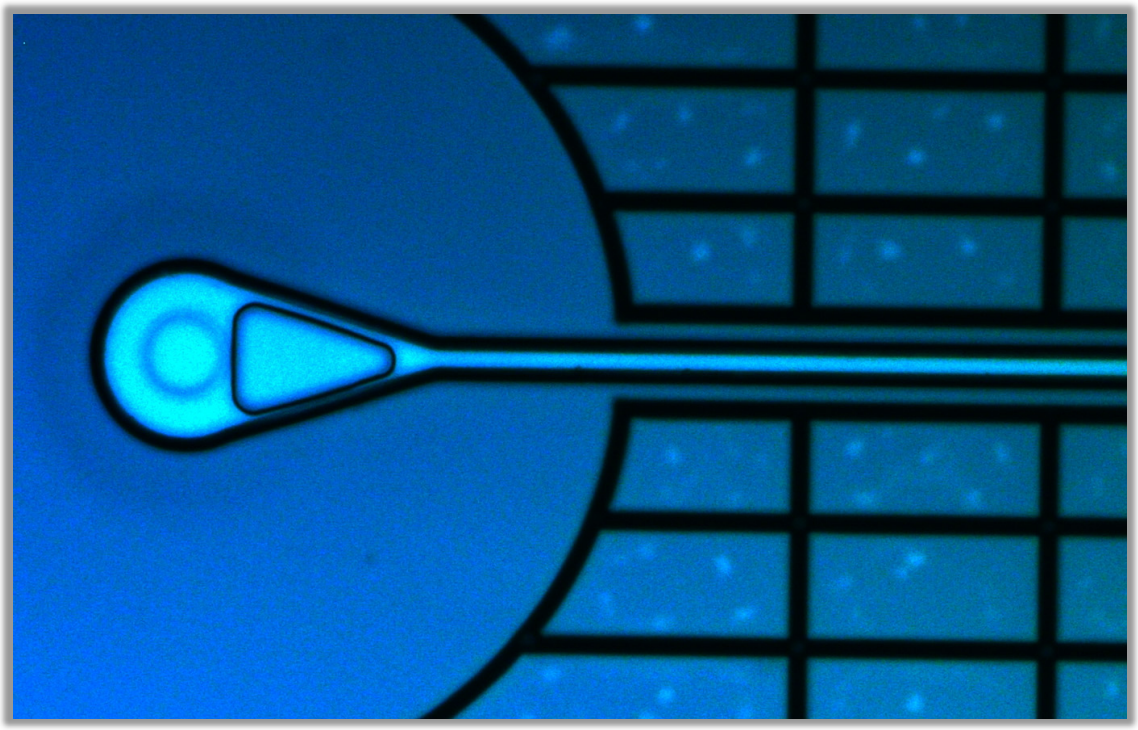

Figure 4.4. Micrograph of a surface-machined parylene fluidic port opening on the wafer's frontside, surrounded by parylene anchors to confine fluid to the channel.

Of course, fluidic control inside of a vacuum is essential to serially interrogate cells and particles with high fidelity. As a solution, the next section describes an approach to establish backside ports as a more robust alternative. The backside of the silicon wafer is both a smooth and stable interface that mates well with external fluidic connections. In this way, such a configuration can serve to better convey fluid and analyte, which is critical to the aim of this research: stable and long-term biological study.

Section 4.3: Backside Porting

The frontside process had serious shortcomings in the attachment of fluidic connections, but served to validate the bridge-channel resonator concept. This section will discuss a backside port process that obtained a more robust attachment to the previously described vacuum chamber.

The backside process incorporates many similar steps to the frontside and general process. After establishment of the PhC, the frontside of the wafer was protected by a layer of photoresist, to reduce potential damage to the delicate optical structures and to serve as a safety barrier for through wafer etching. Photolithography defined a pattern on the backside of the wafer to define the ports, and a deep reactive ion-etch (DRIE) etch opened fluidic passages in the backside of the wafer. By utilizing a Bosch process, the port channels can be cleared through the wafer with good verticality, which is critical to the dimensions of the resulting frontside membrane. The thick insulating oxide ensures the integrity of the frontside structures (by managing thermal stress) and accurately determines etch depth as a stop layer. The buried oxide then constitutes a surface, or membrane, on which sacrificial resist can be later spun and processed for channel formation. By way of the eventual HF release and resist scaffold, these ports subsequently connect to the frontside fluidic network, thereby allowing robust connection on the wafer's backside.

Anisotropic wet etching is another method for through wafer etching, using either potassium hydroxide (KOH) or tetramethylammonium hydroxide (TMAH) [99]. In such a process, the etchants usually attack exposed (100) oriented silicon planes, guided inward by the (111) plane at a 54.7° given its much reduced etch rate along this crystal axis. With a masking material, such as silicon nitride (low-pressure chemical vapor deposited, LPCVD) or thermal oxide, a geometrically corrected pattern can transfer to a membrane on the opposing side. Wet etching can be significantly cheaper, especially given its suitability for batch processing; however, the required masking layers and mask etch selectivities [100] rendered this method difficult to implement in the current process, requiring additional processing steps to remove the mask layer without affecting the supporting oxide membrane. Further, the major deterring factor is the form that the resulting membrane takes. This structure must withstand many additional processing steps to become a permanent fixture in the fluidic channel. In addition to parylene integrity and attachment, this membrane has a limiting effect on the overall pressure allowed by the device. Therefore, careful design of this membrane is important to fluidic specifications, and a circular membrane demonstrates lower stress at its edges than rectangular or square membranes for a given pressure [101]. The simulation in Figure 4.5 shows the high level of stress that occurs at the edge of the structure under a 60-psi load for both the oxide supported and released silicon membranes. When the released case experiences a pressure greater than 150 psi, the edge stress nears that of the silicon yield strength, 7 GPa [102], and the structure can become permanently deformed, toward the eventual state of fracture. This constraint combined with that described for parylene (in Section 3.1.2: Channel Structure) yielded maximum fluidic pressure and flows supported by the devices, measured to exceed pressures of 30 psi (limited only by the compressor) and constrained to pump flows less than 15 μL/minute.

After forming the through wafer ports and associated membranes, the process then defines and etches the parylene anchors and the silicon beam as before. In later generation devices, various anchor designs and layouts were considered, each with various drawbacks

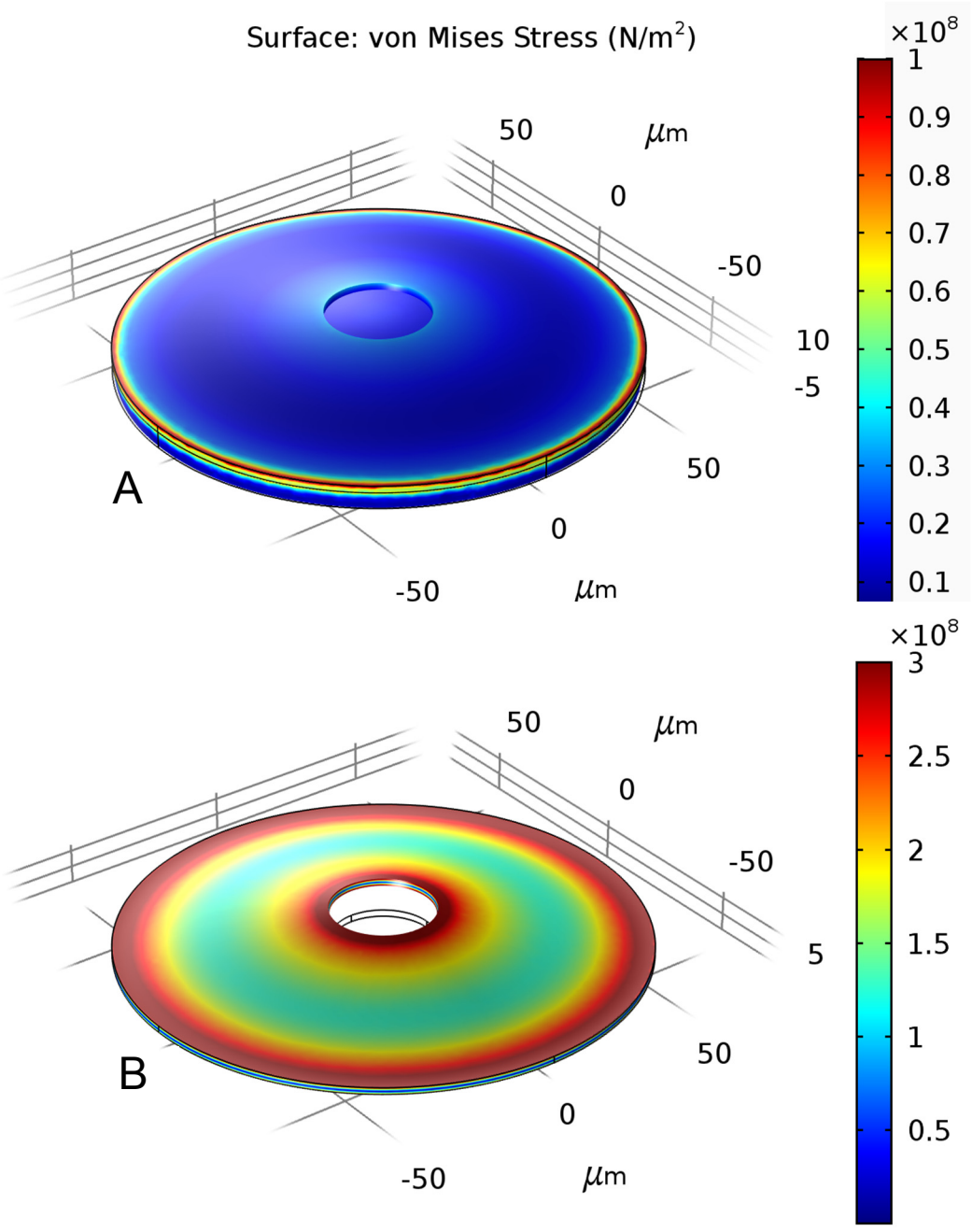

Figure 4.5. Simulation showing stress (for the composite silicon and silicon dioxide membrane, A, and released silicon structure, B) in response to a 60-psi pressure. The maximum stress occurs along the edges.

and limitations. Linear trenching achieved a better fluidic seal, superior to discrete, scattered openings. However, one must carefully consider the mask design to ensure that these trenches do not render the device electrically isolated from the electrodes since the silicon device layer is being etched away. In final designs, for both reliable anchoring and electrical continuity, the anchors included both linear trenches and discreet holes with regions of redundancy to ensure device operation in states of localized failure or in response to fabrication defects.

In harmony with the frontside process, the combination of a deposited photoresist layer and parylene encapsulation next yields patterned channel structures. It is critical that the backside of the wafer is sealed (with an adhesive layer) to prevent parylene deposition within the porting structure; otherwise, this layer would prohibit dissolution of the oxide layer and block fluid flow. For additional protection of the parylene channel during etching, especially for taller features and more extreme topologies, a layer of aluminum was blanket deposited over the photoresist for enhanced protection and thermal management during parylene etching, which is most critical at the channel's apex where the photoresist becomes its thinnest.

As before, an ICP-RIE etch removes exposed regions of the parylene, and a final HF release again undercuts the beam structure, dissolves the oxide membranes, and removes the residual aluminum film. Finally, acetone opens the fluidic channel network via the backside. A scanning electron microscope (SEM) image of the channel cross-section is shown in Figure 4.6, and a final fabricated device can be seen in Figure 4.7, where a released parylene channel supports propagating fluid flow and the inset image shows the beam resonator without a parylene channel for an unobstructed view of the underlying photonic crystal. Figure 4.8 illustrates the critical steps required for the backside approach, and a full process is enclosed in the appendix (Appendix A: Detailed Backside Process Flow).

Since the device was required to mate with fluidic connections in the bottom of the vacuum chamber, both device and substrate electrodes were implemented on the frontside,

with connection to the chamber probe and the mounting plate, respectively. A photolithography liftoff process created a metal electrode stack on the device, composed of chrome, nickel, and gold. Chrome served as an adhesions layer; nickel provided a reinforced pad for better strength and durability during probing; and gold established good conductivity. The substrate electrodes were again deposited using a shadow mask method, with isolation still maintained by the overhanging edge. Due to the fragile nature of this edge, careful addition of a surrounding epoxy bead ensured electrical and mechanical integrity, which is especially essential during loading and unloading from the chamber mount.

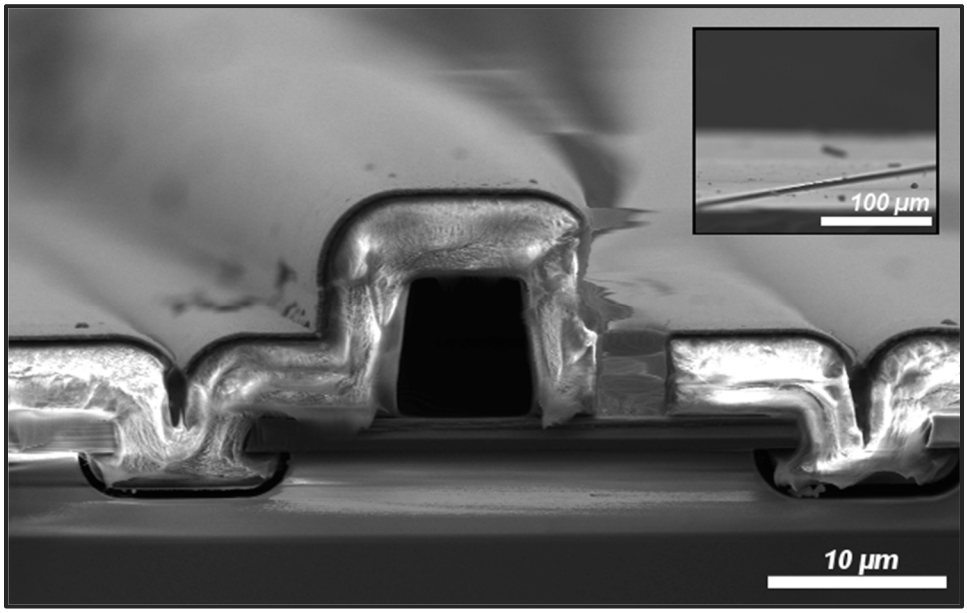

Figure 4.6. SEM micrographs of the channel and its cross-section identified by the released parylene structure and the adjacent anchors underlying the silicon device layer. Blanketing the parylene layer is a thin aluminum film to provide electrical and thermal conduction as an imaging aid.

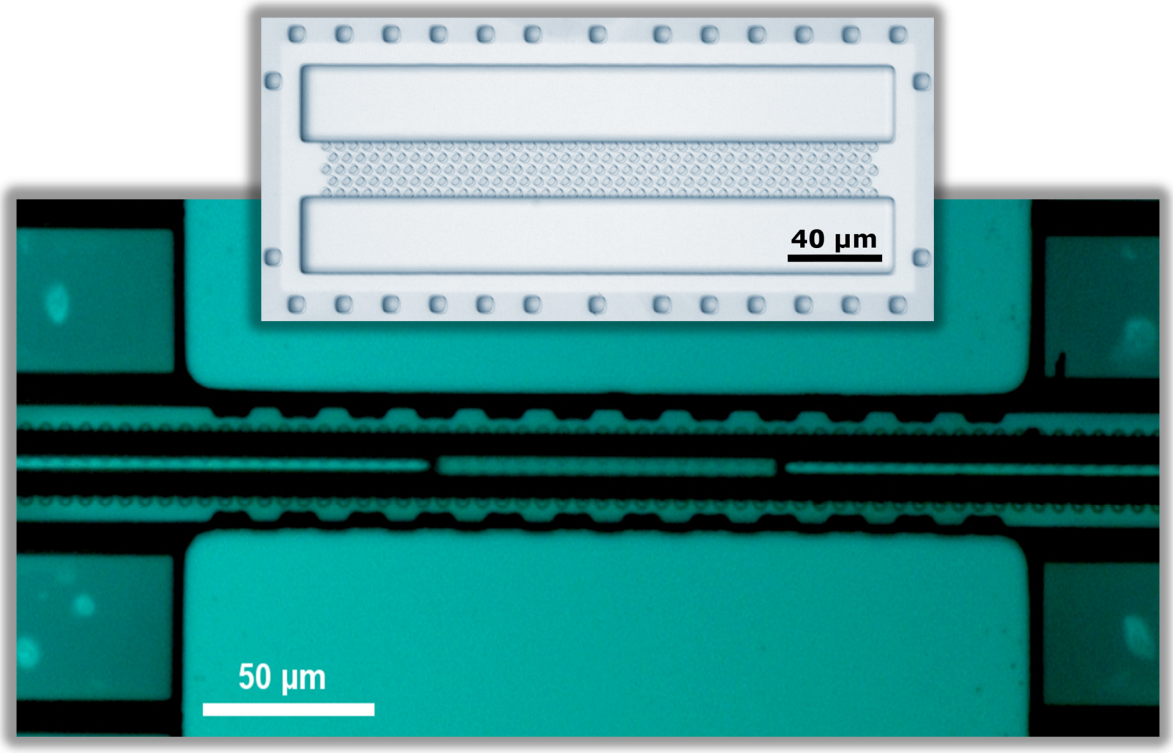

Figure 4.7. (A) An enlarged image of the bridge resonator without the channel to reveal the underlying PhC pattern on the silicon beam. (B) Image of the fully integrated parylene channel structure showing trapped fluid and the underlying PhC.

For the frontside devices, fluid is restricted to contact with the device layer only. However, for the through-hole ports, since fluid enters the structure from the backside and moves to the frontside, it can create a conductive pathway between the two layers and their respective electrodes, shown in Figure 4.9(A). Fluid conductance can become especially pronounced for cell media, which comprises many ions and salts necessary for cell culture and survival. Conducting ions through the fluid leads to electrolysis, which creates both hydrogen (H_2) and oxygen (O_2) gases [103], filling the channel with bubbles. These bubbles disrupt sample observation in the channel, and their compressibility render fluid flow unstable and difficult to accurately control.

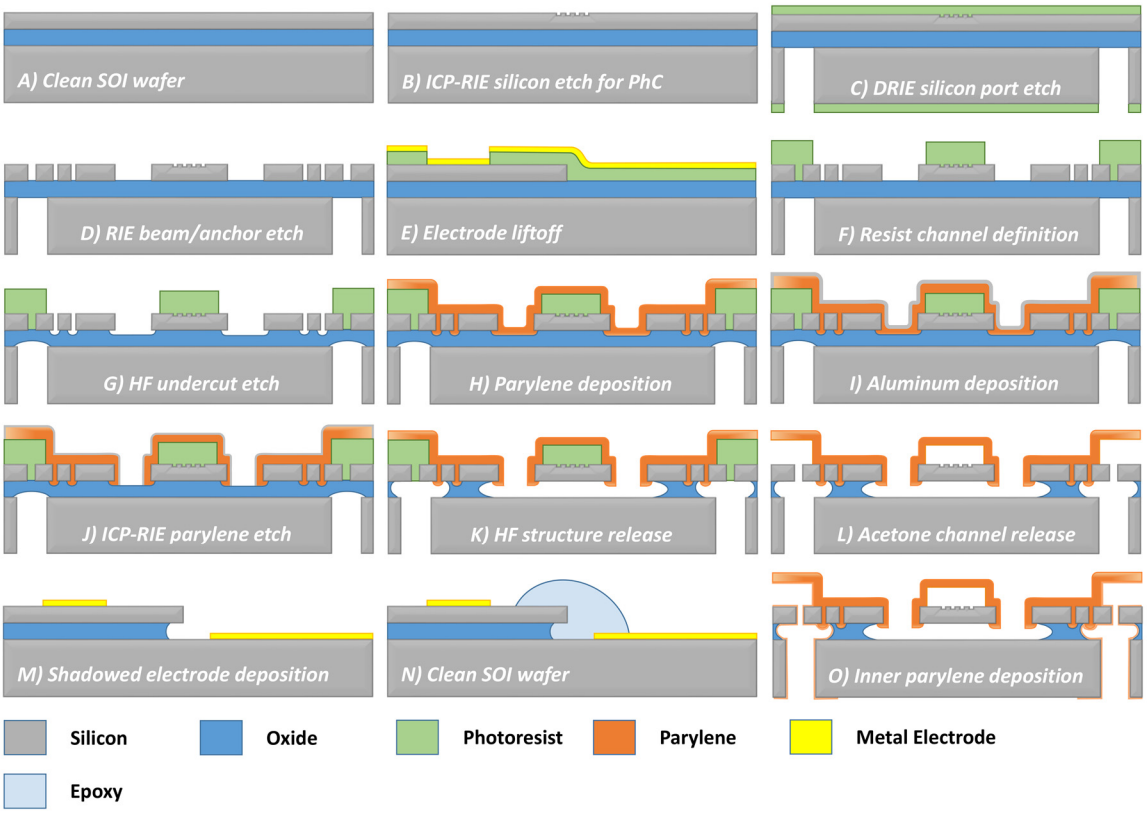

Figure 4.8. Fabricate diagram (with unscaled, exaggerated feature dimensions): (A) Starting with a clean SOI wafer, (B) an ICP-RIE silicon etch transfers the PhC pattern to the silicon device layer. (C) Both sides of the wafer are protected with photoresist, and a DRIE step etches port features through the handle wafer to the buried oxide layer. (D) A RIE process etches the silicon device layer to the oxide stop layer to define the resonator and the parylene anchors. (E) A liftoff process deposits a metal electrode stack on the device layer. (F) Photolithography using a thick photoresist defines the device's channel structures. (G) A short HF etch of the oxide undercuts the silicon device layer to create anchor points for subsequent parylene processing. (H) A conformal parylene deposition encapsulates the photoresist and resonating structure. (I) A layer of aluminum is deposited over the structure as an etch mask. (J) An ICP-RIE etch through the parylene reveals the underlying oxide layer. (K) A HF wet etch fully undercuts and releases the structure to produce the freestanding resonator, and (L) the channel is released in acetone. (M) A shadow mask process deposits electrodes on the substrate. (N) Epoxy seals the undercut edges, and (O) a final parylene deposition electrically isolates the channel from the substrate.

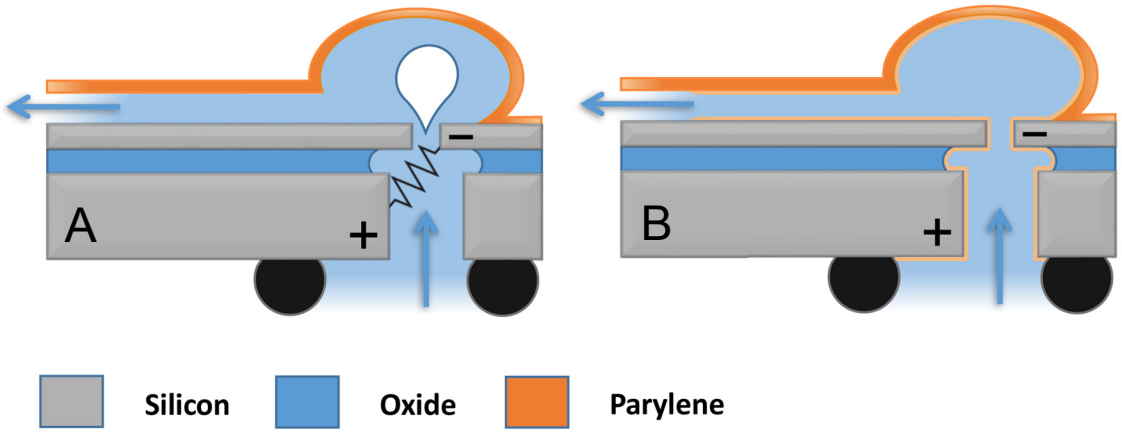

Figure 4.9. (A) Electrolysis occurs as a result of conduction through the fluid layer. (B) A second parylene deposition isolates the two silicon layers.

To isolate the fluid from silicon, a second parylene process coated the walls of the port and the channel with an isolating layer. This second deposition also formed a fully enclosed channel layer by sealing the edge where the primary parylene layer meets the silicon anchors. Figure 4.9(B) illustrates the functionality of an inner parylene layer. As with the first parylene deposition, the opposing side of the wafer had to be protected during deposition to avoid coating the electrodes on the frontside or adding additional parylene to the structure, both to minimize structural weight and to avoid closing the gap between the silicon bridge and the substrate.

Section 4.4: Vertical Flow Limitations

The final porting scheme certainly forged a robust fluidic interface utilizing the wafer's backside; however, this did not come without limitations. The primary challenge when driving fluid vertically spurs from sample settling and collection that is mediated by gravity. As is well-known, the force on an object due to gravity is determined simply:

$$F_G = m \cdot g \tag{4.1}$$

where m is the sample mass and g is the acceleration due to gravity. In a vertical port, the pull of gravity competes with the dynamics within the fluid, namely the drag force that arises when the sample moves relative to the fluid (shown in Figure 4.10). This drag force takes the following form for a circular object, where μ is the fluid viscosity, v is fluid velocity, and a is the particle radius [104]:

$$F_D \propto 6\pi \cdot \mu \cdot v \cdot a \tag{4.2}$$

To ensure sufficient lift to convey the sample into the device, the drag force must overcome opposition from gravity ($F_D > F_G$). This requires a minimum flow to attain sufficient drag, which poses a challenge for sample control inside of the microfluidic device. The vertical port has characteristic linear dimensions on the order of hundreds of micrometers, with progressive tapering down to the highly constricted fluidic channel in the resonator. Mass flow is conserved everywhere within the microfluidic volume for steady flow, meaning that mass transport does not change even for a changing channel diameter. For incompressible fluids where the density does not appreciably vary, fluid flow in various diameter cross-sections are equalized by fluid velocity according to [105]:

$$v_1 \cdot A_1 = v_2 \cdot A_2 = constant \tag{4.3}$$

where A is the cross-sectional area. This continuity relation means that there is almost a 10^3-order increase in the flow of the fluidic channel compared to the interfacing port, and this velocity gradient is shown in Figure 4.11 very clearly.

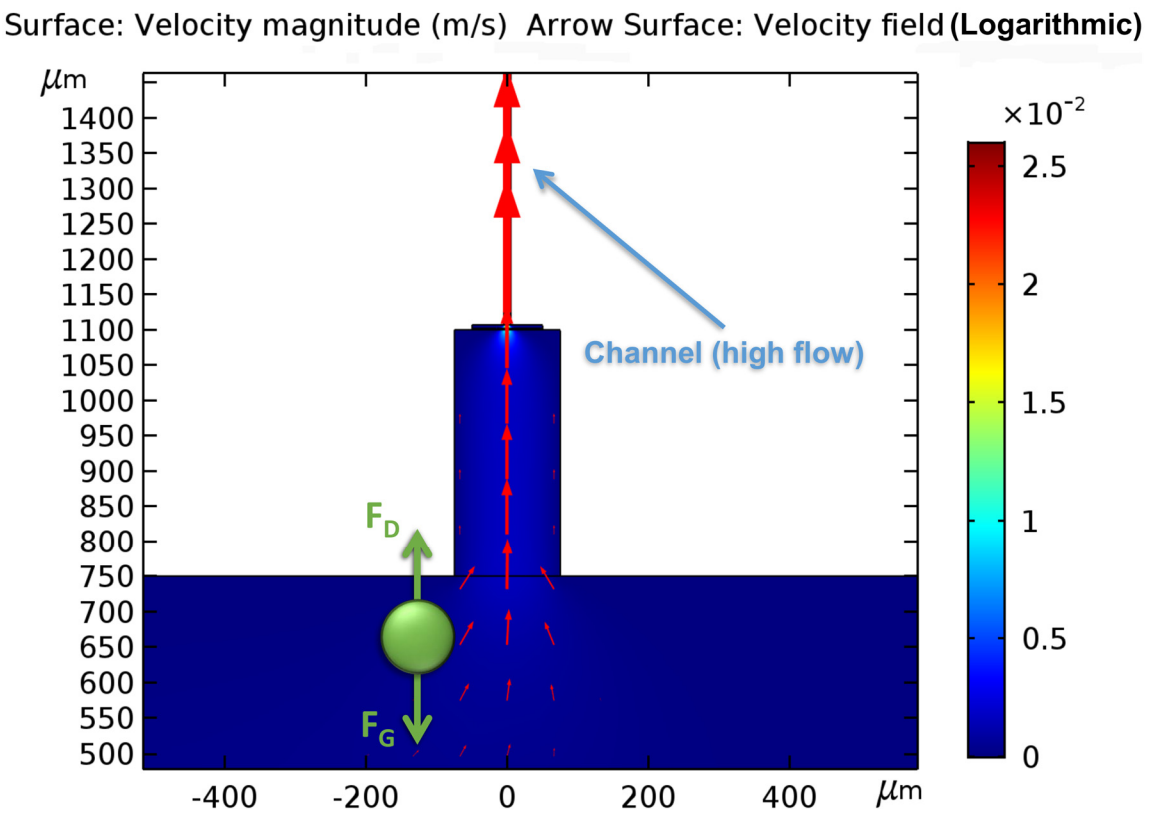

Figure 4.10. Vertical port orientation necessitates a minimum flow to lift the sample to the port surface. Such flow creates a high velocity in the constricted channel structure.

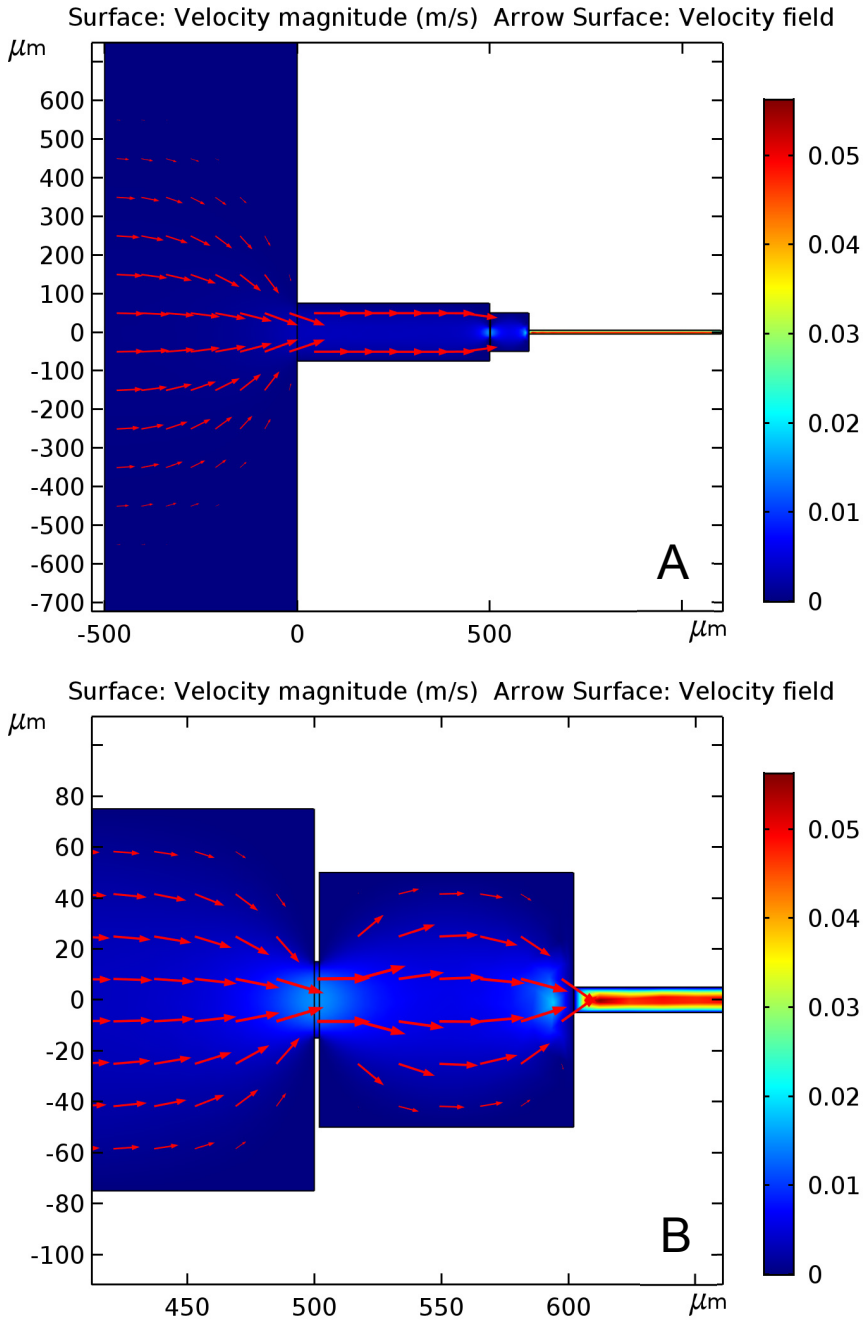

Figure 4.11. A two-dimensionally projected fluidic simulation: (A) for the complete interfacing geometry for the devices and connections; (B) for the internal device geometry.

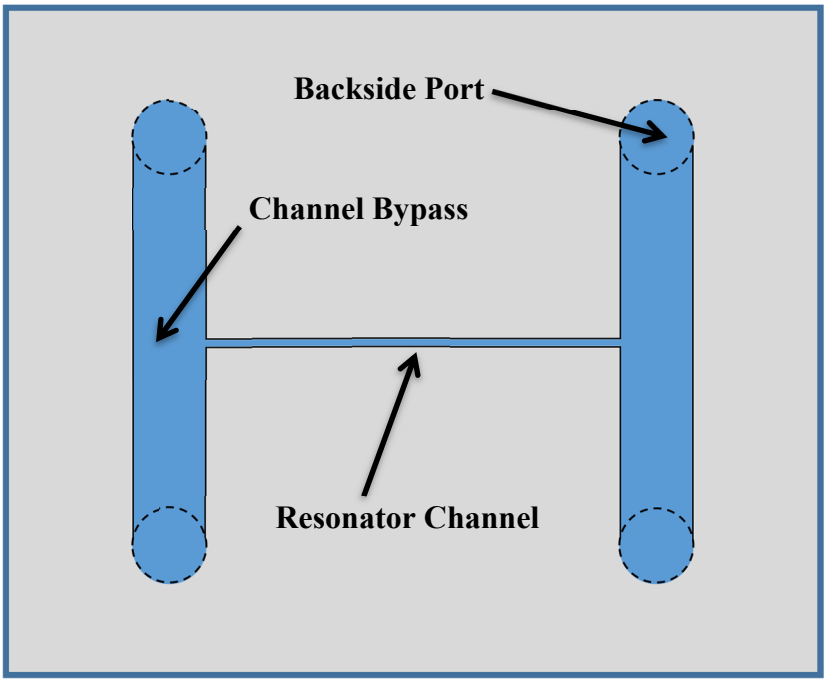

Figure 4.12. Proposed port configuration showing four backside ports for fluidic channel bypass on-chip to achieve better control of sample flow in the resonator channel.

In context of the fabricated devices, lifting samples into the device generally requires transporting them through the resonator at a high, non-ideal velocity. There does exist a method to address this challenge, however. The drag force is also affected by the viscosity of the fluid: as a more viscous fluid can create additional drag, and the density of the fluid can mediate sample buoyancy. With cell culture media, glycerol can provide the necessary boost in viscosity and density, with the tradeoff of measuring the cell in a fluid that does not necessarily reach equilibrium with its constituent fluid, necessitating additional parameters for mass measurement.

While optimizing fluid parameters can help alleviate lift issues, a better alternative involves opening a larger fluidic channel on the chip's topside. Of course, the resonator channel must only be enlarged to accommodate increasing cell size in the name of

sensitivity, but introducing a four-port network on the device can create the necessary bypass (depicted by Figure 4.12). With this bypass occurring on chip, rather than inside the platform of the vacuum chamber, a larger volume of fluid can reach the chip surface thereby ensuring a less severe velocity differential and passing all cells through the chip fluidics. The utilized parylene approach can readily accommodate this fluidic network, and in this way, more precise fluidic control can be achieved.

Section 4.5: Parylene Alternatives

Since parylene can pose notable processing challenges and increased fabrication complexity, we also considered an alternative. One promising candidate was channel formation with a Nanoscribe lithography system [106]. This three-dimensional printer utilizes two-photon polymerization to expose proprietary photoresists (similar to SU-8) to create computer-directed volumetric patterns. With this technology, we attempted creation of arbitrary channels as a replacement to the more involved method of parylene channel formation. One useful benefit was that this approach could incorporate varied designs in any dimension within the microfluidic channel itself, including constrictions or various structures to mechanically probe cells, potentially to aid in the investigation of stiffness [107]. Figure 4.13 shows a compilation of microscope images with varying magnification of the resulting channel structures. Due to the field of view, or write field, the system must stitch together designs through stage movements, which have an associated tolerance error and various re-exposure considerations. This stitching can create either non-continuous channels or small non-contiguous voids, as seen in the figure. With considerable work, it is possible to overcome this stitching concern over the length of the entire channel (~10 mm), and three-dimensional lithography printing could be a viable option for adding functionality to the channel or simplifying the fabrication process.

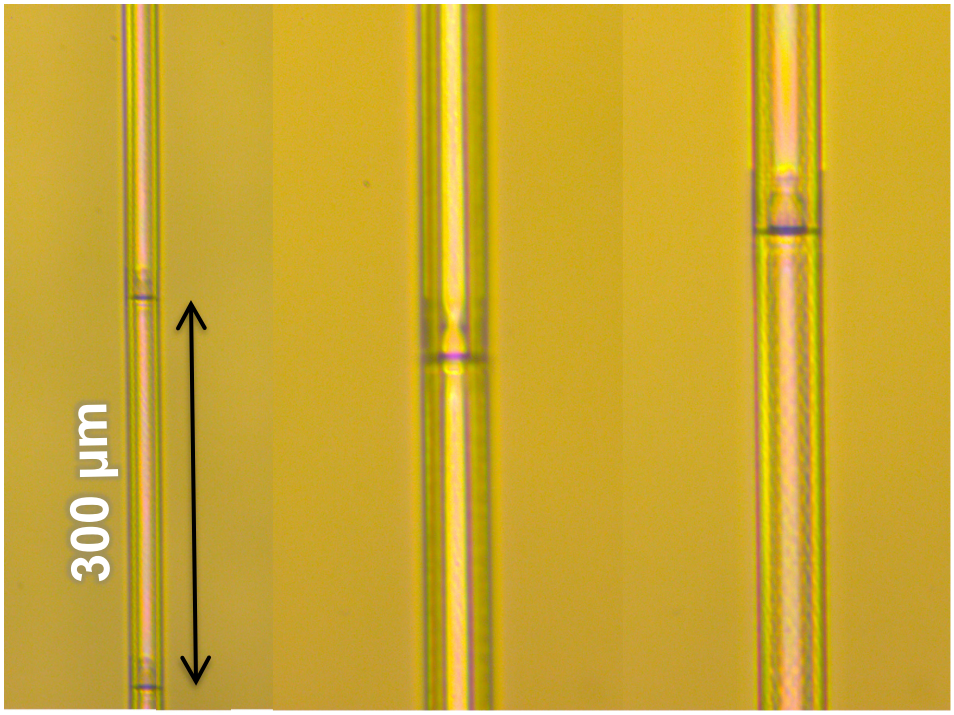

Figure 4.13. This compilation of microscopes images shows three-dimensionally printed channel structures under various magnifications, with a scale bar associated with the far-left magnification. The inner channels are 15 µm wide, with a total width of 25 µm.

Chapter 5

Measurement

This next section discusses measurements and validations performed with the devices from the previous chapter using a system employing all sub-components discussed in Chapter 3: optical trapping/detection, acquisition/feedback, microfluidics, vacuum mounting, and data acquisition.

Laser trapping and optical accessibility are first described in demonstration of the channel's viability for optical integration, together with photonic-crystal enhancement, which is a confirming result of this work. In order to utilize these devices for actual mass measurement and laser trapping, calibration and characterization were critical to understanding performance and optimizing system parameters. Finally, fluid density and particle experiments readied the system for measurement with cells in fluid.

Section 5.1: Optical Validation

Since optical trapping promises position control for improved measurement precision and extended device functionality, investigations first validated the applicability of the etched PhC pattern's enhancement for single cells. The etched PhC was coated with parylene for planarization and to better simulate conditions inside of the channel, with field-size corresponding to designed channel dimensions. Figure 5.1 shows yeast cells in

suspension on the PhC, where the figure presents three snapshots of a yeast cell being trapped on the PhC and dragged as the laser moves along the pattern, shown clearly by fixed reference clusters. The cell was trapped with a low optical intensity of 6.7 $\mu W/\mu m^2$ when moving the cell at 0.5 μm/s. Since the drag force of the fluid is proportional to the velocity of the cell, the speed at which it can move is limited by the stiffness of the trap.

The ultimate manipulation speed is also affected by kinetic friction that occurs as the cell and the substrate move relative to each other. In this context, the low surface adhesion of parylene is actually beneficial for cell manipulation, and can be engineered over a range of hydrophilicities and nanoscale-roughness levels through oxygen plasma surface treatment [108], specifically for controlling cell adherence or non-adherence.

Given sufficient settling time or fluid evaporation, sample particles reach a sufficient proximity to the surface such that short-range attractive forces, known as the van der Waals forces, render the particles adherent to the surface [109] dictated by surface area or resultant deformation. Dependent upon the compatibility of the surface, cells add a dynamic complexity, since adherent cells can spread, migrate, and otherwise control their interaction with the surface [110]. Therefore, operation in a fluidic environment that is mediated by careful control of the flow and fluid drag force can greatly assist optical trapping in addressing surface adherence and attraction. This functionality is readily provided by a channel structure and adequate control of the pressure differential.

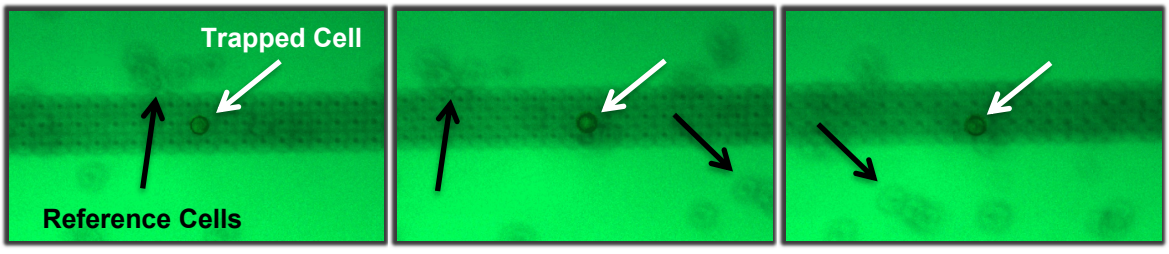

Figure 5.1. Snapshots (from left to right) of a cell trapped on the PhC pattern and moved (in reference to other cells) by the trapping laser [111].

Accordingly, the next validation phase employed optical trapping within a confined fluid volume to confirm the compatibility of the parylene channel and to verify the material's optical characteristics, as represented by Figure 5.2. The figure shows good optical clarity within the channel, assisted by both the properties of the parylene and the geometry of the channel's apex. The optical path as it transitions from vacuum to parylene to water is governed by Snell's law [112], which becomes especially important if the channel assumes a large degree of curvature. A flattened profile was a goal for the fabrication process.

Figure 5.2 depicts a progression of video fames showing the optical manipulation of a 1-µm polystyrene bead suspended in fluid as it is moved along the channel length (relative to a stationary, reference particle). The trapping laser is blocked by an optical filter to maintain particle visibility. This capacity to manipulate the particle within the channel and fix its position even in the presence of fluid pressure and flow, is a key functionality of the MEMS device towards position control and better measurement precision.

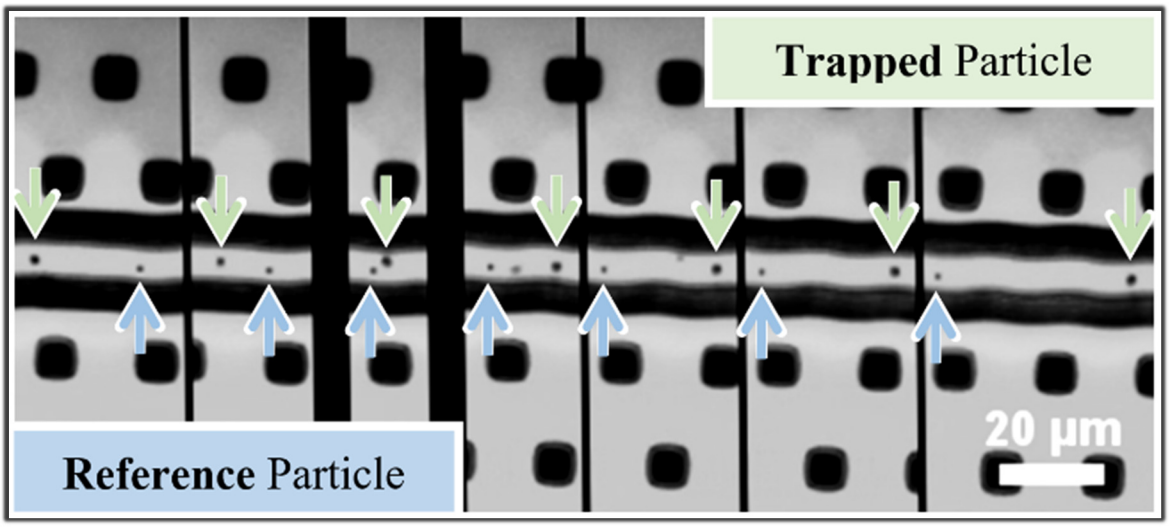

Figure 5.2. Progression frames of a polystyrene bead optically trapped and manipulated within the parylene-fluidic channel (from left to right), demonstrating a critical capability of these devices [62].

To demonstrate compatibility with microscopy and enabled fluorescent imaging, cadmium selenide (CdSe) quantum dots were loaded into the channel. The quantum dots fluoresce in the red wavelength band (~615 nm), which is clearly observed in Figure 5.3(A). The blue features spur from diffraction of the stimulation wavelength under dark-field, revealing the channel structure and port. Figure 5.3(B) shows the clarity with which samples can be viewed within the beam-channel device.

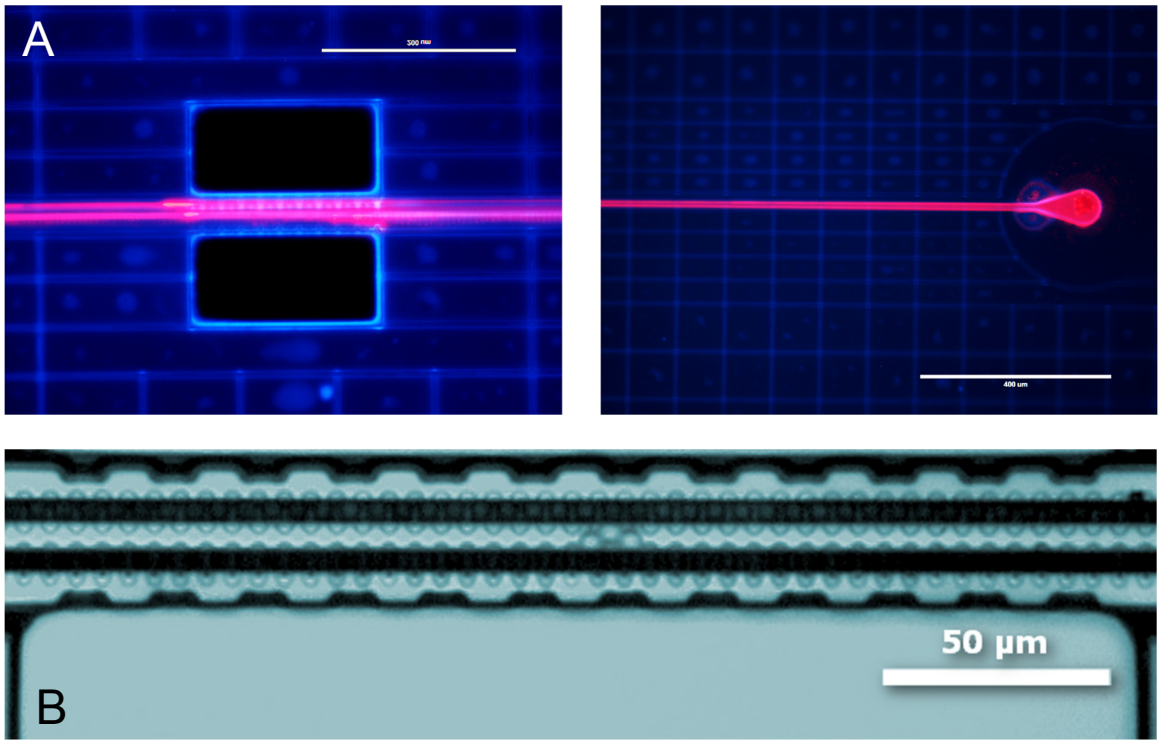

Figure 5.3. (A) Fluorescent micrographs of CdSe quantum dots exhibiting fluorescence with the fluidic channel, depicted in red. The blue excitation light is diffracted by device features and captured in the dark-field image. Both the bridge-resonator and channel port are depicted. (B) Micrograph of the bridge resonator accompanied by three 5.5 µm polymer spheres centered on the structure.

Section 5.2: Device Performance

As discussed extensively in Chapter 2, resonant frequency and quality factor underpin the capability of the fabricated devices. To characterize frequency response, the resonance was first determined in an open-loop drive configuration with a fixed actuation amplitude, bias voltage, and swept frequency parameter. Depending on structural topology and resultant fabrication tolerances, the frequency for the final devices varied around 250 kHz. The devices generally operate with a DC bias of ~40 V and an AC actuation voltage of ~6 V_{pp}. The raw data is fitted by a model for damped harmonic oscillation to provide more accurate parameter estimation (as discussed in Section 2.5: Structural Damping and Resolution). In this manner, Figure 5.7 shows the typical response for one of the beam-resonator devices, indicating a resonant frequency around 286 kHz with a quality factor of ~76.

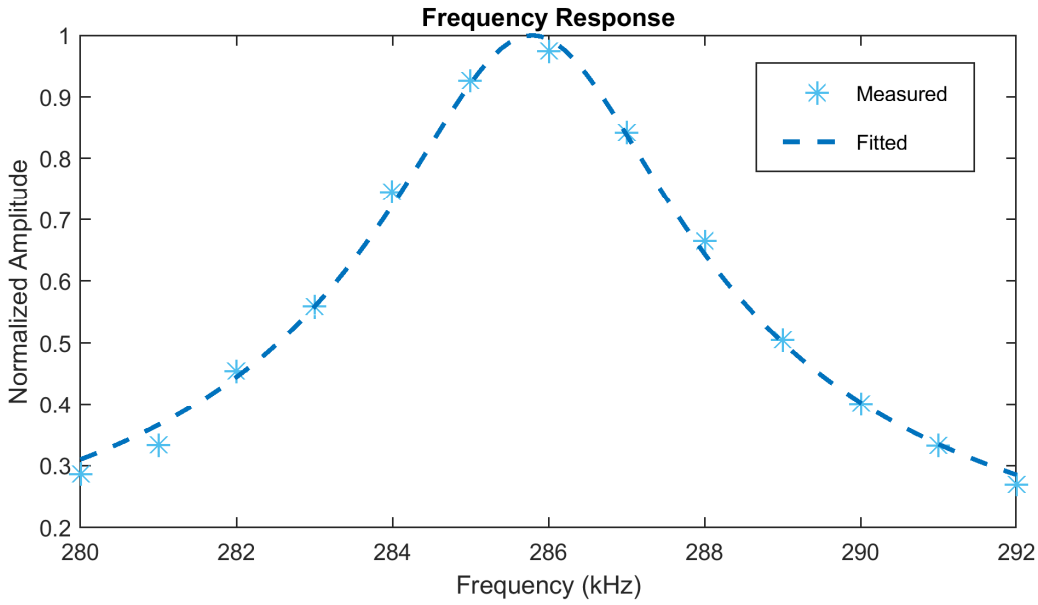

Figure 5.4. Typical resonant frequency response of the beam-channel structure showing a resonance around 286 kHz with a quality factor of ~76.

Figure 5.5 shows an important challenge in maintaining accurate and stable experimental conditions. In the figure are multiple frequency sweeps for the same device sequential in time, over the course of ~10 minutes. Due to mechanical settling in the microscope stage, the signal amplitude decreases temporally, which poses certain difficulties in conducting sequential experiments. Above all, stable measurement originates from the high-signal-to-noise ratio criterion. With careful stabilization and fixation, this drift can be improved, but the current setup requires constant operator intervention. One major instigator for this behavior is the introduction of many peripheral connections that mate with the vacuum chamber. Each brings with it additional stress and torque that translates to stage slip. To further improve experimental fidelity, the set-up could employ a more rigidly mounted stage, immune to such drift, or a computer-controllable motorized stage with the necessary feedback to maintain signal level.

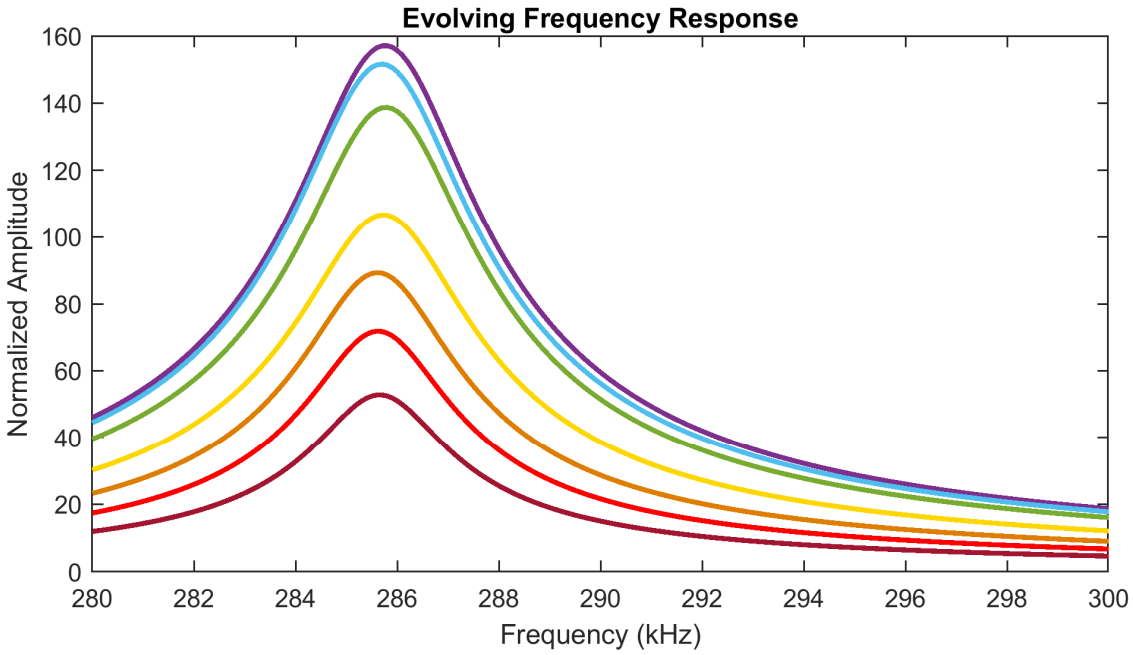

Figure 5.5. Frequency response of the beam structure (filled with water) under vacuum. Due to non-ideal drift in the microscope stage, the signal amplitude varies with time.

By virtue of the imposing nature of air-structure interactions, the Q-factor of the devices were quite low when operated at atmospheric pressure (Q < 10), predominantly indicating squeeze-film and viscous air damping and their severe energy dissipation. To mitigate such opposition, ensuing experiments used the custom mountable vacuum chamber described in Chapter 3 (Section 3.2: Vacuum Chamber Design), which was capable of achieving vacuum levels less than 100 mTorr. This reduction in pressure attained at least an order of magnitude increase to nearly Q ~ 100 for better performing devices. Slight fabrication variation can have a profound effect on the devices, even those developed on the same wafer. Across all devices, the mechanical Q varied on the range from 60 ~ 100. Resonance quality in progressively diminishing vacuum levels is presented by Figure 5.6.

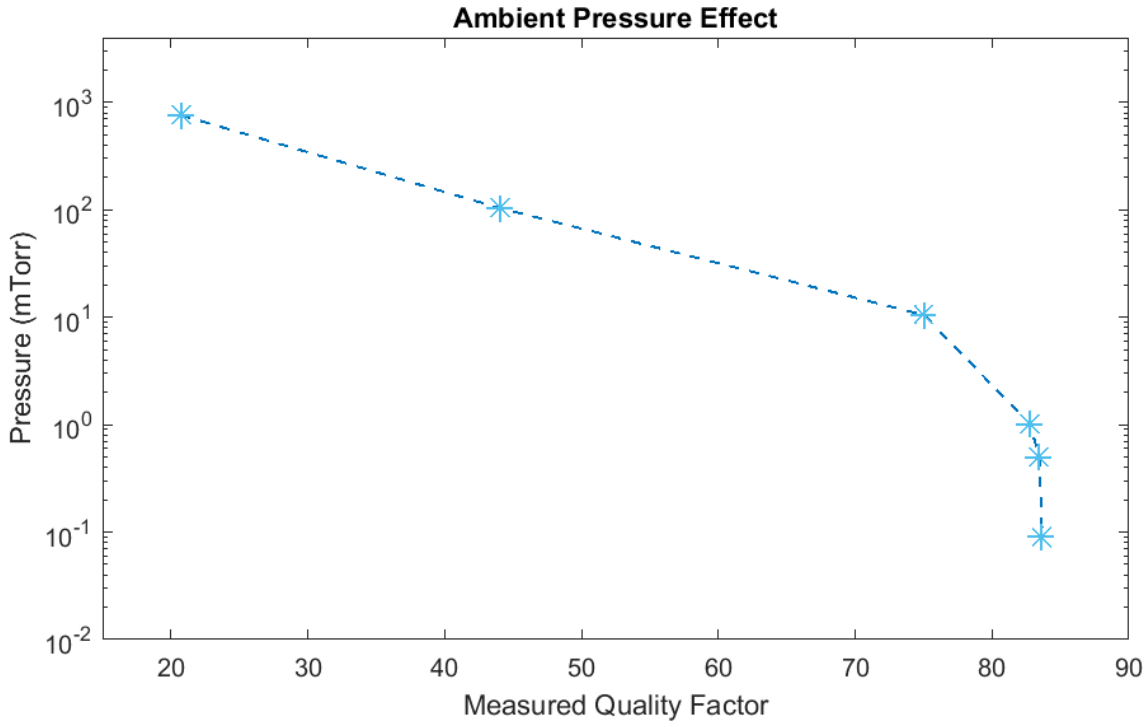

Figure 5.6. The quality factor for the same resonator operated under various ambient pressures, approaching achieved improvement asymptotically.

Since the quality factor asymptotically approaches 10^2, we can likely conclude that air damping no longer dominates the equation; rather, the Q sees limitation from intrinsic effects, especially those arising from friction between the silicon and parylene surfaces. This dissipates energy in the form of heat as the structure undergoes periodic deformation. Designs sought to minimize the surface contact between these two materials, but channel-structure formation retains a majority stake in their union.

The next performance metric sought to verify that fluid loading does not prompt additional damping from fluid dynamics within the structure. To this end, the channel was loaded with air, isopropanol, and water, and the resultant behavior observed. Figure 5.7 plots the three responses normalized by both resonant frequency and amplitude. Fluid loading with similar densities and viscosities did not adversely affect the quality factor.

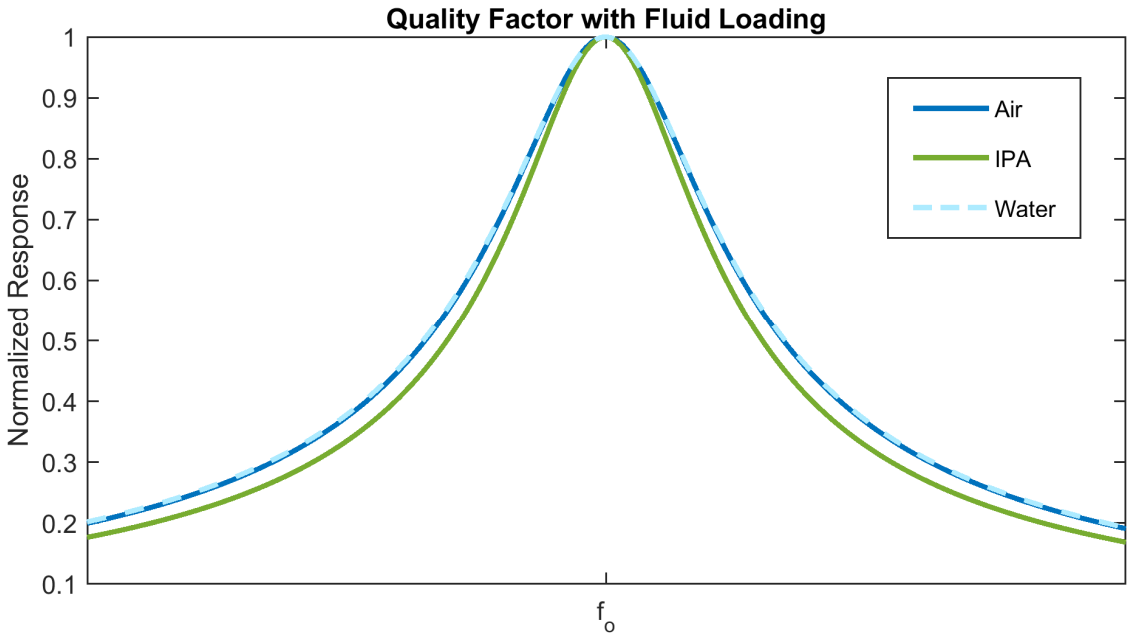

Figure 5.7. Resonant response for three loading fluids: air, isopropanol, and water. Their resonant frequencies have been normalized for comparison of quality factor, which does not appreciably change.

However, viscosity does play a role in device performance. IPA has a viscosity that is more than double that of water [113]. The low viscosities of water and air shared a similar quality factor, but Figure 5.7 shows a slight improvement in the quality factor for IPA. This phenomenon has been observed for other embedded fluidic resonators exhibiting regions of increasing and decreasing quality factors, depending on fluid viscosity [114]. As the channel resonates and undergoes compression and extension, turbulence inside the fluid can create flow into and out of the structure leading to energy dissipation and degradation of Q. This process spurs from complex interactions within the fluid governed by viscosity, density, and pressure.

Section 5.3: Characterization of External Effects

There are many external disturbances that exist for the MEMS resonator and its supporting system. Key sources include the bias voltage, internal channel pressure, ambient pressure, and temperature, among others. The ultimate observed frequency shift, and hence perceived sample mass, is the output of a symphony of contributing sources. Thus, it is essential that the devices undergo careful characterization, to understand how these sources affect frequency and how they can be reduced or isolated.

Section 5.3.1: Bias Voltage

Bias voltage has a measurable effect on resonant frequency due to structural bending and spatially varying capacitance. The analysis in Section 3.1.4: Electrostatic Actuation makes a simplifying assumption for parallel actuation; however, the physical device undergoes bending induced by biasing and stress within the structure. This leads to non-uniform spacing between the structure and the underlying substrate, producing a capacitance and electrostatic-force gradient. Such a gradient incites a reduction in stiffness

and a resonant frequency shift that is linearly related to the square of the voltage [115]. This perturbation was observed in the beam-channel devices as characterized by Figure 5.8. For the dually clamped beam, the gap spacing can be modeled by Equations (5.2).

$$g(x) = d - v(x) \tag{5.1}$$

$$g(x) = d - C_1 \sinh(a \cdot x) - C_2 \cosh(a \cdot x) - C_3 \sin(a \cdot x) - C_4 \cos(a \cdot x) \tag{5.2}$$

And the force for the spatially varying capacitance can be defined:

$$\mathrm{F} = \frac{\varepsilon V^2}{2} \cdot \frac{d}{dg}\left(\int_0^L \frac{w}{g(x)}\,dx\right) \tag{5.3}$$

The definition of stiffness describes the force gradient in the presence of a spatially varying electric field and capacitance; thus, the electrostatic stiffness takes the form shown in Equation (5.4).

$$\mathrm{k}_e = \frac{dF}{dg} = \frac{\varepsilon V^2}{2} \cdot \frac{d^2}{dg^2}\left(\int_0^L \frac{w}{g(x)}\,dx\right) \tag{5.4}$$

With the electrostatic contribution in hand, effective stiffness derives from the sum of mechanical (k) and electrical stiffnesses [116]:

$$k_{eff} = k - k_e \tag{5.5}$$

By differentiating the resonant frequency relation with respect to stiffness, one can find that it has the following dependency for small variations in stiffness:

$$\frac{d\mathrm{f}_r}{\mathrm{f}_r} = -\frac{1}{2} \cdot \frac{k_e}{k} \tag{5.6}$$

Hence, biasing has a measurable effect on resonant frequency and must be considered in device characterization.

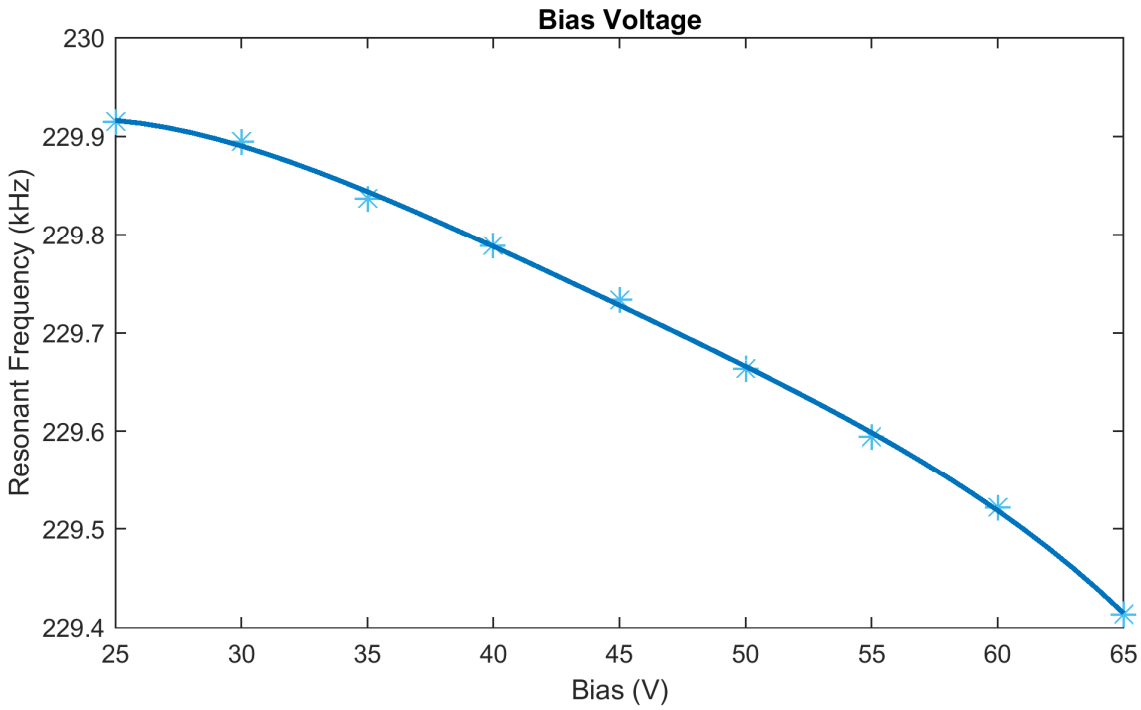

Figure 5.8. Measured frequency variation due to fluctuations in bias voltage. Increasing structure bias reduces the resonant frequency.

Section 5.3.2: Fluid and Ambient Pressure

Fluid/air pressure inside and outside of the channel also have a significant effect, shown by Figure 5.9 and Figure 5.10. For ambient air surrounding the structure, interactions with air molecules, and the persistent collisions, lead to an effective increase in structure mass. This effective mass reduces device sensitivity and its associated resonant frequency; and the ambient fluid's effect is determined by density [117]. Figure 5.9 clearly

shows an increasing trend in resonant frequency in response to decreasing pressure and structure-air interaction.

Due to the integrated nature of the fluidic channel, dynamic pressure and fluid properties within the channel also lead to resonant frequency shifting. Figure 5.10 presents a linear trend between resonant frequency measurements and internal fluidic pressure. For simple beams with varying boundary conditions, the structure's stiffness parameter is proportional to the area moment of inertia (I) and the material Young's modulus (E) [118]:

$$k \propto \mathrm{E} \cdot \mathrm{I} \tag{5.7}$$

where the area moment for a rectangular cross-section referenced to the neutral plane is given by:

$$I = \frac{wh^3}{12} \tag{5.8}$$

Increasing pressure within the channel prompts two competing factors: higher pressures mandate increased fluid density and added mass on the structure, and the pressure simultaneously leads to bulging of the channel walls, especially along the vertical axis. In this way, channel expansion has a third-order effect on the stiffness of the structure, which dominates and results in an upward trend in resonant frequency.

Section 5.3.3: Structure Temperature

Another essential factor is temperature dependence of the structure's response and its constituent materials. This consideration becomes especially consequential when integrating optical trapping, since the structure is locally heated by the trapping laser. To better understand its effects and apply these findings more broadly to temperature drift, the structure's resonant frequency was simulated through acknowledgement of temperature-

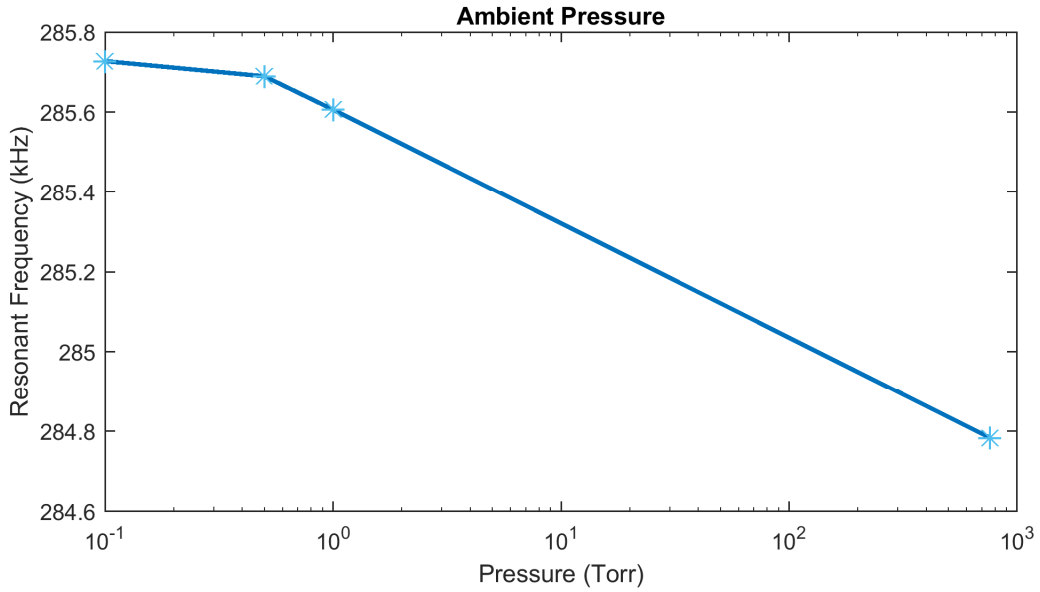

Figure 5.9. Measured variation due to fluctuation in pressure surrounding the structure, leading to a decrease in resonant frequency.

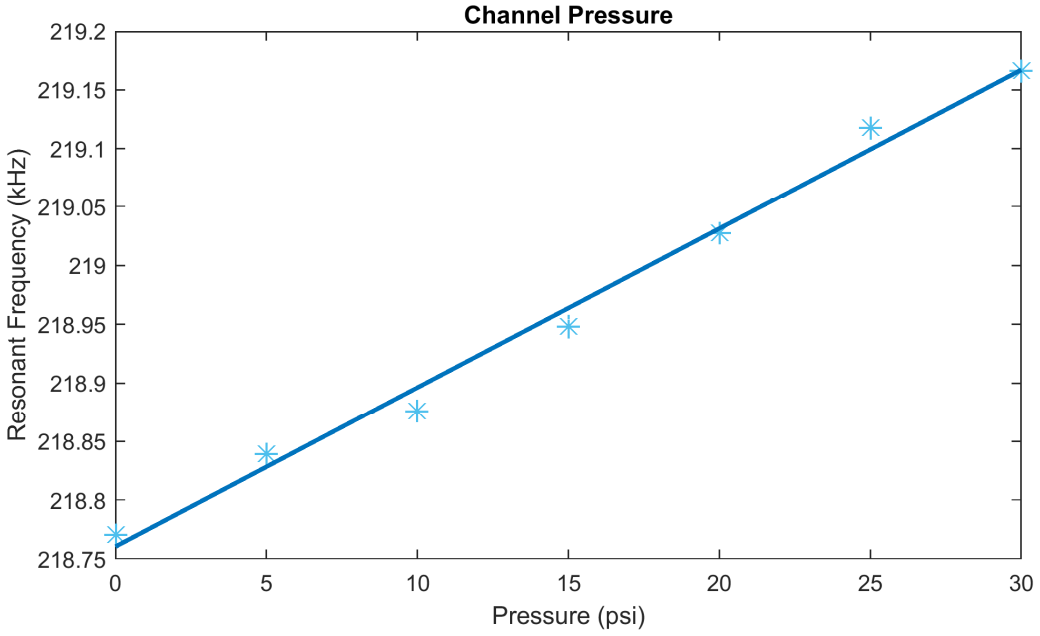

Figure 5.10. Measured frequency variation due to fluctuation in channel pressure. Increasing pressure increases the resonant frequency.

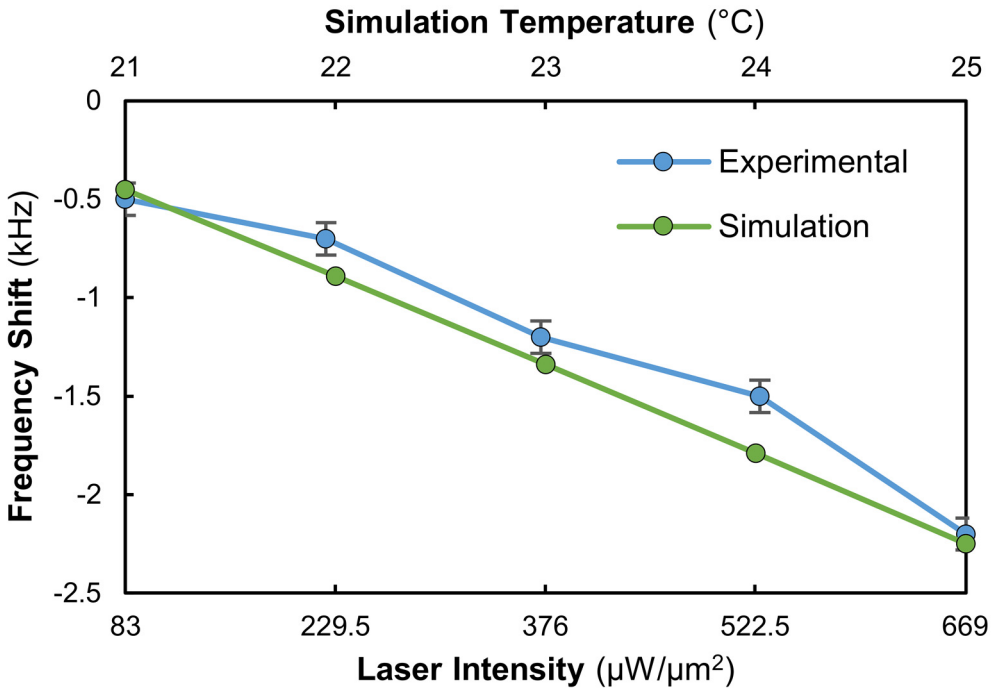

Figure 5.11. Resonant frequency shift induced by the trapping laser, accompanied by a simulation with elastic temperature dependence, necessitating a calibration factor and consideration during continuous-trapping measurements [119].

material relationships, shown in Figure 5.11. This dependence manifests itself as a change in material elasticity (Young's modulus), having an empirically derived temperature dependence [120] [121]. Due to the dynamic E(T), structural heating can induce a subsequent resonant frequency shift, also shown in the measurement result of Figure 5.11. The Young's modulus variation for silicon has been evaluated by vibrational methods, shown to track the expression [120] [121]:

$$E = 1.20 \times 10^5 \cdot e^{\frac{2.61meV}{k_B T}} \quad [MPa] \tag{5.9}$$

For parylene, when considering small temperature variations below the glass transition temperature, E has an approximately linear relationship with a modest rate of

change. In the glass transition region, between 35 ~ 60°C, parylene demonstrates a marked, non-linear change in elasticity [122]. Therefore, attention to temperature and its control become very important for frequency stability. Over low temperatures, both materials exhibit linearity, and such a trend is revealed by the structure's overall frequency response. Figure 5.11 provides a resonant frequency calibration for various optical trapping intensities, matched to simulated temperature variations within the channel-beam structure.

Section 5.4: Device Calibration

To achieve both relative and absolute mass measurements, the structure required calibration with known mass. This mass can come in two forms: liquids of known density and parameters, or standardized particles with controlled size and composition. The following sections will consider both methods to evaluate the devices.

Section 5.4.1: Fluid Mass Calibration

The first and most straightforward mass calibration method involves channel loading with fluids of differing densities. Figure 5.12 shows the structure's frequency response when interrogated with three fluids: air, isopropanol, and water. Water was confirmed as the heaviest and densest of the three.

Furthermore, fluid loading of the device provides a method to calibrate its positional sensitivity. By filling the structure to an arbitrary position x_s and with an assumption about the sensitivity profile for the structure that is derived from its modal shape (obtained either analytically or through simulation), one can measure the sensitivity at particular positions with the sample fluid. By employing a symmetry argument, we can consider only half of the total length L of the resonator. From simulation and the mode structure of a bridge, the profile can be fitted by a multiple-degree polynomial. In this case,

a third-degree polynomial achieves an R-squared value of 1.00, and is well representative of its performance. Accordingly, the sensitivity at any arbitrary position can be represented as:

$$S(x) = y_3x^3 + y_2x^2 + y_1x + y_0 \quad \left[Hz \cdot {}^{ng}/_{pg}\right] \tag{5.10}$$

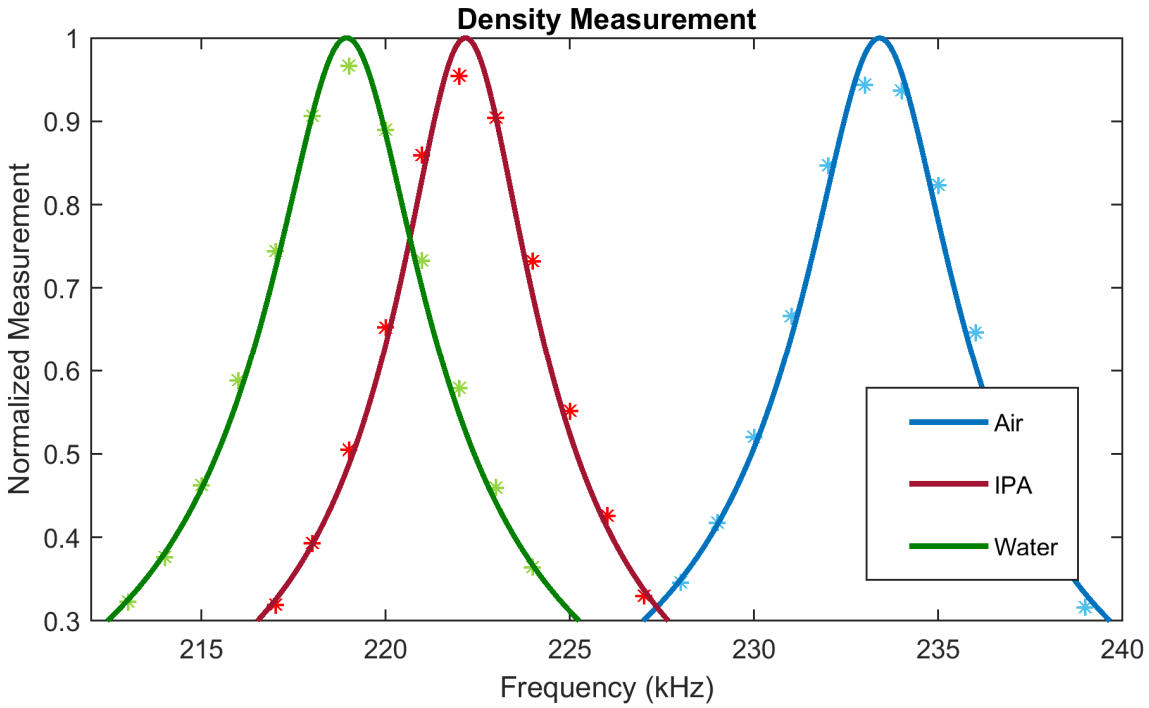

Figure 5.12. Frequency response to fluid loading with air, isopropanol, and water. Water was confirmed as heaviest of the three.

If we integrate the sensitivity over the length of the structure, multiplied by the sample density, the inverse of the structure mass, and channel cross-sectional parameters, we can arrive at the expected frequency shift as shown in Equation (5.11).

$$\frac{h \cdot w \cdot d_s}{m_o} \int_0^{x_s} S(x)\ dx = \Delta f \quad [Hz] \tag{5.11}$$

If we measure Δf, we can solve the equation above (with an appropriate representation of the sensitivity) to determine its vertical-intercept and the overall scaling for the measured structure's sensitivity at a point x_s, shown by Equation (5.12).

$$S(x_s) = y_3\left({x_s}^3 - \frac{{x_s}^4}{4}\right) + y_2\left({x_s}^2 - \frac{{x_s}^3}{3}\right) + y_1\left(x_s - \frac{{x_s}^2}{2}\right) + \frac{1}{x_s} \cdot \frac{m_o}{h \cdot w \cdot d_s} \cdot \Delta f_s \tag{5.12}$$

By filling the structure completely and taking $\Delta f_s = \Delta f \,/\, 2$ to reduce the calculation symmetrically, Equation (5.12) offers a calibration for the sensitivity.

Section 5.4.2: Particle Mass Calibration

Since the goal of this work is to seek mass measurement for a discrete cell on the structure, instead of fluid mass distributed along the beam, the next calibration employed single particles. To characterize the resonator's sensitivity and response to particle mass loading, three 5.5-µm polymer beads (each with a density of 1.05 g/cm^3) were driven to the beam-center using the manipulation laser; Figure 5.13 shows one particle centered on the beam structure as an example.

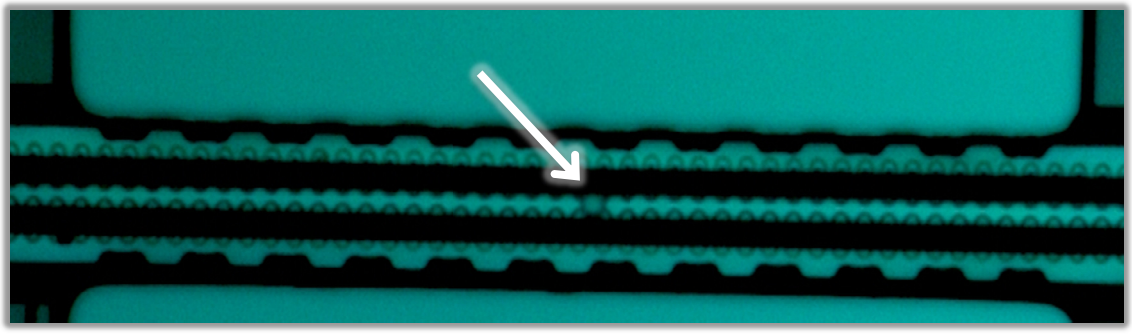

Figure 5.13. An image of the bridge resonator indicating the position of a 5.5 µm polymer sphere centered on the structure.

Figure 5.14 observes the resonant frequency of an empty channel (fitted by the equation for a damped harmonic oscillator) accompanied by a frequency shift from particle loading (accumulating a mass of ~274 pg); when compared to simulated values, the plot shows good agreement, where the measured sensitivity (normalized to structural mass) was 165 Hz · ng/pg while simulation predicted a sensitivity of 161 Hz · ng/pg.

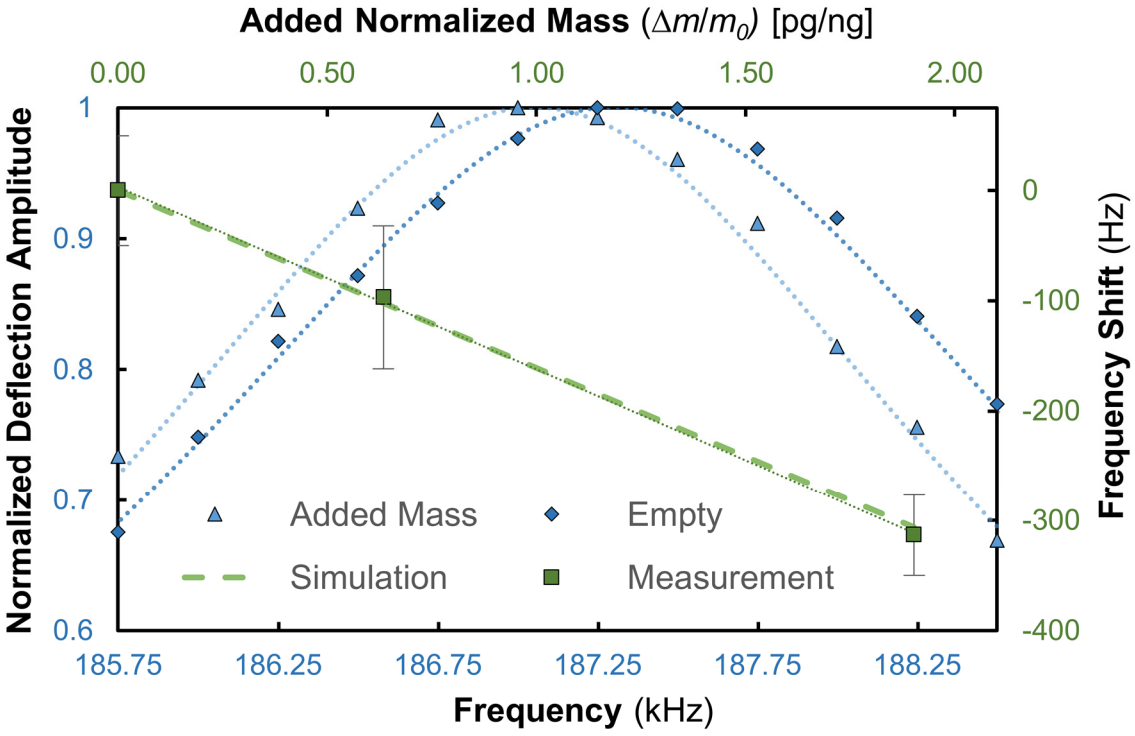

Figure 5.14. Measured frequency response of an empty and a mass-loaded channel fitted by the equation for damped harmonic oscillation, accompanied by measured and simulated frequency shifts incurred from added particle mass. Experimental and simulated frequency shifts agree very closely [119].

Section 5.4.3: Positional Calibration

The center of the bridge boasts the highest sensitivity; in order to consider sensitivity at other positions, mass loading at various positions were considered. Figure 5.15 verifies the sensitivity position-dependence through measurement and simulation at its two boundary points (anchor and beam-center) and at the midpoint between them. It may appear counterintuitive to observe any mass sensitivity at all on the end of the beam (assuming that it remains ideally fixed); however, this arises from undercutting of the oxide layer at the anchor during fabrication that permitted undesirable movement.

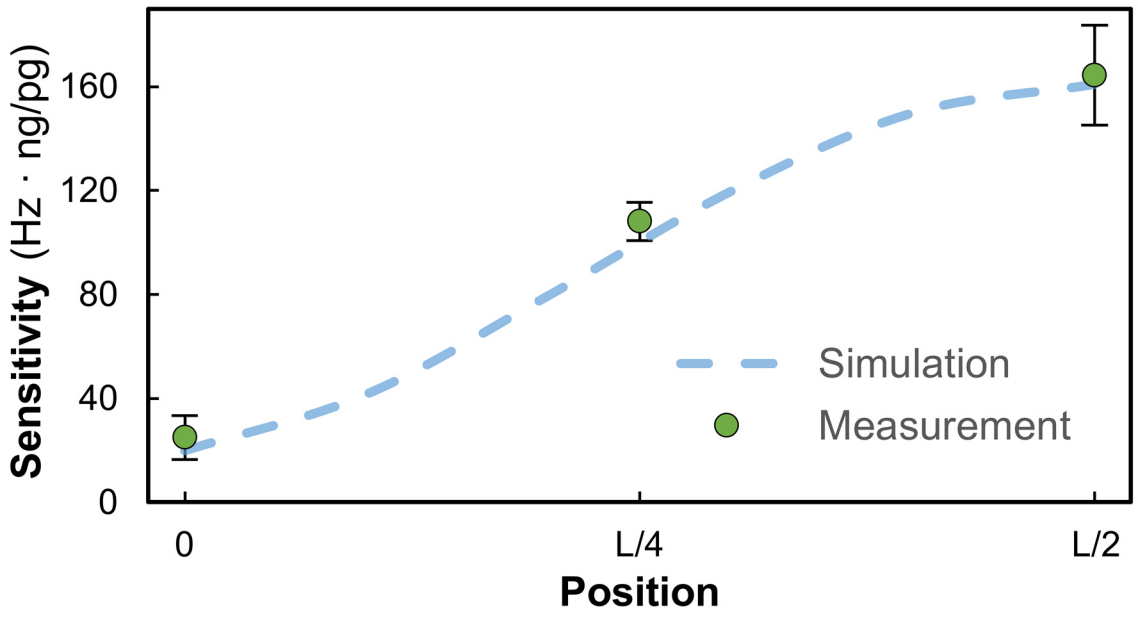

Figure 5.15. Device sensitivity versus mass position for two measured boundary cases and their midpoint with comparison to simulation. Both measurement and simulation validate the response variance due to sample position [119].

This figure gives clear evidence that position has a significant effect on the perceived mass of the sample, and optical trapping is therefore warranted for sample position control and measurement accuracy. To this end, the structures described in this work provide necessary access and observation for optical trapping that can allow precision and motion suppression.

The measured sensitivity parameter for the device is essential to obtain an absolute or relative mass measurement from observation of the resonant frequency. Therefore, it is critical to perform calibration through multiple experiments and methods. Table 5.1 compares the results using both particle and fluid calibration approaches. Each result is referred to its maximum sensitivity at the center of the beam, and the calibration factors show good agreement, even across differing methods.

Table 5.1. Measured Beam-Center Sensitivities

Centered Particle ($Hz \cdot {}^{ng}/_{pg}$)	164
Isopropanol ($Hz \cdot {}^{ng}/_{pg}$)	169
Water ($Hz \cdot {}^{ng}/_{pg}$)	170

Section 5.5: Cell Measurement

The preceding calibration and performance characterization prepared the system and device for actual cell experiment to demonstrate its capabilities for suspended measurement. To this end, yeast cells were measured with the devices due to their resiliency and simpler culture protocol. For the experiment, a standard baker's yeast strain (BY4741) was cultured on a solid agar plate at 30°C for 2 days to form large ~1 mm colonies, and the cultured cells were then stored at 4°C. To prepare the cells for

measurement, they were suspended and grown in a few milliliters of yeast extract peptone dextrose (YEPD).

The suspended-cell samples were injected into the device using the microfluidic pathways described in Chapter 3, and the resonant frequency was monitored as they passed through the device channel. Figure 5.16 shows the resulting frequency measurements over the duration of the experiment. The light blue region of the plot indicates the level of frequency jitter that was present, on the level of a few Hertz. Secondly, the measurement exhibits some drift owed primarily to pressure fluctuations within the channel; this drift was fitted to the global trend of the data and used as the reference for determining frequency shift.

Out of this frequency variability are clear dips in the resonance that indicate cell passage over the structure. The dips represent the additive mass of multiple cells since yeast tend to clump and bud, especially when confined into narrow fluidic channels. It is also important to note that the budding yeast were not synchronized in their cell cycle, and were therefore likely to present a wide range of cell sizes and masses. Each dip represents a mass change of 12 ~ 17 pg according to the calibrated sensitivity. From the literature, yeast cells have been shown to range in mass from 4 ~ 10 pg as they undergo their cell cycle [123], and comparison of the measurements from this work with these external conclusions gives credibility to the result shown in Figure 5.16.

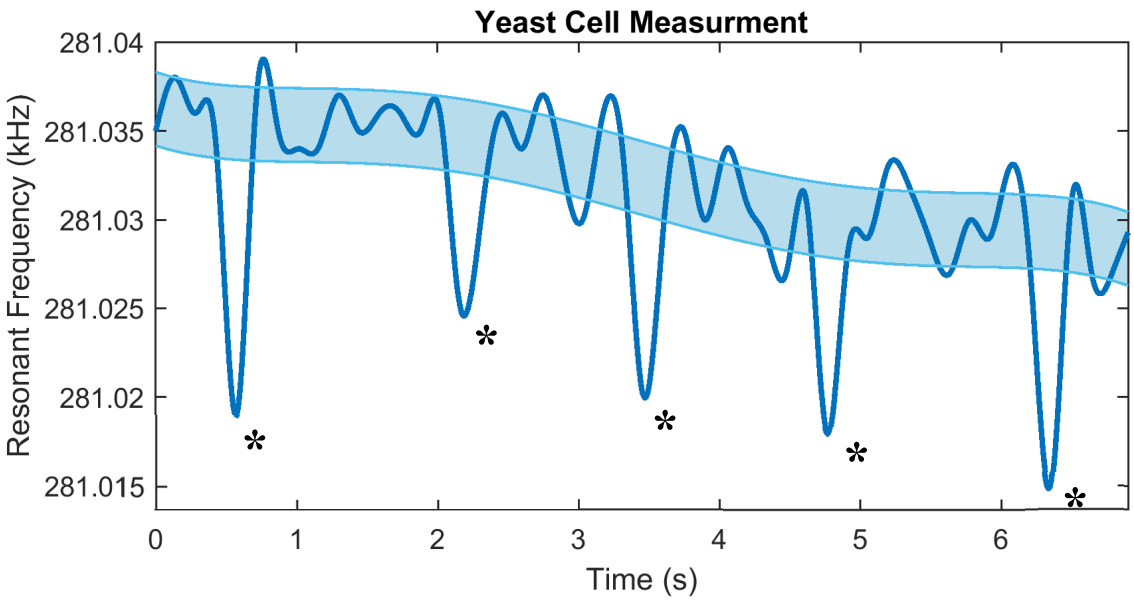

Figure 5.16. Cell mass measurement of yeast cell clumps, shown by asterisks. Single yeast cells were also measured, but they cannot be discerned from noise in the resonant frequency measurement.

Chapter 6

Conclusion

Section 6.1: Summary

The sensor/instrument described in this dissertation unites the techniques of laser trapping, optical characterization, and MEMS resonant mass sensing in a microfluidic-enabled device. The achieved sensitivity of ~1.14 Hz/pg is appropriate for cell characterization given adequate frequency stability, and this specification is comparable with the sensitivity of other published devices that target cell applications, 0.8 ~ 1.4 Hz/pg [20]. While achieving a similar sensitivity, the presented devices deliver the added benefit of enabled optical trapping to achieve higher repeatability and accuracy, and the optically compatibility of these devices can serve as a platform for the integration of a number of optical/near-infrared technologies including fluorescence imaging and flow cytometry. Certainly, further investigation is warranted for quality factor improvement.

External stimulation with light presents heating challenges compounded with other external influencing factors that affect device and system stability; thus, in addition to control of positional variability, characterization of these sources of error is critical to design and accurate measurement. The size of these devices is easily scaled in a versatile fabrication approach employing parylene, nominally conforming to the requirements of biological cells, including larger mammalian lines, in pursuit of important implications in

fundamental biology, pharmacology, and medicine. Furthermore, this approach is viable for devices with reduced structural mass and increased mass sensitivity, for target particles and samples on the nanoscale. Through system control, device design/scaling, and integration of optical technologies, this work lays the foundation for many exciting applications and developments. Most critically, this technology has clear importance in the study of cancer and disease, and the design of therapeutics to treat them.

Section 6.2: Other Applications

Aside from the utility of integrated optical trapping in a full laboratory set-up, interesting applications exist for lab-on-chip or even wearable technologies. However, noise sources and measurement error become serious obstacles during the transition outside of the laboratory. Optical trapping can serve as a mitigating technology in this setting, but it first requires miniaturization with integrated laser sources.

Integrated photonics have made great strides recently; Wu *et al.* demonstrated a monolayer semiconductor nanocavity laser for on-chip applications [124], and by exploiting this ability to achieve low-power on-chip lasing, a very compact, integrated trapping scheme could be realized. Since the trapping force is directly related to the gradient of the intensity profile, narrowing the intensity distribution increases the trapping force. One benefit of the nanocavity approach derives from the ability to confine its output intensity profile by virtue of the nano-sized lasing cavity. By using a photonic-crystal cavity to modulate the intensity profile, the required laser energy can be significantly reduced along with the laser's threat to cell life. By combining mass sensing silicon resonators with integrated silicon photonic trapping, the bio-sample movement and position could be controlled with high fidelity in a compact system comprising a fluidic channel that is readily compatible with less controlled environments or human motion.

CHAPTER 6. CONCLUSION

Optical laser trapping has seen application in vivo blood manipulation [125]. More specifically, anemia in the human body presents as a deficiency of red blood cells or hemoglobin in the blood. Hemoglobin is the protein in red blood cells that is responsible for conveying oxygen throughout the body, and maintaining an optimal hemoglobin level is paramount. It comprises about 95–97% of a red blood cell's dry mass and can be a key indicator in certain pathologies and therapeutics such as toxicity in cytotoxic chemotherapy [126]. Interestingly, the level of hemoglobin can be readily monitored using silicon micro-resonator devices [127], which could offer patients and their physicians time-evolution information for anemia and other important indicators with real-time, internet-connected data streams, as opposed to expensive and infrequent laboratory panels. In a clinical setting, these devices could be integrated into peripherally inserted central catheters (PICC) or Hickman lines for blood monitoring, and in mainstream settings, simple finger pricking, well-established for blood-glucose monitoring, could allow the patient to monitor blood indicators outside of medical laboratories.

Another particularly interesting application for these MEMS resonators could be in the future of dialysis. In fact, in bio-artificial kidney research, MEMS approaches have already found their way into enabling technologies, including engineered filtration membranes that utilize semiconductor fabrication methodologies [128]. The severity of anemia in dialysis patients is proportional to the degree of renal dysfunction [129], and over the course of treating chronic kidney disease (CKD), a noted variability in anemia has been observed. Causally, individuals with CKD have shown hemoglobin level fluctuations around target values even over short time periods. Fluctuations in these levels are associated with increased cardiovascular events and death, and a reduction in this variability is linked with improved clinical outcome [129]. Therefore, through both short- and long-term blood hemoglobin monitoring in real-time, physicians could better manage dialysis treatment. Dialysis itself is a life-saving medical procedure required by more than 2.5 million patients worldwide [130], and can often be a complication of prevalent conditions including high blood pressure or diabetes. Current dialysis methodologies have

a poor long-term survival outcome, given that the current technology cannot match that of normal kidney function. One large pitfall in the current approach, is the intermittency of dialysis treatment (averaging three times a week) causing fluid and uremic toxin levels to vary widely, unlike normal homeostasis achieved by functional kidneys. Cutting-edge research is actively pursuing a prototype wearable artificial kidney (WAK) [131].

The electrolyte and acid-base balance in the human body is an essential one, and it can directly affect critical vitals including fluid and blood pressure regulation. Therefore, WAK requires adequate monitoring through miniaturized sensor technology [130] that is both highly accurate and compatible with the motion of daily life. With enabled hemoglobin mass monitoring, data collection can give doctors and patients real-time feedback on how well the WAK system is cleansing the blood, and could give immediate notification if the system fails or needs adjustment. MEMS silicon resonant sensors can also resolve density changes in samples or aqueous solutions, which could detect changes in the WAK's filtration system or bubbles introduced into the circulating fluids or bloodstream. Even more, such devices have the potential to directly monitor bio-molecules, cells, and pathogens in a patient's blood or the output produced by the WAK, yielding tremendous data volumes critical in device feedback and potential revelations in the field of nephrology.

References

[1] H. Baltes and O. Brand, "CMOS-based microsensors and packaging," *Sensors and Actuators A,* vol. 92, no. 1–3, p. 1–9, 2001.

[2] J. Verd, A. Uranga, G. Abadal, J. Teva, F. Torres, F. Pérez-Murano, J. Fraxedas, J. Esteve and N. Barniol, "Monolithic mass sensor fabricated using a conventional technology with attogram resolution in air conditions," *Applied Physics Letters,* vol. 91, p. 013501, 2007.

[3] Y. T. Yang, C. Callegari, X. L. Feng, K. L. Ekinci and M. L. Roukes, "Zeptogram-scale nanomechanical mass sensing," *Nano Letters,* vol. 6, no. 4, pp. 583-586, 2006.

[4] A. K. Naik, M. S. Hanay, W. K. Hiebert, X. L. Feng and M. L. Roukes, "Towards single-molecule nanomechanical mass spectrometry," *Nature Nanotechnology,* vol. 4, pp. 445-450, 2009.

[5] Y. Arntz, J. D. Seelig, H. P. Lang, J. Zhang, P. Hunziker, J. P. Ramseyer, E. Meyer, M. Hegner and C. Gerber, "Label-free protein assay based on a nanomechanical cantilever array," *Nanotechnology,* vol. 14, no. 1, pp. 86-90, 2002.

[6] T. P. Burg, A. R. Mirza, N. Milovic, C. H. Tsau, G. A. Popescu, J. S. Foster and S. R. Manalis, "Vacuum-packaged suspended microchannel resonant mass sensor for biomolecular detection," *Journal of Microelectromechanical Systems,* vol. 15, no. 6, pp. 1466-1476, 2006.

[7] A. Gupta, D. Akin and R. Bashir, "Detection of bacterial cells and antibodies using surface micromachined thin silicon cantilever resonators," *Journal of Vacuum Science & Technology B: Microelectronics and Nanometer Structures Processing, Measurement, and Phenomena,* vol. 22, no. 6, pp. 2785-2791, 2004.

[8] T. P. Burg, M. Godin, S. M. Knudsen, W. Shen, G. Carlson, J. S. Foster, K. Babcock and S. R. Manalis, "Weighing of biomolecules, single cells and single nanoparticles in fluid," *Nature Letters,* vol. 446, pp. 1066-1069, 2007.

REFERENCES

[9] M. Godin, A. K. Bryan, T. P. Burg, K. Babcock and S. R. Manalis, "Measuring the mass, density, and size of particles and cells using a suspended microchannel resonator," *Applied Physics Letters,* vol. 91, no. 12, p. 123121, 2007.

[10] M. A. Mansor and M. R. Ahmad, "Single cell electrical characterization techniques," *International Journal of Molecular Sciences,* vol. 16, no. 6, pp. 12686-12712, 2015.

[11] G. Popescu, K. Park, M. Miracf and R. Bashir, "New technologies for measuring single cell mass," *Lab on a Chip,* vol. 14, no. 4, pp. 646-652, 2014.

[12] K. G. Phillips, C. R. Velasco, J. Li, A. Kolatkar, M. Luttgen, K. Bethel, B. Duggan, P. Kuhn and O. J. McCarty, "Optical quantification of cellular mass, volume, and density of circulating tumor cells identified in an ovarian cancer patient," *Frontiers in Oncology,* vol. 2, p. 72, 2012.

[13] T. Braun, V. Barwich, M. K. Ghatkesar, A. H. Bredekamp, C. Gerber, M. Hegner and H. P. Lang, "Micromechanical mass sensors for biomolecular detection in a physiological environment," *Physical Review E,* vol. 72, no. 3, p. 031907, 2005.

[14] B. Ilic, Y. Yang and H. G. Craighead, "Virus detection using nanoelectromechanical devices," *Applied Physics Letters,* vol. 85, no. 13, pp. 2604-2606, 2004.

[15] T. P. Burg and S. R. Manalis, "Suspended microchannel resonators for biomolecular detection," *Applied Physics Letters,* vol. 83, no. 13, pp. 2698-2700, 2003.

[16] S. Dohn, W. Svendsen, A. Boisen and O. Hansen, "Mass and position determination of attached particles on cantilever based mass," *Review of Scientific Instruments,* vol. 78, no. 10, p. 103303, 2007.

[17] K. Park, L. J. Millet, N. Kim, H. Li, X. Jin, G. Popescu, N. R. Aluru, K. J. Hsia and R. Bashir, "Measurement of adherent cell mass and growth," *PNAS,* vol. 107, no. 48, pp. 20691-20696, 2010.

[18] Y. Weng, F. F. Delgado, S. Son, T. P. Burg, S. C. Wasserman and S. R. Manalis, "Mass sensors with mechanical traps for weighing single cells in different fluids," *Lab on a Chip,* vol. 11, pp. 4174-4180, 2011.

[19] R. Bashir, "Microcantilevers track single-cell mass," *Nature Biotechnology,* vol. 34, no. 11, pp. 1125-1126, 2016.

[20] N. Cermak, S. Olcum, F. F. Delgado, S. C. Wasserman, K. R. Payer, M. A. Murakami, S. M. Knudsen, R. J. Kimmerling, M. M. Stevens, Y. Kikuchi, A. Sandikci, M. Ogawa, V. Agache, F. Baléras, D. M. Weinstock and S. R. Manalis, "High-throughput measurement of single-cell growth rates using serial microfluidic mass sensor arrays," *Nature Biotechnology,* vol. 34, no. 10, pp. 1052-1059, 2016.

[21] J.-Y. Tinevez, J. Dragavon, L. Baba-Aissa, P. Roux, E. Perret, A. Canivet, V. Galy and S. Shorte, "Methods in Enzymology, Volume 506," in *Imaging and Spectroscopic Analysis of Living Cells: Imaging Live Cells in Health and Disease*, Cambridge, Academic Press, 2012, pp. 291-309.

[22] Y. Liu, D. K. Cheng, G. J. Sonek, M. W. Berns, C. F. Chapman and B. J. Tromberg, "Evidence for localized cell heating induced by infrared optical tweezers," *Biophysical Journal,* vol. 68, no. 5, pp. 2137-2144, 1995.

[23] P. Jing, J. Wu, G. W. Liu, E. G. Keeler, S. H. Pun and L. Y. Lin, "Photonic crystal optical tweezers with high efficiency for live biological samples and viability characterization," *Scientific Reports,* vol. 6, p. 19924, 2016.

[24] A. Tzur, R. Kafri, V. S. LeBleu, G. Lahav and M. W. Kirschner, "Cell growth and size homeostasis in proliferating animal cells," *Science,* vol. 325, no. 5937, pp. 167-171, 2009.

[25] D. Hevia, A. Rodriguez-Garcia, M. Alonso-Gervós, I. Quirós-González, H. M. Cimadevilla, C. Gómez-Cordovés, R. M. Sainz and J. C. Mayo, "Cell volume and geometric parameters determination in living cells using confocal microscopy and 3D reconstruction," *Protocol Exchange,* 2011.

[26] P. H. O'Farrell, "How Metazoans Reach Their Full Size: The Natural History of Bigness," in *Cell Growth: Control of Cell Size*, Cold Spring Harbor, Cold Spring Harbor Press, 2004, pp. 1-22.

[27] W. H. Coulter, "Means for counting particles suspended in a fluid". United States of America Patent US2656508 A, 27 August 1949.

[28] M. Koch, A. G. R. Evans and A. Brunnschweiler, "Design and fabrication of a micromachined Coulter counter," *Journal of Micromechanics and Microengineering,* vol. 9, no. 2, pp. 159-161, 1999.

[29] Y. E. Korchev, J. Gorelik, M. J. Lab, E. V. Sviderskaya, C. L. Johnston, C. R. Coombes, I. Vodyanoy and C. R. W. Edwards, "Cell volume measurement using scanning ion conductance microscopy," *Biophysical Journal,* vol. 78, pp. 451-457, 2000.

REFERENCES

[30] C. Koch, Biophysics of Computation: Information Processing in Single Neurons, New York: Oxford University Press, 1999.

[31] J. Golowasch, G. Thomas, A. L. Taylor, A. Patel, A. Pineda, C. Khalil and F. Nadim, "Membrane capacitance measurements revisited: dependence of capacitance value on measurement method in nonisopotential neurons," *Journal of Neurophysiology,* vol. 102, no. 4, pp. 2161-2175, 2009.

[32] H. Satoh, L. M. D. Delbridge, L. A. Blatter and D. M. Bers, "Surface:volume relationship in cardiac myocytes studied with confocal microscopy and membrane capacitance measurements: species-dependence and developmental effects," *Biophysical Journal,* vol. 70, pp. 1494-1504, 1996.

[33] R. J. Errington and N. S. White, "Measuring Dynamic Cell Volume In Situ by Confocal Microscopy," in *Confocal Microscopy Methods and Protocols*, Totowa, Humana Press, 1999, pp. 315-340.

[34] D. E. Buetow, J. K. Stevens, I. T. Cameron, L. R. Mills, G. M. Padilla, J. E. Trogadis and A. M. Zimmerman, Three-Dimensional Confocal Microscopy: Volume Investigation of Biological Specimens, San Diego: Academic Press, 1994.

[35] H. Satoh, L. M. D. Delbridge, L. A. Blatter and D. M. Bers, "Surface:Volume relationship in cardiac myocytes studied with confocal microscopy and membrane capacitance measurements: species dependence and developmental effects," *Biophysical Journal,* vol. 70, pp. 1494-1504, 1996.

[36] T. A. Zangle and M. A. Teitell, "Live-cell mass profiling: an emerging approach in quantitative biophysics," *Nature Methods,* vol. 11, no. 12, pp. 1221-1228, 2014.

[37] T. A. Zangle, J. Chun, J. Zhang, J. Reed and M. A. Teitell, "Quantification of biomass and cell motion in human pluripotent stem cell colonies," *Biophysical Journal,* vol. 105, no. 3, pp. 593-601, 2013.

[38] J. Chun, T. A. Zangle, T. Kolarova, R. S. Finn, M. A. Teitell and J. Reed, "Rapidly quantifying drug sensitivity of dispersed and clumped breast cancer cells by mass profiling," *Analyst,* vol. 137, no. 23, pp. 5495-5498, 2012.

[39] M. S. Luchansky, A. L. Washburn, T. A. Martin, M. Iqbal, L. C. Gunn and R. C. Baileya, "Characterization of the evanescent field profile and bound mass sensitivity of a label-free silicon photonic microring resonator biosensing platform," *Biosensors and Bioelectronics,* vol. 26, no. 4, pp. 1283-1291, 2010.

REFERENCES

[40] P. N. Abadian, C. P. Kelley and E. D. Goluch, "Cellular analysis and detection using surface plasmon resonance techniques," *Analytical Chemistry,* vol. 86, no. 6, pp. 2799-2812, 2014.

[41] K. A. Marx, T. Zhou, A. Montrone, H. Schulze and S. J. Braunhut, "A quartz crystal microbalance cell biosensor: detection of microtubule alterations in living cells at nM nocodazole concentrations," *Biosensors and Bioelectronics,* vol. 16, no. 9-12, pp. 773-782, 2001.

[42] G. Wang, A. H. Dewilde, J. Zhang, A. Pal, M. Vashist, D. Bello, K. A. Marx, S. J. Braunhut and J. M. Therrien, "A living cell quartz crystal microbalance biosensor for continuous monitoring of cytotoxic responses of macrophages to single-walled carbon nanotubes," *Particle and Fibre Toxicology,* vol. 8, no. 4, 2011.

[43] Y. Luo, T. Liu, J. Zhu, L. Kong, W. Wang and L. Tan, "Label-free and sensitive detection of thrombomodulin, a marker of endothelial cell injury, using quartz crystal microbalance," *Analytical Chemistry,* vol. 87, no. 22, pp. 11277-11284, 2015.

[44] F. R. Blom, S. Bouwstra, J. H. J. Fluitman and M. Elwenspoek, "Resonating silicon beam force sensor," *Sensors and Actuators,* vol. 17, no. 3-4, pp. 513-519, 1989.

[45] S. Bouwstra, R. Legtenberg, H. A. Tilmans and M. Elwenspoek, "Resonating microbridge mass flow sensor," *Sensors and Actuators A: Physical,* vol. 21, no. 1-3, pp. 332-335, 1990.

[46] K. E. B. Thornton, D. Uttamchandani and B. Culshaw, "A sensitive optically excited resonator pressure sensor," *Sensors and Actuators A: Physical,* vol. 24, no. 1, pp. 15-19, 1990.

[47] M. Godin, F. F. Delgado, S. Son, W. H. Grover, A. K. Bryan, A. Tzur, P. Jorgensen, K. Payer, A. D. Grossman, M. W. Kirschner and S. R. Manalis, "Using buoyant mass to measure the growth of single cells," *Nature Methods,* vol. 7, no. 5, pp. 387-390, 2010.

[48] J. Lee, A. K. Bryan and S. R. Manalis, "High precision particle mass sensing using microchannel resonators in the second vibration mode," *Review of Scientific Instruments,* vol. 82, no. 2, p. 023704, 2011.

[49] K. Park, J. Jang, D. Irimia, J. Sturgis, J. Lee, J. P. Robinson, M. Toner and R. Bashir, "'Living cantilever arrays' for characterization of mass of single live cells in fluids," *Lab on a Chip,* vol. 8, no. 7, pp. 1034-1041, 2008.

[50] S. M. Han, H. Benaroya and T. Wei, "Dynamics of transversely vibrating beams using four engineering theories," *Journal of Sound and Vibration,* vol. 225, no. 5, pp. 935-988, 1999.

[51] M. Avcar, "Free vibration analysis of beams considering different geometric characteristics and boundary conditions," *International Journal of Mechanics and Applications,* vol. 4, no. 3, pp. 94-100, 2014.

[52] G. Stemme, "Resonant silicon sensors," *Journal of Micromechanics and Microengineering,* vol. 1, no. 2, pp. 113-125, 1991.

[53] W. H. Grover, A. K. Bryan, M. Diez-Silva, S. Suresh, J. M. Higgins and S. R. Manalis, "Measuring single-cell density," *PNAS,* vol. 108, no. 27, pp. 10992-10996, 2011.

[54] A. Boisen, S. Dohn, S. S. Keller, S. Schmid and M. Tenje, "Cantilever-like micromechanical sensors," *Reports on Progress in Physics,* vol. 74, no. 3, p. 036101, 2011.

[55] F. R. Blom, S. Bouwstra, M. Elwenspoek and J. H. J. Fiuitman, "Dependence of the quality factor of micromachined silicon beam resonators on pressure and geometry," *Journal of Vacuum Science & Technology B,* vol. 10, no. 1, pp. 19-26, 1992.

[56] Z. Hao, A. Erbil and F. Ayazi, "An analytical model for support loss in micromachined beam resonators with in-plane flexural vibrations," *Sensors and Actuators A,* vol. 109, no. 1-2, pp. 156-164, 2003.

[57] S. Ghaffari, E. J. Ng, C. H. Ahn, Y. Yang, S. Wang, V. A. Hong and T. W. Kenny, "Accurate modeling of quality factor behavior of complex silicon MEMS resonators," *Journal of Microelectromechanical Systems,* vol. 24, no. 2, pp. 276-288, 2015.

[58] T. P. Burg, Suspended microchannel resonators for biomolecular detection, Cambridge: Massachusetts Institute of Technology, 2005.

[59] J. Tamayo, A. D. L. Humphris, R. J. Owen and M. J. Miles, "High-Q dynamic force microscopy in liquid and its application to living cells," *Biophysical Journal,* vol. 81, no. 1, pp. 526-537, 2001.

[60] K. L. Ekinci, Y. T. Yang and M. L. Roukes, "Ultimate limits to inertial mass sensing based upon nanoelectromechanical systems," *Journal of Applied Physics,* vol. 95, no. 5, pp. 2682-2689, 2004.

[61] K. C. Neuman and S. M. Block, "Optical trapping," *Review of Scientific Instruments,* vol. 75, no. 9, pp. 2787-2809, 2004.

[62] E. G. Keeler, P. Jing, J. Wu, C. Zou and L. Y. Lin, "MEMS resonant mass sensor with enabled optical trapping," in *Nano/Micro Engineered and Molecular Systems (NEMS), 2017 IEEE 12th International Conference on*, Los Angeles, 2017.

[63] P. Jing, J. Wu and L. Y. Lin, "Patterned optical trapping with two-dimensional photonic crystals," *ACS Photonics,* vol. 1, no. 5, pp. 398-402, 2014.

[64] B. K. Wilson, T. Mentele, S. Bachar, E. Knouf, A. Bendoraite, M. Tewari, S. H. Pun and L. Y. Lin, "Nanostructure-enhanced laser tweezers for efficient trapping and alignment of particles," *Optics Express,* vol. 18, no. 15, pp. 16005-16013, 2010.

[65] G. E. Loeb, M. J. BaK, M. Salcman and E. M. Schmidt, "Parylene as a chronically stable, reproducible microelectrode insulator," *IEEE Transactions on Biomedical Engineering,* Vols. BME-24, no. 2, pp. 121-128, 1977.

[66] T. Chen, D. Wuu, C. Wu, C. Chiang, Y. Chen and R. Horng, "Improvements of permeation barrier coatings using encapsulated parylene interlayers for flexible electronic applications," *Plasma Processes and Polymers,* vol. 4, no. 2, pp. 180-185, 2007.

[67] N. Kim, W. J. P. Jr., B. Domercq, B. Kippelen and S. Graham, "A hybrid encapsulation method for organic electronics," *Applied Physics Letters,* vol. 94, no. 16, p. 163308, 2009.

[68] J. T. Kuo, B. J. Kim, S. A. Hara, C. D. Lee, C. A. Gutierrez, T. Q. Hoang and E. Meng, "Novel flexible Parylene neural probe with 3D sheath structure for enhancing tissue integration," *Lab on a Chip,* vol. 13, pp. 554-561, 2013.

[69] S. Takeuchi, D. Ziegler, Y. Yoshida, K. Mabuchi and T. Suzuki, "Parylene flexible neural probes integrated with microfluidic channels," *Lab on a Chip,* vol. 5, pp. 519-523, 2005.

[70] C. Hassler, R. P. v. Metzen, P. Ruther and T. Stieglitz, "Characterization of parylene C as an encapsulation material for implanted neural prostheses," *Journal of Biomedical Materials Research,* vol. 93B, no. 1, pp. 266-274, 2010.

[71] Y.-F. Rui, J.-Q. Liu, B. Yang, K.-Y. Li and C.-S. Yang, "Parylene-based implantable platinum-black coated wire microelectrode for orbicularis oculi

muscle electrical stimulation," *Biomedical Microdevices,* vol. 14, no. 2, pp. 367-373, 2012.

[72] P.-J. Chen, D. C. Rodger, M. S. Humayun and Y.-C. Tai, "Floating-disk parylene microvalves for self-pressure-regulating flow controls," *Journal of Microelectromechanical Systems,* vol. 17, no. 6, pp. 1352-1361, 2008.

[73] S. Sukas, A. E. Erson, C. Sert and H. Kulah, "A parylene-based dual channel microelectrophoresis system for rapid mutation detection via heteroduplex analysis," *Electrophoresis,* vol. 29, no. 18, pp. 3752-3758, 2008.

[74] C. A. Gutierrez and E. Meng, "Impedance-based force transduction within fluid-filled parylene microstructures," *Journal of Microelectromechanical Systems,* vol. 20, no. 5, pp. 1098-1108, 2011.

[75] E. Meng, P.-Y. Li and Y.-C. Tai, "Plasma removal of parylene-C," *Journal of Micromechanics and Microengineering,* vol. 18, p. 045004, 2008.

[76] Specialty Coating Systems, Inc., "SCS Parylene Properties," Specialty Coating Systems, Inc., Indianapolis, 2016.

[77] Parylene Engineering, "Thermal Properties of Parylene C vs. Epoxy, Silicone, and Urethanes," Parylene Engineering, 2016. [Online]. Available: http://www.paryleneengineering.com/thermal_properties_of_parylene.htm. [Accessed 05 2016].

[78] T. Harder, T.-J. Yao, Q. He, C.-Y. Shih and Y.-C. Tai, "Residual stress in thin-film parylene-c," in *IEEE Micro Electro Mechanical Systems*, Las Vegas, 2002.

[79] R. Machorro, L. E. Regalado and J. M. Siqueiros, "Optical properties of parylene and its use as substrate in beam splitters," *Applied Optics,* vol. 30, no. 19, pp. 2778-2781, 1991.

[80] C. Schinke, P. C. Peest, J. Schmidt, R. Brendel, K. Bothe, M. R. Vogt, I. Kröger, S. Winter, A. Schirmacher, S. Lim, H. T. Nguyen and D. MacDonald, "Uncertainty analysis for the coefficient of band-to-band absorption of crystalline silicon," *AIP Advances,* vol. 5, no. 6, p. 067168, 2015.

[81] T. M. Squires and S. R. Quake, "Microfluidics: Fluid physics at the nanoliter scale," *Reviews of Modern Physics,* vol. 77, no. 3, pp. 977-1026, 2005.

[82] Crane Co., Flow of Fluids, through Valves, Fittings, and Pipe, New York: Crane Co., 1982.

[83] B. Kim, M. A. Hopcroft, R. N. Candler, C. M. Jha, M. Agarwal, R. Melamud, S. A. Chandorkar, G. Yama and T. W. Kenny, "Temperature dependence of quality factor in MEMS resonators," *Journal of Microelectromechanical Systems,* vol. 17, no. 3, pp. 755-766, 2008.

[84] L. Y. Lin and E. G. Keeler, "Progress of MEMS scanning micromirrors for optical bio-imaging," *Micromachines,* vol. 6, no. 11, pp. 1675-1689, 2015.

[85] M. I. Younis, E. M. Abdel-Rahman and A. Nayfeh, "A reduced-order model for electrically actuated microbeam-based MEMS," *Journal of Microelectromechanical Systems,* vol. 12, no. 5, pp. 672-680, 2003.

[86] B. H. Kim, D. P. Kern, S. Raible and U. Weimar, "Fabrication of micromechanical mass-sensitive resonators with increased mass resolution using SOI substrate," *Microelectronic Engineering,* Vols. 61-62, pp. 947-953, 2002.

[87] J. Kiihamäki, J. Dekker, P. Pekko, H. Kattelus, T. Sillanpää and T. Mattila, "‘‘Plug-up’’–a new concept for fabricating SOI MEMS devices," *Microsystem Technologies,* vol. 10, no. 5, pp. 346-350, 2004.

[88] K. Yoshimoto, R. Suzuki, Y. Ishikawa and K. Wada, "Bandgap control using strained beam structures for Si photonic devices," *Optics Express,* vol. 18, no. 25, pp. 26492-26498, 2010.

[89] E. Serra, M. Bonaldi, A. Borrielli, L. Conti, G. Pandraud and P. M. Sarro, "Low loss single-crystal silicon mechanical resonators for the investigation of thermal noise statistical properties," *Sensors and Actuators A: Physical,* vol. 227, pp. 48-54, 2015.

[90] Z. Yapu, "Stiction and anti-stiction in MEMS and NEMS," *Acta Mechanica Sinica,* vol. 19, no. 1, pp. 1-10, 2003.

[91] R. A. Barton, B. Ilic, S. S. Verbridge, B. R. Cipriany, J. M. Parpia and H. G. Craighead, "Fabrication of a nanomechanical mass sensor containing a nanofluidic channel," *Nano Letters,* vol. 10, no. 6, pp. 2058-2063, 2010.

[92] G. Vidal-Álvarez, E. Marigó, F. Torres and N. Barniol, "Fabrication and measurement of a suspended nanochannel microbridge resonator monolithically integrated with CMOS readout circuitry," *Micromachines,* vol. 7, no. 3, p. 40, 2016.

[93] J. Charmet, J. Bitterli, O. Sereda, M. Liley, P. Renaud and H. Keppner, "Optimizing parylene C adhesion for MEMS processes: potassium hydroxide

wet etching," *Journal of Microelectromechanical Systems,* vol. 22, no. 4, pp. 855-864, 2013.

[94] Q. He, E. Meng, Y.-C. Tai, C. M. Rutherglen, J. Erickson and J. Pine, "Parylene neuro-cages for live neural networks study," in *TRANSDUCERS, Solid-State Sensors, Actuators and Microsystems*, Boston, 2003.

[95] K. Walsh, J. Norville and Y.-C. Tai, "Photoresist as a sacrificial layer by dissolution in acetone," in *Micro Electro Mechanical Systems (MEMS)*, Interlaken, 2001.

[96] B. A. Peeni, M. L. Lee, A. R. Hawkins and A. T. Woolley, "Sacrificial layer microfluidic device fabrication methods," *Electrophoresis,* vol. 27, no. 24, pp. 4888-4895, 2006.

[97] J. R. Lee, J. P. Barber, Z. A. George, M. L. Lee, H. Schmidt and A. R. Hawkins, "Microchannels with rectangular and arched core shapes fabricated using sacrificial etching," *Journal of Micro/nanolithography, MEMS, and MOEMS,* vol. 6, no. 1, p. 013010, 2007.

[98] C.-T. Seo, C.-H. Bae, D.-S. Eun, J.-K. Shin and J.-H. Lee, "Fabrication of circular-type microchannel using photoresist reflow and isotropic etching for microfluidic devices," *Japanese Journal of Applied Physics,* vol. 43, no. 11A, pp. 7773-7776, 2004.

[99] M. Shikida, K. Sato, K. Tokoro and D. Uchikawa, "Differences in anisotropic etching properties of KOH and TMAH solutions," *Sensors and Actuators,* vol. 80, no. 2, pp. 179-188, 2000.

[100] K. R. Williams, K. Gupta and M. Wasilik, "Etch rates for micromachining processing—Part II," *Journal of Microelectromechanical Systems,* vol. 12, no. 6, pp. 761-778, 2003.

[101] R. Khakpour, S. R. M. Mansouri and A. Bahadorimehr, "Analytical comparison for square, rectangular and circular diaphragms in MEMS applications," in *Electronic Devices, Systems and Applications (ICEDSA)*, Kuala Lumpur, 2010.

[102] K. Petersen, "Silicon as a mechanical material," *Proceedings of the IEEE,* vol. 70, no. 5, pp. 420-457, 1982.

[103] J.Rossmeisl, Z.-W. Qu, H. Zhu, G.-J. Kroes and J.K.Nørskov, "Electrolysis of water on oxide surfaces," *Journal of Electroanalytical Chemistry,* vol. 607, no. 1-2, pp. 83-89, 2007.

REFERENCES

[104] M. Ozkan, M. Wang, C. Ozkan, R. Flynn and S. Esener, "Optical manipulation of objects and biological cells in microfluidic devices," *Biomedical Microdevices,* vol. 5, no. 1, pp. 61-67, 2003.

[105] Y. Nakayama, Introduction to Fluid Mechanics, Oxford: Butterworth-Heinemann, 2000.

[106] Nanoscribe, "Microprinting on the micrometer scale - Nanoscribe GmbH," Nanoscribe, [Online]. Available: http://www.nanoscribe.de/en/. [Accessed 11 10 2017].

[107] S. Byun, S. Son, D. Amodei, N. Cermak, J. Shaw, J. H. Kang, V. C. Hecht, M. M. Winslow, T. Jacks, P. Mallick and S. R. Manalis, "Characterizing deformability and surface friction of cancer cells," *PNAS,* vol. 110, no. 19, pp. 7580-7585, 2013.

[108] P. Jing, Y. Liu, E. G. Keeler, N. M. Cruz, B. S. Freedman and L. Y. Lin, "Optical tweezers system for live stem cell organization at the single-cell level," *Biomedical Optics Express,* vol. 9, no. 2, pp. 771-779, 2018.

[109] A. Busnaina, H. Lin, N. Moumen, J.-w. Feng and J. Taylor, "Particle adhesion and removal mechanisms in post-CMP cleaning processes," *IEEE Transactions on Semiconductor Manufacturing,* vol. 15, no. 4, pp. 374-382, 2002.

[110] B. M. Gumbiner, "Cell adhesion: the molecular basis of tissue architecture and morphogenesis," *Cell,* vol. 84, no. 3, pp. 345-357, 1996.

[111] E. G. Keeler, J. Wu, P. Jing and L. Y. Lin, "MEMS resonator and photonic crystal integration for enhanced cellular mass sensing," in *Optics in the Life Sciences*, Vancouver, 2015.

[112] F. L. Pedrotti, L. S. Pedrotti and L. M. Pedrotti, Introduction to Optics, Upper Saddle River: Pearson Prentice Hall, 2007.

[113] D. R. Lide, CRC Handbook of Chemistry and Physics, 85th Edition, Boca Raton: CRC Press, 2004.

[114] T. P. Burg, J. E. Sader and S. R. Manalis, "Nonmonotonic energy dissipation in microfluidic resonators," *Physical Review Letters,* vol. 102, no. 22, p. 228103, 2009.

[115] Z. J. Davis, G. Abadal, O. Kuhn, O. Hansen, F. Grey and A. Boisen, "Fabrication and characterization of nanoresonating devices for mass

detection," *Journal of Vacuum Science & Technology B,* vol. 18, no. 2, pp. 612-616, 2000.

[116] M. Laat, H. P. Garza, J. L. Herder and M. K. Ghatkesar, "A review on in situ stiffness adjustment methods in MEMS," *Journal of Micromechanics and Microengineering,* vol. 26, no. 6, p. 063001, 2016.

[117] S. Weigert, M. Dreier and M. Hegner, "Frequency shifts of cantilevers vibrating in various media," *Applied Physics Letters,* vol. 69, no. 19, pp. 2834-2836, 1996.

[118] C. Liu, Foundations of MEMS, Upper Saddle River: Pearson Prentice Hall, 2006.

[119] E. G. Keeler, P. Jing, J. Wu, C. Zou and L. Y. Lin, "MEMS resonant mass sensor with enabled optical manipulation," *IEEE Transactions on Nanotechnology,* vol. 17, no. 4, pp. 1-5, 2018.

[120] N. Ono, K. Kitamura, K. Nakajima and Y. Shimanuki, "Measurement of Young's modulus of silicon single crystal at high temperature and its dependency on boron concentration using the flexural vibration method," *Japanese Journal of Applied Physics,* vol. 39, no. 1, pp. 368-371, 2000.

[121] K. Shirai, "Temperature dependence of Young's modulus of silicon," *Japanese Journal of Applied Physics,* vol. 52, no. 8R, p. 088002, 2013.

[122] J. C.-H. Lin, P. Deng, G. Lam, B. Lu, Y.-K. Lee and Y.-C. Tai, "Creep of parylene-C film," in *Solid-State Sensors, Actuators and Microsystems Conference (TRANSDUCERS)*, Beijing, 2011.

[123] A. K. Bryan, A. Goranov, A. Amon and S. R. Manalis, "Measurement of mass, density, and volume during the cell cycle of yeast," *PNAS,* vol. 107, no. 3, pp. 999-1004, 2010.

[124] S. Wu, S. Buckley, J. R. Schaibley, L. Feng, J. Yan, D. G. Mandrus, F. Hatami, W. Yao, J. Vučković, A. Majumdar and X. Xu, "Monolayer semiconductor nanocavity lasers with ultralow thresholds," *Nature,* vol. 520, p. 69–72, 2015.

[125] M.-C. Zhong, X.-B. Wei, J.-H. Zhou, Z.-Q. Wang and Y.-M. Li, "Trapping red blood cells in living animals using optical tweezers," *Nature Communications,* vol. 4, p. 1768, 2012.

[126] L. Balducci, "Anemia, cancer, and aging," *Cancer Control,* vol. 10, no. 6, p. 478–486, 2003.

[127] R. Malka, F. F. Delgado, S. R. Manalis and J. M. Higgins, "In vivo volume and hemoglobin dynamics of human red blood cells," *Computational Biology,* vol. 10, no. 10, p. e1003839, 2014.

[128] H. D. Humes, D. Buffington, A. J. Westover, S. Roy and W. H. Fissell, "The bioartificial kidney: current status and future promise," *Pediatric Nephrology,* vol. 29, no. 3, p. 343–351, 2014.

[129] K. Kalantar-Zadeh and G. R. Aronoff, "Hemoglobin variability in anemia of chronic kidney disease," *Journal of the American Society of Nephrology,* vol. 20, no. 3, p. 479–487, 2009.

[130] J. P. Kooman, J. A. Joles and K. G. F. Gerritsen, "Creating a wearable artificial kidney: where are we now?," *Expert Review of Medical Devices,* vol. 12, no. 4, p. 373–376, 2015.

[131] V. Gura, M. B. Rivara, S. Bieber, R. Munshi, N. C. Smith, L. Linke, J. Kundzins, M. Beizai, C. Ezon, L. Kessler and J. Himmelfarb, "A wearable artificial kidney for patients with end-stage renal disease," *JCI Insight,* vol. 1, no. 8, p. e86397, 2016.

Appendix

Appendix A: Detailed Backside Process Flow

	Cleaning Step
	Lithography Step
	Metrology Step
	Key Step

Sequence	**Step**	**Side**	**Equipment**	**Parameters/Notes**
0	*START*		WAFER	Wafer Diameter: 100 mm Device Thickness: 2 µm BOX Thickness: 5 µm Handle Thickness: 350 µm
1	*CLEAN*		BATH2-RCA	10 min. in SC-1 and 10 min. in SC-2
2	*TREATMENT*		HMDS-OVEN	Standard HMDS treatment
3	*SPIN RESIST*	*FR*	SPIN1|2-AUTO	Resist: AZ1512 Expected Thickness: ~1.1 µm Recipe (Time, Speed, Acceleration): 1 | 2 s, 500 RPM, 4000 RPM/s 2 | 30 s, 4000 RPM, 4000 RPM/s
4	*BAKE RESIST*	*FR*	HOTPLATE	110°C, 90 seconds

5	*EXPOSE*	*FR*	ABM-ALIGNER	MASK1-PhC (includes alignment) Intensity: ~20 mW/cm^2 Time: 3.1 seconds
6	*DEVELOP*	*FR*	BATH5-DEVELOP	AZ340:DI Water (1:4), 50 seconds
7	*INSPECT*	*FR*	NIKON	Optical microscopy
8	*MEASURE*	*FR*	ALPHA STEP	Measure step height of AZ1512
9↓	*ETCH Si PhC*	*FR*	ICP-FL	Temp: 20°C Pressure: 15 mTorr RF Forward: 30 W ICP Forward: 1200 W SF_6: 25 sccm C_4F_8: 19 sccm He flow: ~11 sccm Time: 25 seconds Etch rate: ~18 nm/s Resist etch rate: ~ 3 nm/s Etch depth: ~350 nm. *To create photonic crystal.*
10	*ETCH CALIBRATION*	*FR*	ALPHA STEP	*For combined resist + Si etch.*
↻	*ETCH Si PhC*	*FR*	*VISION-RIE*	Repeat **Steps 9–10** as required
11	*RESIST STRIP*	*FR*	EKC	Strip in EKC for 5 minutes
12	*CLEAN*	*FR*	BARREL-ETCH	Power: 125 W Time: 5 minutes

13	*INSPECT*	*FR*	NIKON	Optical microscopy (green filter)
14	*ETCH CALIBRATION*	*FR*	ALPHA STEP	For final depth of the PhC (z_{PhC})
	TREATMENT		HMDS-OVEN	Standard HMDS treatment
15	*SPIN RESIST*	*FR*	SPIN1|2-AUTO	Resist: AZ1512 Expected Thickness: ~1.1 µm Recipe (Time, Speed, Acceleration): 1 | 2 s, 500 RPM, 4000 RPM/s 2 | 30 s, 4000 RPM, 4000 RPM/s
16	*BAKE RESIST*	*FR*	HOTPLATE	120°C, 120 seconds, Proximity mode (~1 mm) for backside cleanliness
17	*COOL RESIST*	*FR*	NONE	Cool resist layer for > 1 minute
18	*SPIN RESIST*	*BK*	SPIN1|2-AUTO	Resist: AZ9260 Expected Thickness: ~10 µm Recipe (Time, Speed, Acceleration): 1 | 5 s, 350 RPM, 1500 RPM/s 2 | 3 s, 0 RPM, 1000 RPM/s 3 | 5 s, 350 RPM, 2000 RPM/s 4 | 30 s, 1800 RPM, 2000 RPM/s
19	*BAKE RESIST*	*BK*	HOTPLATE	120°C, 360 seconds, Proximity mode (~1 mm)
20	*REHYDRATE RESIST*	*BK*	NONE	Rehydrate resist for > 30 minutes
21	*EXPOSE*	*BK*	EVG-ALIGNER	MASK2-Port Intensity: ~20 mW/cm^2 Time: 65 seconds

				Mode: Hard Contact Alignment: Cross Hairs
22	*DEVELOP*	*BK*	BATH5-DEVELOP	AZ400K:DI Water (1:4), 7 minutes
23	*REST RESIST*	*BK*	NONE	Rest resist overnight in white light
24	*INSPECT*	*BK*	NIKON	Optical microscopy (green filter)
25	*MEASURE*	*BK*	FILMETRICS	Characterize resist thickness
26	*EXPOSE*	*BK*	ABM-AIGNER	Flood Exposure Intensity: ~20 mW/cm^2 Time: 20 seconds
27↓	*ETCH Si Ports*	*BK*	OXFORD-DRIE	Temp: 15°C He flow: ~11 sccm Total Time: 150 minutes Etch rate: ~2.3 µm/min Resist etch rate: ~3 nm/s Etch depth: ~350 µm. **Etch** Pressure: 26 mTorr RF Forward: 25 W ICP Forward: 1500 W SF_6: 100 sccm C_4F_8: 0 sccm Time: 7 seconds **Deposit** Pressure: 20 mTorr RF Forward: 10 W ICP Forward: 1650 W SF_6: 0 sccm C_4F_8: 100 sccm Time: 5 seconds

				To port through silicon substrate.
28	*ETCH CALIBRATION*	*FR*	WYKO	Interferometric profilometry for hole depth
↻	*ETCH Si Ports*	*FR*	*OXFORD-DRIE*	Repeat **Steps 27–28** as required
29	*RESIST STRIP*	*FR*	EKC	Strip in EKC for 5 minutes
30	*CLEAN*	*FR*	BARREL-ETCH	Power: 125 W Time: 5 minutes
31	*ETCH CALIBRATION*	*FR*	WYKO	Interferometric profilometry for final port depth verification
32	*INSPECT*	*FR*	NIKON	Optical microscopy
33	*CLEAN*		BATH2-RCA	10 min. in SC-1 and 10 min. in SC-2
34	*TREATMENT*		HMDS-OVEN	Standard HMDS treatment
35	*SPIN RESIST*	*FR*	SPIN1|2-AUTO	Resist: AZ1512 Expected Thickness: ~1.1 µm Recipe (Time, Speed, Acceleration): 1 | 2 s, 500 RPM, 4000 RPM/s 2 | 30 s, 4000 RPM, 4000 RPM/s
36	*BAKE RESIST*	*FR*	HOTPLATE	110°C, 90 seconds
37	*EXPOSE*	*FR*	ABM-ALIGNER	MASK3-Beam Intensity: ~20 mW/cm^2 Time: 3.1 seconds

38	*DEVELOP*	*FR*	BATH5-DEVELOP	AZ340:DI Water (1:4), 50 seconds
39	*INSPECT*	*FR*	NIKON	Optical microscopy (green filter)
40	*DESCUM*	*FR*	VISION-RIE	Pressure: 75 mTorr RF Power: 30 W O_2: 50 sccm Time: 1 minute
41	*ETCH Si Beam*	*FR*	VISION-RIE	Pressure: 60 mTorr RF Power: 120 W SF_6: 20 sccm CHF_3: 8 sccm Time: 11 minutes Etch rate: ~300 nm/min. *Etch until silicon cleared and oxide visible.*
42	*RESIST STRIP*	*FR*	EKC	Strip in EKC for 5 minutes
43	*CLEAN*	*FR*	BARREL-ETCH	Power: 125 W Time: 5 minutes
44	*INSPECT*	*FR*	NIKON	Optical microscopy
45	*MEASURE*	*FR*	ALPHA STEP	For final beam thickness (z_{Beam})
46	*TREATMENT*		HMDS-OVEN	Standard HMDS treatment
47	*SPIN RESIST*	*FR*	SPIN1|2-AUTO	Resist: AZ9260 Expected Thickness: ~10 µm Recipe (Time, Speed, Acceleration): 1 | 5 s, 350 RPM, 1500 RPM/s 2 | 3 s, 0 RPM, 1000 RPM/s

				3 | 5 s, 350 RPM, 2000 RPM/s 4 | 30 s, 1800 RPM, 2000 RPM/s
48	*BAKE RESIST*	*FR*	HOTPLATE	110°C, 170 seconds
49	*REHYDRATE*	*FR*	NONE	Rehydrate resist layer for > 30 min
50	*EXPOSE*	*FR*	ABM-ALIGNER	MASK4-Electrodes Intensity: ~20 mW/cm^2 Time: 63 seconds
51	*DEVELOP*	*FR*	BATH5-DEVELOP	AZ400K:DI Water (1:4), 5 minutes
52	*DESCUM*	*FR*	VISION-RIE	Pressure: 75 mTorr RF Power: 30 W O_2: 50 sccm Time: 2 minutes
53	*INSPECT*	*FR*	NIKON	Optical microscopy
54	*EVAPORATE*	*FR*	EVAP-1	Recipe (Metal, Thickness, Rate): 1 | Chrome, 10 nm, 1 Å/s 2 | Nickel, 100 nm, 3 Å/s 3 | Gold, 200 nm, 3 Å/s
55	*LIFTOFF*	*FR*	BATH6-STRIP	Liftoff in acetone soak, rinse with acetone, IPA, and water *Could obtain cleaner edges with bi-layer resist stack.*
56	*CLEAN*	*FR*	BARREL-ETCH	Power: 100 W Time: 5 minutes
57	*INSPECT*	*FR*	NIKON	Optical microscopy

58	*TREATMENT*		HMDS-OVEN	Standard HMDS treatment
59	*SPIN RESIST*	*FR*	SPIN1|2-AUTO	Resist: AZ9260 Expected Thickness: ~7 µm Recipe (Time, Speed, Acceleration): 1 | 5 s, 350 RPM, 1500 RPM/s 2 | 3 s, 0 RPM, 1000 RPM/s 3 | 5 s, 350 RPM, 2000 RPM/s 4 | 30 s, 2300 RPM, 2000 RPM/s
60	*BAKE RESIST*	*FR*	HOTPLATE	110°C, 180 seconds
61	*REHYDRATE*	*FR*	NONE	Rehydrate resist layer for > 30 min
62	*EXPOSE*	*FR*	ABM-ALIGNER	MASK4-Channel Intensity: ~20 mW/cm^2 Time: 65 seconds
63	*DEVELOP*	*FR*	BATH5-DEVELOP	AZ400K:DI Water (1:4), 6 minutes
64	*INSPECT*	*FR*	NIKON	Optical microscopy
65	*OXIDE UNDERCUT*	*FR*	BATH3-HF	49% HF for 1.5 minutes
66	*DESCUM*	*FR*	VISION-RIE	Pressure: 75 mTorr RF Power: 30 W O_2: 50 sccm Time: 3 minutes
67	*MEASURE*	*FR*	WYKO	Interferometric profilometry for resist thickness ($z_{Channel}$)

68	*PROTECT*	*BK*	NONE	Wafer tape on backside
69	*DEPOSIT*	*FR*	PARYLENE	Deposition rate: ~0.55 µm/g Amount: 10 g Expected thickness: ~5.5 µm
70	*CLEAN*	*BK*	NONE	Remove tape from backside
71	*DEPOSIT*	*FR*	EVAP-1	Recipe (Metal, Thickness, Rate): 1 | Aluminum, 150 nm, 3 Å/s
72	*CLEAN*	*FR*	NONE	Remove parylene around edges with razor blade
73	*SPIN RESIST*	*FR*	SPIN1|2-AUTO	Resist: AZ9260 Recipe (Time, Speed, Acceleration): 1 | 5 s, 350 RPM, 1500 RPM/s 2 | 3 s, 0 RPM, 1000 RPM/s 3 | 5 s, 350 RPM, 2000 RPM/s 4 | 30 s, 1800 RPM, 2000 RPM/s
74	*BAKE RESIST*	*FR*	HOTPLATE	110°C, 80 seconds
75	*COOL*	*FR*	NONE	Cool resist layer for > 1 min
76	*SPIN RESIST*	*FR*	SPIN1|2-AUTO	Resist: AZ9260 Expected Final Thickness: ~30 µm Recipe (Time, Speed, Acceleration): 1 | 5 s, 350 RPM, 1500 RPM/s 2 | 3 s, 0 RPM, 1000 RPM/s 3 | 5 s, 350 RPM, 2000 RPM/s 4 | 30 s, 1800 RPM, 2000 RPM/s
77	*BAKE RESIST*	*FR*	HOTPLATE	110°C, 180 seconds

78	*REHYDRATE RESIST*	*FR*	NONE	Rehydrate resist overnight
79	*EXPOSE*	*FR*	ABM-ALIGNER	MASK5-Parylene Intensity: ~20 mW/cm^2 Time: 46.5 seconds
80	*REST RESIST*	*FR*	ABM-ALIGNER	Let resist rest for > 1 minute
81	*EXPOSE*	*FR*	ABM-ALIGNER	MASK5-Parylene Intensity: ~20 mW/cm^2 Time: 46.5 seconds
82	*DEVELOP*	*FR*	BATH5-DEVELOP	AZ400K:DI Water (1:4), 8 minutes (may require agitation or longer time to fully dissolve exposed aluminum layer)
83	*INSPECT*	*FR*	NIKON	Optical microscopy (green filter)
84	*REST RESIST*	*FR*	NONE	Rest resist > 24 hrs. in white light
85	*ETCH Parylene*	*FR*	ICP-FL	Temp: 0°C Pressure: 10 mTorr RF Forward: 35 W ICP Forward: 2000 W O_2: 30 sccm N_2: 10 sccm He flow: ~6 sccm Time: 5 minutes Etch rate: ~1.1 µm/s Resist etch rate: ~1 µm/s *Etch until exposed parylene removed.*
86	*CLEAN*	*BK*	BATH6-STRIP	Remove remaining resist with acetone, and rinse with IPA/water

87	*INSPECT*	*FR*	NIKON	Optical microscopy
88	*MEASURE*	*FR*	WYKO	Interferometric profilometry for parylene thickness ($z_{Parylene}$)
89	*RELEASE*	*FR*	BATH3-HF	49% HF for 15 minutes to release structure Undercut Depth: ~28 µm
90	*SOLVENT DRY*	*FR*	BATH6-STRIP	To avoid stiction from water surface tension, first submerge in water then directly transfer into IPA for 10 minute soak. After IPA, allow device to dry in air.
91	*EVAPORATE*	*FR*	EVAP-1	MASK6-Shadow Electrodes Recipe (Metal, Thickness, Rate): 1 | Chrome, 10 nm, 1 Å/s 2 | Gold, 200 nm, 3 Å/s
92	*CHANNEL RELEASE*	*FR*	BATH6-STRIP	Long acetone soak (> 30 hours)
93	*INSPECT*	*FR*	NIKON	Optical microscopy
94	*PROTECT*	*FR*	COVER	Invert wafer and protect frontside with cover/tape
95	*DEPOSIT*	*BK*	PARYLENE	Deposition rate: ~0.55 µm/g Amount: 2 g Expected thickness: ~1.1 µm *Parylene coats inner channel.*
96	*CLEAN*	*BK*	RAZOR	Remove cover, tape, and loose parylene

97	*DICE*		SCRIBE	Dice wafer into chips
98	*PROTECT*	*FR*	EPOXY	Use epoxy adhesive to protect undercut edge
	PROCESS COMPLETE			

Appendix B: Detailed Frontside Process Flow

	Cleaning Step
	Lithography Step
	Metrology Step
	Key Step

Sequence	Step	Side	Equipment	Parameters/Notes
0	*START*		WAFER	Wafer Diameter: 100 mm Device Thickness: 2 µm BOX Thickness: 5 µm Handle Thickness: 350 µm
1	*CLEAN*		BATH2-RCA	10 min. in SC-1 and 10 min. in SC-2
2	*TREATMENT*		HMDS-OVEN	Standard HMDS treatment
3	*SPIN RESIST*	*FR*	SPIN1|2-AUTO	Resist: AZ1512 Expected Thickness: ~1.1 µm Recipe (Time, Speed, Acceleration): 1 | 2 s, 500 RPM, 4000 RPM/s 2 | 30 s, 4000 RPM, 4000 RPM/s
4	*BAKE RESIST*	*FR*	HOTPLATE	110°C, 90 seconds
5	*EXPOSE*	*FR*	ABM-ALIGNER	MASK1-PhC (includes alignment) Intensity: ~20 mW/cm^2 Time: 3.1 seconds

6	*DEVELOP*	*FR*	BATH5-DEVELOP	AZ340:DI Water (1:4), 50 seconds
7	*INSPECT*	*FR*	NIKON	Optical microscopy
8	*MEASURE*	*FR*	ALPHA STEP	Measure step height of AZ1512
9↓	*ETCH Si PhC*	*FR*	ICP-FL	Temp: 20°C Pressure: 15 mTorr RF Forward: 30 W ICP Forward: 1200 W SF_6: 25 sccm C_4F_8: 19 sccm He flow: ~11 sccm Time: 25 seconds Etch rate: ~18 nm/s Resist etch rate: ~ 3 nm/s Etch depth: ~350 nm. *To create photonic crystal.*
10	*ETCH CALIBRATION*	*FR*	ALPHA STEP	*For combined resist + Si etch.*
↻	*ETCH Si PhC*	*FR*	*ICP-FL*	Repeat **Steps 9–10** if required
11	*RESIST STRIP*	*FR*	EKC	Strip in EKC for 5 minutes
12	*CLEAN*	*FR*	BARREL-ETCH	Power: 125 W Time: 5 minutes
13	*INSPECT*	*FR*	NIKON	Optical microscopy (green filter)
14	*ETCH CALIBRATION*	*FR*	ALPHA STEP	For final depth of the PhC (z_{PhC})

15	*TREATMENT*		HMDS-OVEN	Standard HMDS treatment
16	*SPIN RESIST*	*FR*	SPIN1|2-AUTO	Resist: AZ1512 Expected Thickness: ~1.1 µm Recipe (Time, Speed, Acceleration): 1 | 2 s, 500 RPM, 4000 RPM/s 2 | 30 s, 4000 RPM, 4000 RPM/s
17	*BAKE RESIST*	*FR*	HOTPLATE	110°C, 90 seconds
18	*EXPOSE*	*FR*	ABM-ALIGNER	MASK2-Beam Intensity: ~20 mW/cm^2 Time: 3.1 seconds
19	*DEVELOP*	*FR*	BATH5-DEVELOP	AZ340:DI Water (1:4), 50 seconds
20	*INSPECT*	*FR*	NIKON	Optical microscopy (green filter)
21	*DESCUM*	*FR*	VISION-RIE	Pressure: 75 mTorr RF Power: 30 W O_2: 50 sccm Time: 1 minute
22	*ETCH Si Beam*	*FR*	VISION-RIE	Pressure: 60 mTorr RF Power: 120 W SF_6: 20 sccm CHF_3: 8 sccm Time: 8.5 minutes Etch rate: ~300 nm/min. *Etch until silicon cleared and oxide visible.*
23	*RESIST STRIP*	*FR*	EKC	Strip in EKC for 5 minutes

24	*CLEAN*	*FR*	BARREL-ETCH	Power: 125 W Time: 5 minutes
25	*INSPECT*	*FR*	NIKON	Optical microscopy
26	*MEASURE*	*FR*	ALPHA STEP	For final beam thickness (z_{Beam})
39	*TREATMENT*		HMDS-OVEN	Standard HMDS treatment
40	*SPIN RESIST*	*FR*	SPIN1|2-AUTO	Resist: AZ9260 Expected Thickness: ~7 µm Recipe (Time, Speed, Acceleration): 1 | 5 s, 350 RPM, 1500 RPM/s 2 | 3 s, 0 RPM, 1000 RPM/s 3 | 5 s, 350 RPM, 2000 RPM/s 4 | 30 s, 2300 RPM, 2000 RPM/s
41	*BAKE RESIST*	*FR*	HOTPLATE	110°C, 170 seconds
42	*REHYDRATE*	*FR*	NONE	Rehydrate resist layer for > 30 min
43	*EXPOSE*	*FR*	ABM-ALIGNER	MASK3-Channel Intensity: ~20 mW/cm^2 Time: 65 seconds
44	*DEVELOP*	*FR*	BATH5-DEVELOP	AZ400K:DI Water (1:4), 5 minutes
45	*INSPECT*	*FR*	NIKON	Optical microscopy
46	*OXIDE UNDERCUT*	*FR*	BATH3-HF	49% HF for 1.5 minutes

47	*DESCUM*	*FR*	VISION-RIE	Pressure: 75 mTorr RF Power: 30 W O_2: 50 sccm Time: 3 minutes
48	*MEASURE*	*FR*	WYKO	Interferometric profilometry for resist thickness ($z_{Channel}$)
49	*PROTECT*	*BK*	NONE	Wafer tape on backside
50	*DEPOSIT*	*FR*	PARYLENE	Deposition rate: ~0.55 µm/g Amount: 10 g Expected thickness: ~5.5 µm
51	*CLEAN*	*BK*	NONE	Remove tape from backside
52	*DEPOSIT*	*FR*	EVAP-1	Recipe (Metal, Thickness, Rate): 1 | Aluminum, 150 nm, 3 Å/s
53	*SPIN RESIST*	*FR*	SPIN1|2-AUTO	Resist: AZ9260 Recipe (Time, Speed, Acceleration): 1 | 5 s, 350 RPM, 1500 RPM/s 2 | 3 s, 0 RPM, 1000 RPM/s 3 | 5 s, 350 RPM, 2000 RPM/s 4 | 30 s, 1800 RPM, 2000 RPM/s
54	*BAKE RESIST*	*FR*	HOTPLATE	110°C, 80 seconds
55	*COOL*	*FR*	NONE	Cool resist layer for > 1 min
56	*SPIN RESIST*	*FR*	SPIN1|2-AUTO	Resist: AZ9260 Expected Final Thickness: ~30 µm Recipe (Time, Speed, Acceleration): 1 | 5 s, 350 RPM, 1500 RPM/s 2 | 3 s, 0 RPM, 1000 RPM/s 3 | 5 s, 350 RPM, 2000 RPM/s

				4 | 30 s, 1800 RPM, 2000 RPM/s
57	*BAKE RESIST*	*FR*	HOTPLATE	110°C, 160 seconds
58	*REHYDRATE RESIST*	*FR*	NONE	Rehydrate resist overnight
59	*EXPOSE*	*FR*	ABM-ALIGNER	MASK4-Parylene Intensity: ~20 mW/cm^2 Time: 93 seconds
60	*DEVELOP*	*FR*	BATH5-DEVELOP	AZ400K:DI Water (1:4), 8 minutes (may require agitation to fully dissolve exposed aluminum layer)
61	*INSPECT*	*FR*	NIKON	Optical microscopy
62	*ETCH Parylene*	*FR*	ICP-FL	Temp: 0°C Pressure: 10 mTorr RF Forward: 35 W ICP Forward: 2000 W O_2: 30 sccm N_2: 10 sccm He flow: ~11 sccm Time: 5 minutes Etch rate: ~1.1 µm/s Resist etch rate: ~1 µm/s *Etch until exposed parylene removed.*
63	*CLEAN*	*BK*	BATH6-STRIP	Remove remaining resist with acetone, and rinse with IPA/water
64	*INSPECT*	*FR*	NIKON	Optical microscopy

65	*MEASURE*	*FR*	WYKO	Interferometric profilometry for parylene thickness ($z_{Parylene}$)
66	*RELEASE*	*FR*	BATH3-HF	49% HF for 25 minutes to release structure
67	*SOLVENT DRY*	*FR*	BATH6-STRIP	To avoid stiction from water surface tension, first submerge in water then directly transfer into IPA for a 10-minute soak. After IPA, allow device to dry in air.
	EVAPORATE	*FR*	EVAP-1	MASK5-Shadow Electrodes Recipe (Metal, Thickness, Rate): 1 | Chrome, 10 nm, 1 Å/s 2 | Gold, 200 nm, 3 Å/s
	EVAPORATE	*BK*	EVAP-1	Recipe (Metal, Thickness, Rate): 1 | Aluminum, 250 nm, 3 Å/s
68	*CHANNEL RELEASE*	*FR*	BATH6-STRIP	Long acetone soak (> 30 hours)
69	*INSPECT*	*FR*	NIKON	Optical microscopy
70	*DICE*		SCRIBE	Dice wafer into chips
71	*PROTECT*	*FR*	EPOXY	Use epoxy adhesive to protect undercut edge
	PROCESS COMPLETE			

Appendix C: Detection and Feedback Circuit Overview

The signal is first detected by the photodiode (shown as an equivalent circuit model) and converted to a voltage by a transimpedance amplifier. This signal is further amplified and filtered by a bandpass filter.

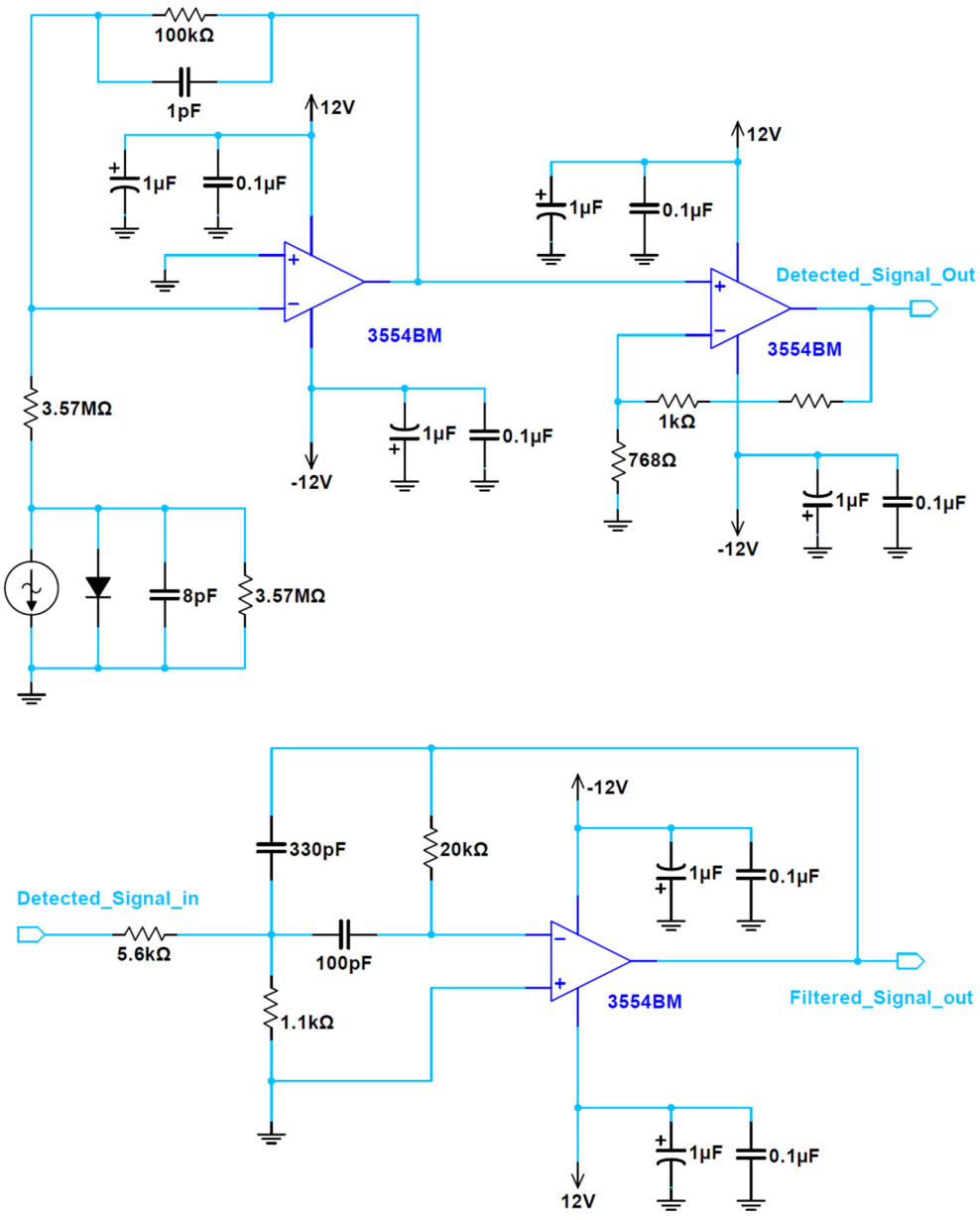

After filtering noise, the signal is amplified to the required level for feedback and frequency detection. The amplification is fixed, but can be adjusted using the indicated potentiometer. This level is converted to a RMS-DC voltage by an analog IC.

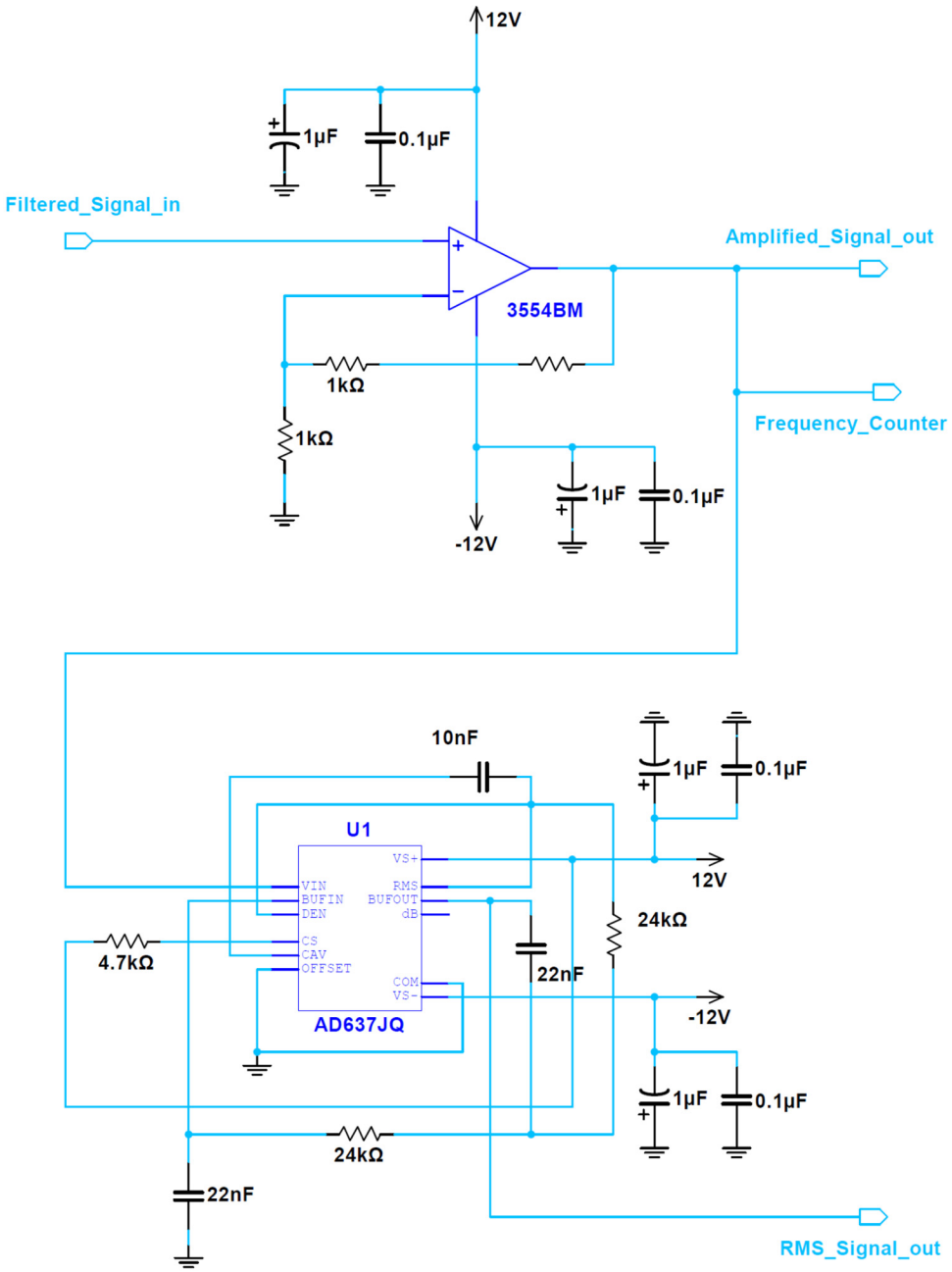

The RMS voltage is amplified and split into two paths: one to an analog-to-digital converter for data acquisition and the other for comparison to the drive amplitude set point through a difference amplifier. The ADC signal is amplified to better utilize dynamic range and limited for digital input protection.

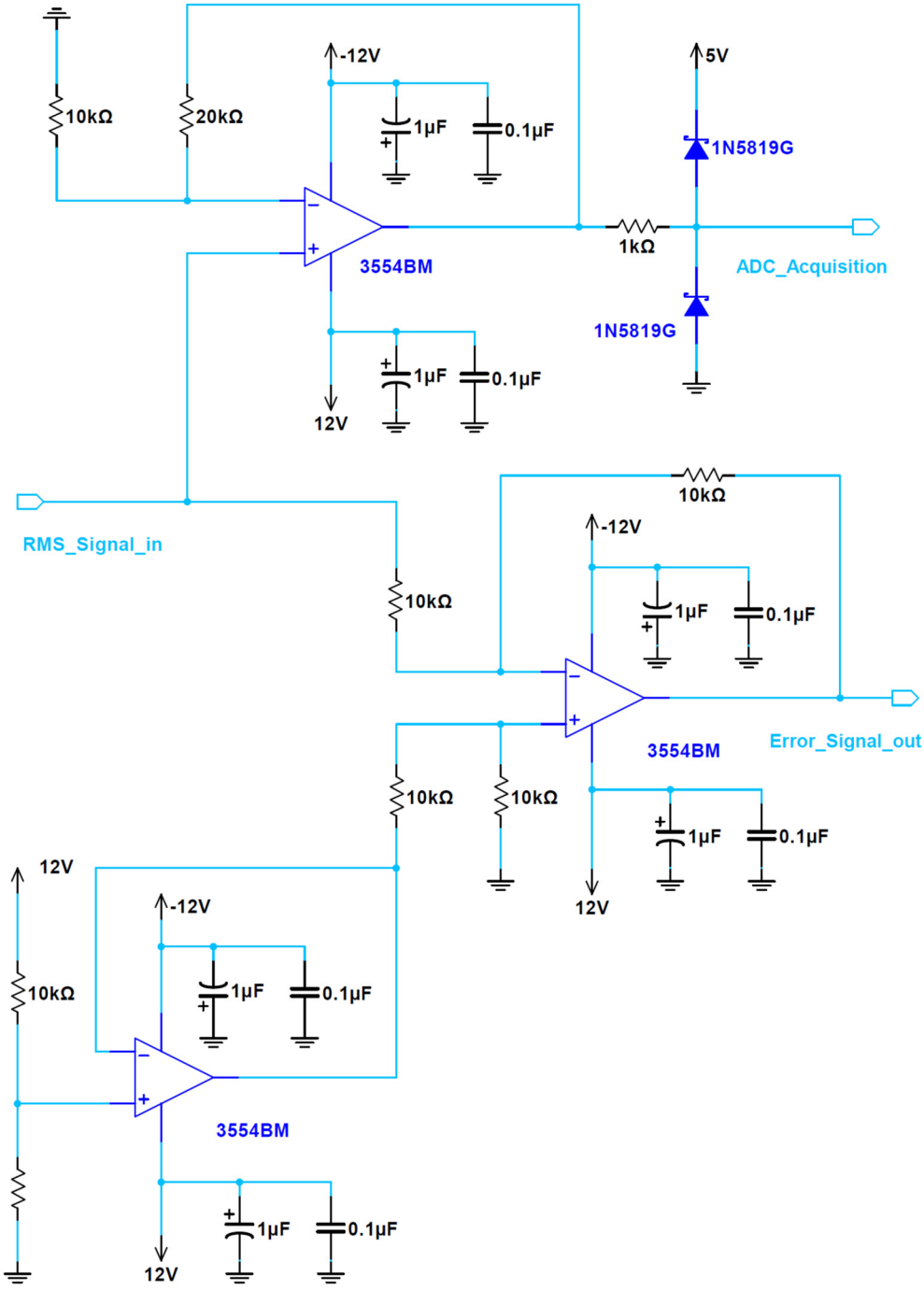

Error arising from the difference amplifier feeds three amplifier stages to produce proportional (P), integral (I), and difference (D) terms that are summed together to produce an output control signal, with required limiting.

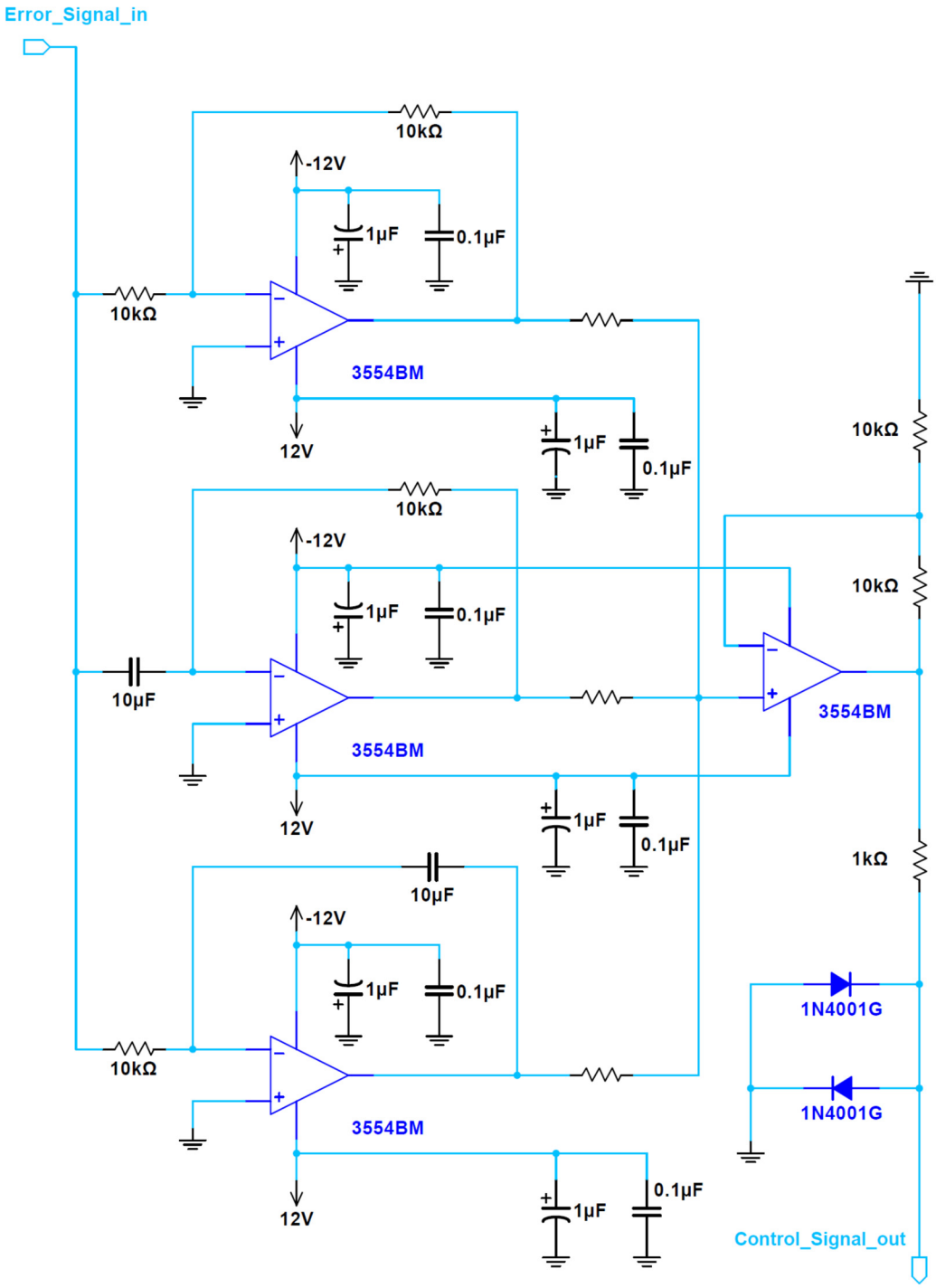

The amplified signal passes through an all-pass filter, which imparts the necessary phase shift for feedback and can be tuned with a potentiometer. The final conditioned signal is amplified by a voltage-controlled amplifier (thereby implementing the PID control signal) and added to the device bias voltage. For direct-drive measurements, an AC waveform can be injected to characterize frequency response.

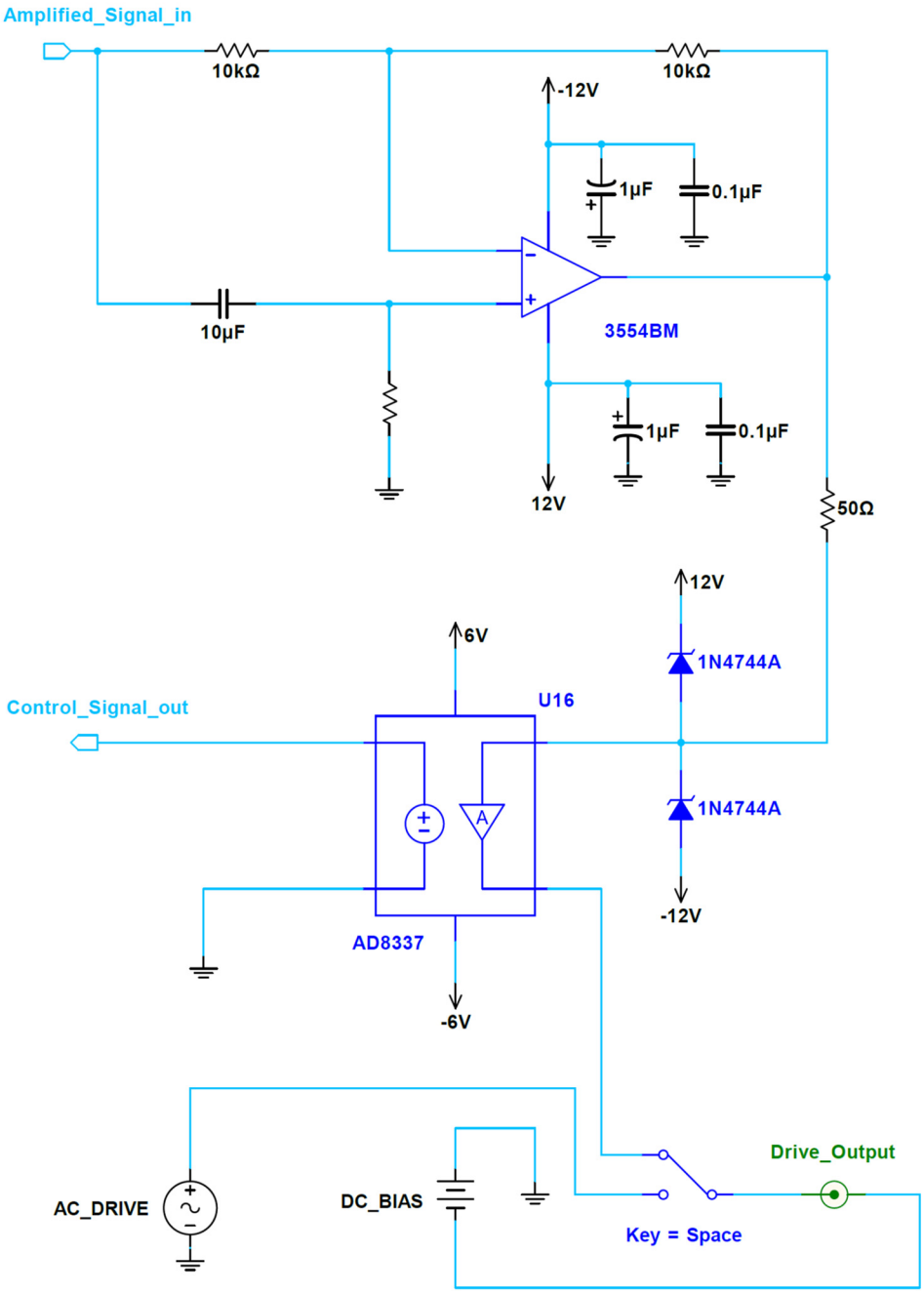

Appendix D: Setup Control and Data Acquisition Software

```
using System;
using System.ComponentModel;
using System.Windows.Forms;
using OxyPlot;
using OxyPlot.Axes;
using OxyPlot.Series;

namespace SetupControl
{
    // This is the main form for application control and measurement.
    public partial class MainForm : Form
    {
        // This form allows two types of measurements: sweep and monitor.
        // Sweep measurements sweep frequency and obtain the fitted amplitude
        // response, while monitor records the resonant frequency in real
        // time using feedback in the set-up.

        // Sweep measurement frequencies and data.
        Double[][] measuredData;
        Double[] measuredFreq;

        // Create sweep file on next measure.
        static bool createSweepFile = false;

        // Form components.
        GrayOut backForm;
        System.Drawing.Color tbForeColor;
        System.Drawing.Color tbReadOnly;
        System.Drawing.Color tbEnabled;

        // Sweep plot elements.
        PlotModel myModelSweep; // model handle
        Axis horizontalSweep; // horizontal axis
        Axis verticalSweep; // vertical axis
        Series[] seriesSweep; // data series
        int maxSeries = 12; // maximum number of sweeps (maxSeries / 2)
        int currentSeries = 0; // current measurement series
        Double minFrequency, maxFrequency;
        Double frequencyAxisClearance = 0.5; // fit curve/labels
        // Color array for series data. Optimally the number of colors should
        // match(maxSeries / 2).
        OxyColor[] plotColorSweep = new OxyColor[] {
            OxyColors.Blue,
            OxyColors.Purple,
            OxyColors.Green,
            OxyColors.Red,
            OxyColors.Orange,
            OxyColors.Black
        };
```

```
// Monitor (resonant frequency) plot elements.
PlotModel myModelMonitor; // model handle
Axis horizontalMonitor; // horizontal axis
Axis verticalMonitor; // vertical axis
LineSeries seriesMonitor; // monitor data Series

// Measurement button fade control (indicates measurement).
static System.Windows.Forms.Timer statusTimer;
int steps = 20; // # of fade steps
int step; // fade step
static int fadeStatus = 0; // current fade level

// Initialize the main Form.
public MainForm()
{
    InitializeComponent();

    // Open the GrayOut form to dedicate system resources
    // to measurement.
    backForm = new GrayOut();
    backForm.Show();

    // Collect form drawing colors for reference.
    tbForeColor = System.Drawing.Color.FromArgb(255, 70, 130, 180);
    tbReadOnly = System.Drawing.Color.FromArgb(255, 220, 220, 220);
    tbEnabled = tb_Amp.BackColor;
    UpdateTextBoxStyles();

    // Create a background worker to handle measurement/processing.
    BackgroundWorker.DoWork += new DoWorkEventHandler(bw_DoWork);
    BackgroundWorker.WorkerSupportsCancellation = true;

    // Obtain the configuation from file.
    Configuration.LoadConfiguration();

    // Initialize the measurement instruments.
    Generator.Initialize();
    Acquisition.Initialize();
    Counter.Initialize();

    // Enable measurement if initialization is successful.
    EnableMeasurement();

    // Display/set the saved measurement parameters.
    tb_Amp.Text = Configuration.Amplitude.ToString();
    tb_FStart.Text = Configuration.StartFrequency.ToString();
    tb_FStep.Text = Configuration.StepFrequency.ToString();
    tb_FEnd.Text = Configuration.EndFrequency.ToString();
    tb_Drift.Text = Configuration.DriftFactor.ToString();
    tb_IntervalMonitor.Text =
        Configuration.MonitorInterval.ToString();
```

```
if (Configuration.Continuous)
    btn_Continuous.BackColor = System.Drawing.Color.Thistle;

if (Configuration.SaveSweep)
{
    btn_SaveSweep.BackColor = System.Drawing.Color.Thistle;
    // Create new sweep file on measure.
    createSweepFile = true;
}

if (Configuration.Overlay)
    btn_Overlay.BackColor = System.Drawing.Color.Thistle;

if (Configuration.SaveMonitor)
    btn_SaveMonitor.BackColor = System.Drawing.Color.Thistle;

// Initialize data fields.
for (int i = 0; i < maxSeries; i += 2)
{
    listBox.Items.Add("{ }");
}
tb_Stats.Text = "[ ]";
measuredFreq = new Double[maxSeries / 2];

// Create measure button fade Timer.
statusTimer = new System.Windows.Forms.Timer();
statusTimer.Tick += new EventHandler(TimerEventProcessor);
statusTimer.Interval = 50;
step =
    (int)(255.0 / (Double)steps); // Calculate number of steps.

// Create the sweep plot.
myModelSweep = new PlotModel { Title = "Frequency Response" };
horizontalSweep = new LinearAxis();
verticalSweep = new LinearAxis();
horizontalSweep.Position = AxisPosition.Bottom;
verticalSweep.Position = AxisPosition.Left;
horizontalSweep.Title = "Frequency (kHz)";
verticalSweep.Title = "Magnitude";
myModelSweep.Axes.Add(horizontalSweep);
myModelSweep.Axes.Add(verticalSweep);
myModelSweep.PlotAreaBackground =
    OxyPlot.OxyColor.FromRgb(255, 255, 255);
plotViewSweep.Model = myModelSweep;
// Create array of data series, and assign each a type and color.
seriesSweep = new Series[maxSeries];
int colorIndex = 0;
for (int i = 0; i < maxSeries; i++)
{
    // Scatter series represent measurement data.
    ScatterSeries scatter = new ScatterSeries { MarkerFill =
        plotColorSweep[colorIndex] };
    scatter.MarkerSize = 3;
    scatter.MarkerType = MarkerType.Circle;
```

```
            seriesSweep[i] = scatter;
            myModelSweep.Series.Add(seriesSweep[i]);
            i++;

            // Line series represent fit data.
            LineSeries line = new LineSeries();
            line.Color = plotColorSweep[colorIndex];
            seriesSweep[i] = line;
            myModelSweep.Series.Add(seriesSweep[i]);

            // Increment color for next series (or loop to start).
            colorIndex++;
            if (colorIndex >= plotColorSweep.Length) colorIndex = 0;
        }

        // Set minimum and maximum plot frequencies.
        maxFrequency = 0.0;
        minFrequency = Double.MaxValue;

        // Create the monitor plot.
        myModelMonitor =
            new PlotModel { Title = "Resonant Frequency Time Series" };
        horizontalMonitor = new LinearAxis();
        verticalMonitor = new LinearAxis();
        verticalMonitor.LabelFormatter = _formatter;
        horizontalMonitor.Position = AxisPosition.Bottom;
        verticalMonitor.Position = AxisPosition.Left;
        horizontalMonitor.Title = "Time (s)";
        verticalMonitor.Title = "Frequency (Hz)";
        myModelMonitor.Axes.Add(horizontalMonitor);
        myModelMonitor.Axes.Add(verticalMonitor);
        myModelMonitor.PlotAreaBackground =
            OxyPlot.OxyColor.FromRgb(255, 255, 255);
        plotViewMonitor.Model = myModelMonitor;
        seriesMonitor = new LineSeries();
        myModelMonitor.Series.Add(seriesMonitor);
    }

    //
    // MEASUREMENT AND PLOTTING METHODS
    //

    // Event handler for fading the measurement button.
    private static void TimerEventProcessor(
        Object myObject, EventArgs myEventArgs)
    {
        statusTimer.Stop();
        Program.MainHandle.FadeMeasureButton();

        // Check that a measurement is still ocurring.
        if (Program.MainHandle.BackgroundWorker.IsBusy)
            statusTimer.Enabled = true;
        else Program.MainHandle.SetMeasureFade(false);
    }
```

```
// Update the sweep plot with new data.
public bool ReportDataSweep(Double x, Double y)
{
    // Adjust frequency range if necessary.
    if (x > maxFrequency) maxFrequency = x + frequencyAxisClearance;
    if (x < minFrequency) minFrequency = x - frequencyAxisClearance;
    horizontalSweep.Minimum = minFrequency;
    horizontalSweep.Maximum = maxFrequency;

    // Add new point to current data series.
    ScatterSeries scatter =
        seriesSweep[currentSeries] as ScatterSeries;
    scatter.Points.Add(new ScatterPoint(x, y));

    // Update the GUI.
    if (plotViewSweep.InvokeRequired)
    {
        plotViewSweep.Invoke(new MethodInvoker(() =>
        {
            plotViewSweep.InvalidatePlot(true);
        }));
    }
    else
    {
        plotViewSweep.InvalidatePlot(true);
    }
    // Return the state of measurement operation.
    return BackgroundWorker.CancellationPending;
}

// Update the monitor plot with new data.
public bool ReportDataMonitor(Double x, Double y)
{
    // Add the new data point to the series.
    seriesMonitor.Points.Add(new DataPoint(x, y));

    // Update the GUI.
    if (plotViewMonitor.InvokeRequired)
    {
        plotViewMonitor.Invoke(new MethodInvoker(() =>
        {
            plotViewMonitor.InvalidatePlot(true);
        }));
    }
    else
    {
        plotViewMonitor.InvalidatePlot(true);
    }
    // Return the state of measurement operation.
    return BackgroundWorker.CancellationPending;
}
```

```
// Calculate specific statistics for input data
// (average, standard deviation, standard error).
private Double[] CalculateStatistics(Double[] values_in)
{
    // Count the number of non-zero values.
    int count = 0;
    for (int i = 0; i < values_in.Length; i++)
        if (values_in[i] > 0) count++;

    // Create a new Array without zero values.
    Double[] values = new Double[count];
    int k = 0;
    for (int i = 0; i < values_in.Length; i++)
    {
        if (values_in[i] > 0)
        {
            values[k] = values_in[i];
            k++;
        }
    }

    // Calculate the statistical values.
    Double[] results = new Double[3];
    if (values.Length > 0)
    {
        Double average = 0;
        for (int i = 0; i < values.Length; i++) average += values[i];
        results[0] = average / values.Length; // average

        Double deviation = 0;
        for (int i = 0; i < values.Length; i++)
            deviation += Math.Pow(values[i] - results[0], 2);

        // standard deviation
        results[1] =
           Math.Sqrt(deviation / values.Length);
        // standard error
        results[2] = results[1] / Math.Sqrt(values.Length);
    }
    // Return results array.
    return results;
}

// Process and plot data from a completed measurement sweep.
public void PlotData(Double[][] newData)
{
    // Check if data is valid and measurement isn't terminating.
    if (newData[0] != null &&
        !Program.MainHandle.BackgroundWorker.CancellationPending)
    {
        // Set the start frequency, and the end frequency will be
        // shifted by the data.
        Double startFreq = newData[0][0];
        Double endFreq = newData[0][0];
```

```
// Calculate the fit parameters and fit data.
Double[] fitParams = Processing.FitData(newData);
Double[][] fitData =
    Processing.EvaluateFunction(fitParams, newData);

// Update measured resonant frequency array.
measuredFreq[currentSeries / 2] = fitParams[0];

// Clear measurement/fit curves and populate with final data.
ScatterSeries scatter =
    seriesSweep[currentSeries] as ScatterSeries;
LineSeries line =
    seriesSweep[currentSeries + 1] as LineSeries;
scatter.Points.Clear();
line.Points.Clear();
for (int i = 0; i < newData.Length; i++)
{
    if (newData[i] != null)
    {
        scatter.Points.Add(
            new ScatterPoint(newData[i][0], newData[i][1]));
        endFreq = newData[i][0];
    }
    else break;
}

for (int i = 0; i < fitData.Length; i++)
{
    if (fitData[i] != null)
    {
        line.Points.Add(
            new DataPoint(fitData[i][0], fitData[i][1]));
    }
    else break;
}

// Set final axis ranges + clearance.
if (endFreq > maxFrequency)
    maxFrequency = endFreq + frequencyAxisClearance;
if (startFreq < minFrequency)
    minFrequency = startFreq - frequencyAxisClearance;
horizontalSweep.Minimum = minFrequency;
horizontalSweep.Maximum = maxFrequency;

// Obtain measurement information fields.
String bias = "", description = "", amplitude = "";
if(tb_SweepBias.InvokeRequired)
{
    tb_SweepBias.Invoke(new MethodInvoker(() =>
    {
        bias = tb_SweepBias.Text;
        description = tb_SweepDescription.Text;
        amplitude = tb_Amp.Text;
    }));
```

```
            }
            else
            {
                bias = tb_SweepBias.Text;
                description = tb_SweepDescription.Text;
                amplitude = tb_Amp.Text;
            }
            // If save enabled, save data/information to file.
            if (Configuration.SaveSweep)
                Files.ExportSweepData(newData, fitParams, description,
                    amplitude, bias);

            // Calculate and display statistics values, and update plot.
            Double[] stats = CalculateStatistics(measuredFreq);
            String statsStr = "[ " + String.Format("{0:N3}", stats[0]) +
                ", " + String.Format("{0:N3}", stats[1]) + ", " +
                String.Format("{0:N3}", stats[2]) + " ]";
            String dataStr = "{ " + String.Format("{0:N2}", fitParams[0])
                + ", " + String.Format("{0:N0}", fitParams[1]) + ", " +
                String.Format("{0:N0}", fitParams[3] * 100) + "}";
            if (plotViewSweep.InvokeRequired)
            {
                plotViewSweep.Invoke(new MethodInvoker(() =>
                {
                    listBox.Items[currentSeries / 2] = dataStr;
                    tb_Stats.Text = statsStr;
                    plotViewSweep.InvalidatePlot(true);
                }));
            }
            else
            {
                listBox.Items[currentSeries / 2] = dataStr;
                tb_Stats.Text = statsStr;
                plotViewSweep.InvalidatePlot(true);
            }
        }
    }

    // Conduct a sweep measurement.
    private void MeasureSweep(String[] arguments)
    {
        do
        {
            // Clear statistics/data from previous measurement.
            listBox.Invoke(new MethodInvoker(() =>
            {
                listBox.Items[currentSeries / 2] = "{ }";
            }));
            ScatterSeries scatter =
                seriesSweep[currentSeries] as ScatterSeries;
            scatter.Points.Clear();
            LineSeries line =
                seriesSweep[currentSeries + 1] as LineSeries;
            line.Points.Clear();
```

```
        // If overlay is set, clear the previous plot data.
        if (!Configuration.Overlay)
        {
            int previous = currentSeries - 2;
            if (previous < 0) previous = maxSeries - 2;

            ScatterSeries scatterPrev =
                seriesSweep[previous] as ScatterSeries;
            scatterPrev.Points.Clear();
            LineSeries linePrev =
                seriesSweep[previous + 1] as LineSeries;
            linePrev.Points.Clear();
        }

        // Perform a measurement and plot the data.
        measuredData = SweepMeasurement.Measure(arguments);
        PlotData(measuredData);

        // Check if the measurement has been cancelled.
        if (!BackgroundWorker.CancellationPending)
        {
            // Check if measurement is continuous and a measurement
            // delay is set.
            if (Configuration.Continuous &&
                Configuration.MeasurementDelay > 0)
            {
                // Play sound to indicate sweep completion.
                WMPLib.WindowsMediaPlayer wplayer =
                    new WMPLib.WindowsMediaPlayer();
                wplayer.URL = "tone.mp3";
                wplayer.controls.play();

                // Set generator to resonant frequency
                // for user intervention.
                String f = String.Format("{0:F0}",
                    measuredFreq[currentSeries / 2]);
                Generator.SetFrequency(f);

                // Wait for set delay time.
                System.Threading.Thread.Sleep(
                    Configuration.MeasurementDelay * 1000);

                // Indicate measurement delay has ended.
                wplayer.controls.play();
            }
            // Increment to the next data series.
            currentSeries += 2;
            if (currentSeries >= maxSeries)
                currentSeries = 0;
        }
        else break;
    } while (Configuration.Continuous);
```

```
    // Report that the measurement has ended.
    ReportMeasurementEnd(true);
}

// Conduct a real-time resonant frequency measurement.
private void MeasureMonitor(String[] arguments)
{
    // Create data arrays with an initialize size.
    Double[] time = new Double[100];
    Double[] frequency = new Double[100];

    // Record start time and obtain sampling interval.
    DateTime start = DateTime.Now;
    int interval = Int32.Parse(arguments[0]);

    int i = 0;
    while (!BackgroundWorker.CancellationPending)
    {
        // This measurement continues until cancelled by an error or
        // the user.

        // Record lapsed time and obtain counter measurement.
        time[i] = DateTime.Now.Subtract(start).TotalSeconds;
        frequency[i] = Counter.ReadFrequency() * 1000;

        // Report new frequency data to plot.
        ReportDataMonitor(time[i], frequency[i]);

        // Export the new data to file if save enabled.
        if (Configuration.SaveMonitor)
            Files.ExportMonitorData(time[i], frequency[i]);

        // Check if data arrays are full, and double size if
        // necessary.
        i++;
        if (i >= time.Length)
        {
            Double[] newTime = new Double[time.Length * 2];
            Double[] newFrequency = new Double[frequency.Length * 2];

            Array.Copy(time, newTime, time.Length);
            Array.Copy(frequency, newFrequency, frequency.Length);

            time = newTime;
            frequency = newFrequency;
        }

        // Calculate the new running statistic.
        Double[] stats = CalculateStatistics(frequency);

        // Publish the current statistics to the user.
        tb_MonitorStats.Invoke(new MethodInvoker(() =>
            {
```

```
                tb_LastMonitor.Text = frequency[i - 1].ToString();
                tb_MonitorStats.Clear();
                tb_MonitorStats.AppendText("Average: " +
                    String.Format("{0:N3}", stats[0]));
                tb_MonitorStats.AppendText(Environment.NewLine);
                tb_MonitorStats.AppendText("Std. Deviation: " +
                    String.Format("{0:N3}", stats[1]));
                tb_MonitorStats.AppendText(Environment.NewLine);
                tb_MonitorStats.AppendText("Std. Error: " +
                    String.Format("{0:N3}", stats[2]));
            }));

        // Wait on delay interval between measurements.
        System.Threading.Thread.Sleep(interval);
    }

    // Report that the measurement has ended.
    ReportMeasurementEnd(true);
}

// Start measurement on the background workder thread.
private void bw_DoWork(Object sender, DoWorkEventArgs e)
{
    BackgroundWorker worker = (BackgroundWorker)sender;

    // Pass arguments along to either the sweep or monitor
    // measurement.
    String[] arguments = (String[])e.Argument;
    String[] argumentsNew = new String[arguments.Length - 1];
    Array.Copy(arguments, 1, argumentsNew, 0, arguments.Length - 1);
    if (arguments[0].Equals("sweep")) MeasureSweep(argumentsNew);
    else if (arguments[0].Equals("monitor"))
        MeasureMonitor(argumentsNew);
}

// Notify the user that the measurement has ended.
private void ReportMeasurementEnd(bool success)
{
    if(success)
    {
        // Create audible sound to inicate successful completion.
        WMPLib.WindowsMediaPlayer wplayer =
            new WMPLib.WindowsMediaPlayer();
        wplayer.URL = "sweep.mp3";
        wplayer.controls.play();

        // Stop measure button indicator.
        SetMeasureFade(false);
    }
}

//
// CONTROL AND INDICATOR METHODS
//
```

```
// Format labels to give adequate significant digits
// to resonant frequency.
private static String _formatter(Double d)
{
    return String.Format("{0:N3}", d);
}

// Update display styles when changing state.
private void UpdateTextBoxStyles()
{
    TextBox[] items = new TextBox[]
    {
        tb_Amp,
        tb_FStart,
        tb_FStep,
        tb_FEnd,
        tb_Drift
    };

    foreach (TextBox item in items)
    {
        if (item.ReadOnly)
        {
            item.BackColor = tbReadOnly;
        }
        else
        {
            item.BackColor = tbEnabled;
        }
        item.ForeColor = tbForeColor;
    }
}

// Enable or disable button and text controls.
private void EnableControls(bool enabled)
{
    // Sweep elements.
    btn_Config.Enabled = enabled;
    tb_Amp.ReadOnly = !enabled;
    tb_FStart.ReadOnly = !enabled;
    tb_FStep.ReadOnly = !enabled;
    tb_FEnd.ReadOnly = !enabled;
    btn_Continuous.Enabled = enabled;
    btn_SaveSweep.Enabled = enabled;
    btn_Overlay.Enabled = enabled;

    // Monitor elements.
    btn_ConfigMonitor.Enabled = enabled;
    tb_IntervalMonitor.ReadOnly = !enabled;
    btn_SaveMonitor.Enabled = enabled;

    // Update text boxes.
    UpdateTextBoxStyles();
}
```

```
// Activate/deactive measure button fading.
public void SetMeasureFade(bool state)
{
    if (state)
    {
        // Measurement underway, disable controls and start fade.
        fadeStatus = 0;
        step = step * -1;
        EnableControls(false);
        statusTimer.Start();
    }
    else
    {
        // Stop measure button fade, and enable controls.
        statusTimer.Stop();
        if (btn_MeasureSweep.InvokeRequired)
        {
            btn_MeasureSweep.Invoke(new MethodInvoker(() =>
            {
                btn_MeasureSweep.BackColor =
                    System.Drawing.SystemColors.Control;
                btn_MeasureMonitor.BackColor =
                    System.Drawing.SystemColors.Control;
                EnableControls(true);
            }));
        }
        else
        {
            btn_MeasureSweep.BackColor =
                System.Drawing.SystemColors.Control;
            btn_MeasureMonitor.BackColor =
                System.Drawing.SystemColors.Control;
            EnableControls(true);
        }
    }
}

// Toggle the measurement fade state.
private void ExecuteFade()
{
    // Set both monitor and sweep measurement buttons to current fade
    // level.
    btn_MeasureSweep.BackColor =
        System.Drawing.Color.FromArgb(fadeStatus, 30, 144, 255);
    btn_MeasureMonitor.BackColor =
        System.Drawing.Color.FromArgb(fadeStatus, 30, 144, 255);
    fadeStatus += step;

    // Determine the fade direction.
    if (fadeStatus >= 255) { step = step * -1; fadeStatus = 255; }
    else if (fadeStatus <= 0) { step = step * -1; fadeStatus = 0; }
}
```

```
// Method call for ExecuteFade that handles invoking.
private void FadeMeasureButton()
{
    if (btn_MeasureSweep.InvokeRequired)
    {
        btn_MeasureSweep.Invoke(new MethodInvoker(() =>
            ExecuteFade()));
    }
    else
    {
        ExecuteFade();
    }
}

//
// FORM METHODS FOR SWEEP MEASUREMENT
//

// Handle the sweep measurement button click.
private void MeasureSweep_Click(Object sender, EventArgs e)
{
    // Save configuration in case program fails.
    Configuration.SaveConfiguration();

    if (BackgroundWorker.IsBusy)
    {// End measurement.

        // Stop fade, enable monitor measurement, and cancel
        // processes.
        SetMeasureFade(false);
        BackgroundWorker.CancelAsync();
        btn_MeasureMonitor.Enabled = true;
    }
    else
    {// Start measurement.

        // If enabled, check save information.
        DialogResult result = DialogResult.Yes;
        if ((String.IsNullOrWhiteSpace(tb_SweepDescription.Text)
            || String.IsNullOrWhiteSpace(tb_SweepBias.Text))
            && Configuration.SweepCheckSave)
            result = MessageBox.Show("Are you sure you want to leave
                the description/bias blank?",
                "Save Information Check", MessageBoxButtons.YesNo,
                MessageBoxIcon.Question);

        if (result == DialogResult.Yes)
        {
            if (!Configuration.Overlay)
            {
                // Set initial axis ranges.
                minFrequency = Double.Parse(tb_FStart.Text) -
                    frequencyAxisClearance;
                maxFrequency = Double.Parse(tb_FEnd.Text) +
```

```
                    frequencyAxisClearance;
                horizontalSweep.Minimum = minFrequency;
                horizontalSweep.Maximum = maxFrequency;

                // Clear previous sweeps and associated data.
                currentSeries = 0;
                for (int i = 0; i < maxSeries; i++)
                {
                    for (int j = 0; j < measuredFreq.Length; j++)
                        measuredFreq[j] = 0;
                    tb_Stats.Text = "[ ]";
                    listBox.Items[i / 2] = "{ }";
                    ScatterSeries scatter =
                        seriesSweep[i] as ScatterSeries;
                    scatter.Points.Clear();
                    i++;
                    LineSeries line = seriesSweep[i] as LineSeries;
                    line.Points.Clear();
                }
            }

            // Update sweep plot.
            plotViewSweep.InvalidatePlot(true);

            // Create a new sweep file for measurement.
            if (createSweepFile)
            {
                Files.CreateNewSweepFile();
                createSweepFile = false;
            }

            // Disable monitor measurement, start fade, and initiate
            // measurement. Cannot have simultaneous measurements
            // (disable monitor).
            btn_MeasureMonitor.Enabled = false;
            SetMeasureFade(true);
            String[] arguments = new String[] { "sweep", tb_Amp.Text,
                tb_FStart.Text, tb_FStep.Text, tb_FEnd.Text };
            BackgroundWorker.RunWorkerAsync(arguments);
        }
    }
    // Focus away from the measurement button.
    panel1.Focus();
}

// Open the sweep configuration dialog.
private void Configure_Click(Object sender, EventArgs e)
{
    SweepConfigForm configForm = new SweepConfigForm();
    configForm.ShowDialog(this);
}
```

```
// Toggle the sweep continuous setting.
private void Continuous_Click(Object sender, EventArgs e)
{
    Configuration.Continuous = !Configuration.Continuous;
    if (Configuration.Continuous) btn_Continuous.BackColor =
        System.Drawing.Color.Thistle;
    else btn_Continuous.BackColor =
        System.Drawing.SystemColors.Control;
}

// Toggle the sweep save setting.
private void SaveSweep_Click(Object sender, EventArgs e)
{
    Configuration.SaveSweep = !Configuration.SaveSweep;
    if (Configuration.SaveSweep)
    {
        btn_SaveSweep.BackColor = System.Drawing.Color.Thistle;

        // Every toggle creates a new sweep file.
        Files.CreateNewSweepFile();
    }
    else btn_SaveSweep.BackColor =
        System.Drawing.SystemColors.Control;
}

// Toggle the sweep overlay setting.
private void Overlay_Click(Object sender, EventArgs e)
{
    Configuration.Overlay = !Configuration.Overlay;
    if (Configuration.Overlay)
        btn_Overlay.BackColor = System.Drawing.Color.Thistle;
    else
    {
        // Clear the previous overlay data.
        for (int i = 0; i < maxSeries; i++)
        {
            listBox.Items[i / 2] = "{ }";
            tb_Stats.Text = "[ ]";
            ScatterSeries scatter = seriesSweep[i] as ScatterSeries;
            scatter.Points.Clear();
            i++;
            LineSeries line = seriesSweep[i] as LineSeries;
            line.Points.Clear();
        }
        plotViewSweep.InvalidatePlot(true);
        btn_Overlay.BackColor = System.Drawing.SystemColors.Control;
    }
}
```

```
//
// FORM METHODS FOR MONITOR MEASUREMENT
//

// Handle the monitor measurement button click.
private void btn_MeasureMonitor_Click(Object sender, EventArgs e)
{
    // Save configuration in case program fails.
    Configuration.SaveConfiguration();

    if (BackgroundWorker.IsBusy)
    {// Stop measurement.

        // Stop fade, cancel processes, and enable sweep.
        SetMeasureFade(false);
        BackgroundWorker.CancelAsync();
        btn_MeasureSweep.Enabled = true;
    }
    else
    {// Start measurement.

        // If enabled, check save information.
        DialogResult result = DialogResult.Yes;
        if ((String.IsNullOrWhiteSpace(tb_MonitorDescription.Text)
            || String.IsNullOrWhiteSpace(tb_MonitorBias.Text))
            && Configuration.MonitorCheckSave)
            result = MessageBox.Show("Are you sure you want to leave
                the description/bias blank?",
                "Save Information Check", MessageBoxButtons.YesNo,
                MessageBoxIcon.Question);

        if (result == DialogResult.Yes)
        {
            // Clear the previous plot data.
            seriesMonitor.Points.Clear();
            plotViewMonitor.InvalidatePlot(true);

            // Create new monitor file for every measurement if set.
            if (Configuration.SaveMonitor)
                Files.CreateNewMonitorFile(
                tb_MonitorDescription.Text, tb_MonitorBias.Text);

            // Start fade, disable sweep, and initiate measurement.
            // Cannot have simultaneous measurements (disable sweep).
            btn_MeasureSweep.Enabled = false;
            SetMeasureFade(true);
            String[] arguments =
                new String[] { "monitor", tb_IntervalMonitor.Text };
            BackgroundWorker.RunWorkerAsync(arguments);
        }
    }
    // Focus away from the measure button.
    panel4.Focus();
}
```

```
// Toggle the save monitor option.
private void btn_SaveMonitor_Click(Object sender, EventArgs e)
{
    Configuration.SaveMonitor = !Configuration.SaveMonitor;
    if (Configuration.SaveMonitor)
    {
        btn_SaveMonitor.BackColor = System.Drawing.Color.Thistle;
        // A new file is created for every measurement since
        // measurements can acquire large datasets.
    }
    else btn_SaveMonitor.BackColor =
             System.Drawing.SystemColors.Control;
}

// Open monitor configuration dialog.
private void btn_ConfigMonitor_Click(Object sender, EventArgs e)
{
    MonitorConfigForm configForm = new MonitorConfigForm();
    configForm.ShowDialog(this);
}

//
// SHARED GUI METHODS
//

// Check if measurement should be enabled, based on instrument
// initialization.
public void EnableMeasurement()
{
    // Only the required instruments are required for a particular
    // measurement.

    // Check sweep measurement.
    if (Generator.State && Acquisition.State)
        btn_MeasureSweep.Enabled = true;
    else
        btn_MeasureSweep.Enabled = false;

    // Check monitor measurement.
    if (Counter.State)
        btn_MeasureMonitor.Enabled = true;
    else
        btn_MeasureMonitor.Enabled = false;
}

private void MainForm_Closing(Object sender,
    System.ComponentModel.CancelEventArgs e)
{
    // Update the configuration with field values.
    Configuration.Amplitude = Double.Parse(tb_Amp.Text);
    Configuration.StartFrequency = Double.Parse(tb_FStart.Text);
    Configuration.StepFrequency = Double.Parse(tb_FStep.Text);
    Configuration.EndFrequency = Double.Parse(tb_FEnd.Text);
```

```
            Configuration.DriftFactor = Int32.Parse(tb_Drift.Text);
            Configuration.MonitorInterval =
                Int32.Parse(tb_IntervalMonitor.Text);

            // Save the configuration.
            Configuration.SaveConfiguration();

            backForm.Close();
        }
    }
}
```

```
using System;

namespace SetupControl
{
    // This class orchestrates sweep measurements.
    static class SweepMeasurement
    {
        // allowed number of measurement failures
        static int maximumFailures = 3;

        // Produce test data for measurement simulation.
        private static Double[][] CreateData(Double increment)
        {
            Double[][] testData = new Double[6][];
            testData[0] = new Double[] { 215, 0.0632946 };
            testData[1] = new Double[] { 217, 0.167324 };
            testData[2] = new Double[] { 219, 0.216017 };
            testData[3] = new Double[] { 221, 0.168621 };
            testData[4] = new Double[] { 223, 0.109385 };
            testData[5] = new Double[] { 225, 0.0653981 };

            for(int i = 0; i < testData.Length; i++)
            {
                testData[i][0] += increment;
            }
            return testData;
        }

        // Conduct test measurement with simulation data.
        public static Double[][] TestMeasure(Double increment)
        {
            // Generate test data.
            Double[][] testData = CreateData(increment);

            for (int i = 0; i < testData.Length; i++)
            {
                // Simulate a measurement delay.
                System.Threading.Thread.Sleep(300);
                // Break if error or measurement has stopped.
                if (Program.MainHandle.ReportDataSweep(testData[i][0],
```

```
                testData[i][1]))
                    break;
        }
        return testData;
    }

    // Conduct an amplitude measurement.
    private static Double PerformMeasurement()
    {
        // The min/max values set the range for viable measurement data.
        Double minValue = 0.0;
        Double maxValue = 500.0;
        int minimumPoints = Configuration.SampleNumber;

        int point = 0;
        Double total = 0.0;
        int failure = 0;

        // Take specified # of measurements or until maximum failures.
        while (point < minimumPoints && failure < maximumFailures)
        {
            try
            {
                // Read data from the ADC.
                Double measured = Acquisition.ReadData();
                if (measured > minValue && measured < maxValue)
                {
                    // Add measured value.
                    total += measured;
                    point++;
                }
            }
            catch { failure++; }
        }
        // Return the averaged amplitude measurement.
        return total / point;
    }

    // Main function for sweep measurement.
    public static Double[][] Measure(String[] parameters)
    {
        // Load measurement parameters and settings.
        String vAmp = parameters[0];
        Double fStart = Double.Parse(parameters[1]) * 1000.0;
        Double fStep = Double.Parse(parameters[2]) * 1000.0;
        Double fEnd = Double.Parse(parameters[3]) * 1000.0;

        // Calculate number of data points and reserve memory.
        int dataPoints =
            (int)Math.Ceiling((fEnd - fStart) / fStep + 1.0);
        Double[][] measuredData = new Double[dataPoints][];

        // Initialize the function generator.
        Generator.SetRemoteControl();
```

```
            Generator.SetWaveFunction("SIN");
            Generator.SetVoltageOffset("0");

            // Perform measurement calibration.
            Generator.SetAmplitude("0.001"); // Remove driving signal.
            System.Threading.Thread.Sleep(500); // Wait for stabilization.
            Double calibration =
                PerformMeasurement(); // Measure calibration data.

            // Set generator amplitude.
            Generator.SetAmplitude(vAmp);
            System.Threading.Thread.Sleep(500); // Wait for stabilization.

            Double fCurrent = fStart;
            int j = 0;
            while (fCurrent <= fEnd)
            {
                // Set the generator to the current frequency.
                Generator.SetFrequency(fCurrent.ToString());

                // Record the current frequency.
                measuredData[j] = new Double[2];
                measuredData[j][0] = fCurrent/1000;
                System.Threading.Thread.Sleep(100); // Stabilize.

                // Perform an amplitude measurement and calibrate.
                Double data = PerformMeasurement();
                measuredData[j][1] = data - calibration;

                fCurrent += fStep;
                // If the measurement is ending (user initiated), then break.
                if (Program.MainHandle.ReportDataSweep(measuredData[j][0],
                    measuredData[j][1]))
                        break;
                j++;
            }
            return measuredData;
        }
    }
}
```

```
using System;
using System.IO.Ports;
using System.Windows.Forms;

namespace SetupControl
{
    // This class interacts with ADC peripherals devices.
    static class Acquisition
    {
        private static SerialPort SerialPort;
        public static bool State; // initialization state
```

```
private static int measurements = 5; // # of measurements to average
private static int failures = 5; // allowed # of failed measurements

// Initialize() must be called to open necessary ports and
// connect with ADC devices.
public static bool Initialize()
{
    SerialPort = new SerialPort();

    SerialPort.PortName = Configuration.ADCPort;
    SerialPort.BaudRate = 9600;
    SerialPort.Parity = System.IO.Ports.Parity.None;
    SerialPort.DataBits = 8;
    SerialPort.StopBits = System.IO.Ports.StopBits.One;
    SerialPort.Handshake = System.IO.Ports.Handshake.None;
    SerialPort.ReadTimeout = 1000;
    SerialPort.WriteTimeout = 1000;

    // Try to open the serial port (which will fail if no ADC device
    // exists on the port).
    try
    {
        SerialPort.Open();
        State = true;
        return true;
    }
    catch
    {
        MessageBox.Show("ADC initialization failed. Please check that
            it is turned on and connected.", "ADC Error",
            MessageBoxButtons.OK, MessageBoxIcon.Warning);
        State = false;
        return false;
    }
}

// ReInitialize() reopens ADC connections if settings have changed.
public static bool ReInitialize()
{
    // Try to open the serial port (which will fail if no ADC device
    // exists on the port).
    try
    {
        if (SerialPort.IsOpen) SerialPort.Close();
        SerialPort.PortName = Configuration.ADCPort;
        SerialPort.Open();
        State = true;
        return true;
    }
    catch
    {
        MessageBox.Show("ADC initialization failed. Please check that
            it is turned on and connected.", "ADC Error",
```

```
                    MessageBoxButtons.OK, MessageBoxIcon.Warning);
                State = false;
                return false;
            }
        }

        // Read data from the ADC.
        public static Double ReadData()
        {
            int i = 0;
            Double dataIn = 0;

            // Clear the buffer to remove old, backed-up data.
            SerialPort.DiscardInBuffer();

            // Acquire the configured number of measurements.
            // After the preconfigured number of failures, the measurement
            // will terminate.
            while (i < measurements)
            {
                try
                {
                    // Read/add the next measurement from the serial port.
                    dataIn += Double.Parse(SerialPort.ReadLine());
                    i++;
                }
                catch {
                    failures--;
                    if (failures <= 0)
                    {
                        throw new Exception("ADC measurement failed.");
                    }
                }
            }
            // Return the averaged measurement reading.
            return dataIn / measurements;
        }

        // Close the serial port.
        public static void Dispose()
        {
            SerialPort.Close();
        }
    }
}
```

```
using NationalInstruments.Visa;
using Ivi.Visa;
using System.Windows.Forms;

namespace SetupControl
{
    // This class interacts with the function generator.
    static class Generator
    {
        // GPIB communication uses a message based session.
        private static MessageBasedSession session;
        private static IMessageBasedFormattedIO iMsg;
        public static bool State; // initialization state

        // Initialize the GPIB interface.
        public static bool Initialize()
        {
            // Try to communicate with the function generator.
            try
            {
                session = new GpibSession(Configuration.GeneratorAddress);
                iMsg = session.FormattedIO;
                State = true;
                return true;
            }
            catch
            {
                MessageBox.Show("Function Generator initialization failed.
                    Please check that it is turned on and connected.",
                    "Function Generator Error", MessageBoxButtons.OK,
                    MessageBoxIcon.Warning);
                State = false;
                return false;
            }
        }

        // Assert remote control over generator.
        public static void SetRemoteControl()
        {
            iMsg.WriteLine("SYST:REM;");
        }

        // Set the output wave function (typical: SIN).
        public static void SetWaveFunction(String func)
        {
            iMsg.WriteLine("FUNCT " + func);
        }

        // Set the voltage offset value (V).
        public static void SetVoltageOffset(String offset)
        {
            iMsg.WriteLine("VOLT:OFFS " + offset);
        }
```

```
        // Set the amplitude (Vpp).
        public static void SetAmplitude(String amplitude)
        {
            iMsg.WriteLine("VOLT " + amplitude);
        }

        // Set the frequency (Hz).
        public static void SetFrequency(String frequency)
        {
            iMsg.WriteLine("FREQ " + frequency);
        }
    }
}
```

```
using System;
using System.IO.Ports;
using System.Windows.Forms;

namespace SetupControl
{
    // This class handles interactions with the frequency counter.
    class Counter
    {
        private static SerialPort SerialPort;
        public static bool State; // initialization state

        private static int timeout = 5; // measurement timeout (seconds)
        private static int readbytes = 15; // # of bytes in counter message

        // Test data for simulating measurements.
        static int testIndex = -1;
        static String[] testData = new String[] {
            "313.000 kHz",
            "314.000 kHz",
            "315.000 kHz",
            "311.000 kHz",
            "312.000 kHz",
            "317.000 kHz",
            "316.000 kHz",
            "310.000 kHz",
            "312.000 kHz"
        };

        // Initialize() must be called to open necessary ports and
        // connect with the frequency counter.
        public static bool Initialize()
        {
            SerialPort = new SerialPort();

            SerialPort.PortName = Configuration.CounterPort;
            SerialPort.BaudRate = 9600;
            SerialPort.Parity = System.IO.Ports.Parity.None;
```

```
        SerialPort.DataBits = 8;
        SerialPort.StopBits = System.IO.Ports.StopBits.One;
        SerialPort.Handshake = System.IO.Ports.Handshake.None;
        SerialPort.RtsEnable = false;
        SerialPort.DtrEnable = true;

        SerialPort.ReadTimeout = 10000;
        SerialPort.WriteTimeout = 10000;

        // Try to open the serial port (which will fail if no counter
        // exists on the port).
        try
        {
            SerialPort.Open();
            State = true;
            return true;
        }
        catch
        {
            MessageBox.Show("Frequency Counter initialization failed.
                Please check that it is turned on and connected.",
                "Frequency Counter Error", MessageBoxButtons.OK,
                MessageBoxIcon.Warning);
            State = false;
            return false;
        }
    }

    // Method returns sequential test data for measurement simulation.
    private static String TestData()
    {
        testIndex++;
        if (testIndex >= testData.Length) testIndex = 0;
        return testData[testIndex];
    }

    // Read the current frequency on the counter.
    public static Double ReadFrequency()
    {
        byte[] received = new byte[16]; // for incoming frequency data
        byte[] send = new byte[] {
            (byte)'D', 0x0D
        }; // outgoing measurement command

        // Send frequency read command.
        SerialPort.Write(send, 0, send.Length);

        DateTime start = DateTime.Now;
        int i = 0;

        // Read neccessary number of bytes or reach timeout condition.
        while(DateTime.Now.Subtract(start).TotalSeconds < timeout &&
            i < readbytes)
        {
```

```
                while(SerialPort.BytesToRead > 0)
                {
                    // Read the next byte from the counter.
                    received[i] = (byte) SerialPort.ReadByte();
                    i++;
                }
            }
            // Decode the measurement from counter byte array and parse.
            String frequency =
                System.Text.Encoding.Default.GetString(received);
            return Double.Parse(frequency.Split()[0]);
        }

        // Re-initialize the counter interface if settings have changed.
        public static bool ReInitialize()
        {
            // Try to open the serial port (which will fail if no counter
            // exists on the port).
            try
            {
                if (SerialPort.IsOpen) SerialPort.Close();
                SerialPort.PortName = Configuration.CounterPort;
                SerialPort.Open();
                State = true;
                return true;
            }
            catch
            {
                MessageBox.Show("Frequency Counter initialization failed.
                    Please check that it is turned on and connected.",
                    "Frequency Counter Error", MessageBoxButtons.OK,
                    MessageBoxIcon.Warning);
                State = false;
                return false;
            }
        }

        // Close the serial port.
        public static void Dispose()
        {
            SerialPort.Close();
        }
    }
}
```

```
using System;

namespace SetupControl
{
    // This class processes the sweep measurement data.
    static class Processing
    {
        // This calculation fits the sweep measurement data with the
        // equation for damped harmonic oscillation for a better
        // representation of both the resonant frequency and the
        // quality factor.

        // Define model parameters.
        static Double epsx = 0.00000001;
        static int maxits = 0;

        static int steps = 50; // number calculated points for fit

        // Evaluate the harmonic oscillator equation with c as parameters and
        // rawData as the data for fit.
        public static Double[][] EvaluateFunction(Double[] c,
            Double[][] rawData)
        {
            // Calculate frequency span and step value.
            Double span = rawData[rawData.Length - 1][0] - rawData[0][0];
            Double step = span / steps;
            Double current = rawData[0][0];

            Double[][] data = new Double[steps + 1][];
            for (int i = 0; i < steps + 1; i++)
            {
                // Create new (frequency, amplitude) data point.
                data[i] = new Double[2];
                data[i][0] = current;
                // Evaluate.
                data[i][1] = c[2] * Math.Pow(c[0], 2) /
                    Math.Sqrt(Math.Pow(Math.Pow(c[0], 2) -
                    Math.Pow(data[i][0] * 1000.0, 2), 2) +
                   (Math.Pow(data[i][0] * 1000.0 * c[0] / c[1], 2)));
                current += step;
            }
            return data;
        }

        // Definition of the harmonic oscillator function.
        private static void function(Double[] c, Double[] x, ref Double func,
            Object obj)
        {
            func = c[2] * Math.Pow(c[0], 2) /
                Math.Sqrt(Math.Pow(Math.Pow(c[0], 2) - Math.Pow(x[0], 2), 2)
                + (Math.Pow(x[0] * c[0] / c[1], 2)));
        }
```

```
// Definition of the derivative of the harmonic oscillator function.
private static void gradient(Double[] c, Double[] x, ref Double func,
    Double[] grad, Object obj)
{
    Double F = c[2] * Math.Pow(c[0], 2);
    Double G = Math.Sqrt(Math.Pow(Math.Pow(c[0], 2) -
        Math.Pow(x[0], 2), 2) + (Math.Pow(x[0] * c[0] / c[1], 2)));

    func = F / G;

    Double Fa = 2 * c[0] * c[2];
    Double Ga = 0.5 * Math.Pow(G, -1) * (4 * Math.Pow(c[0], 3) - 4 *
        c[0] * Math.Pow(x[0], 2) + (2 * c[0] *
        Math.Pow(x[0] / c[1], 2)));
    grad[0] = (G * Fa - F * Ga) / Math.Pow(G, 2);

    Double Gb = 0.5 * Math.Pow(G, -1) * (-2 *
        Math.Pow(c[0] * x[0], 2) / Math.Pow(c[1], 3));

    grad[1] = -1 * F * Gb / Math.Pow(G, 2);
    grad[2] = Math.Pow(c[0], 2) / G;
}

// Main method call for calculating data fit.
public static Double[] FitData(Double[][] data )
{
    // Set the fit initial values.
    Double[] c = new Double[] {
        Configuration.FitMinFrequency,
        Configuration.FitMinQ,
        Configuration.FitMinAmplitude };

    // Reserve memory for x and y arrays.
    Double[,] x = new Double[data.Length,1];
    Double[] y = new Double[data.Length];
    for (int i = 0; i < data.Length; i++)
    {
        if (data[i] != null)
        {
            // Load x and y values. (Convert kHz to Hz.)
            x[i, 0] = data[i][0] * 1000.0;
            y[i] = data[i][1];
        }
    }

    int info;
    alglib.lsfitstate state;
    alglib.lsfitreport rep;

    // Conduct a least-squares fit of the data.
    alglib.lsfitcreatefg(x, y, c, true, out state);
    alglib.lsfitsetbc(state,
        new Double[] {
            Configuration.FitMinFrequency,
```

```
                    Configuration.FitMinQ,
                    Configuration.FitMinAmplitude
                },
                new Double[] {
                    Configuration.FitMaxFrequency,
                    Configuration.FitMaxQ,
                    Configuration.FitMaxAmplitude });
            alglib.lsfitsetcond(state, epsx, maxits);
            alglib.lsfitfit(state, function, gradient, null, null);
            alglib.lsfitresults(state, out info, out c, out rep);

            // Output the results of the fit.
            Double[] outParam = new Double[4];
            outParam[0] = c[0]; // resonant frequency
            outParam[1] = c[1]; // quality factor
            outParam[2] = c[2]; // amplitude
            outParam[3] = rep.r2; // r-value of fit

            return outParam;
        }
    }
}
```

```
using System;
using System.Collections.Generic;
using System.IO;

namespace SetupControl
{
    // This class handles file interactions.
    static class Files
    {
        // Array parameters specify the layout in the config file.
        // {true}: parameter; {false}: blank space.
        static bool[] fileStruct;
        static String[] paramKeys;

        // Directory information for data export.
        static String configFile = "config.ini";
        static String currentSweepFile;
        static String currentMonitorFile;
        static String dataDirectory = "data";
        static String sweepDirectory = "sweep";
        static String monitorDirectory = "monitor";

        // Write the configuration to the config file.
        public static void WriteConfiguration()
        {
            // Retrieve the current configuration.
            Dictionary<String, String> currentConfiguration =
                Configuration.CurrentConfiguration;
            String[] output = new String[fileStruct.Length];
```

```
    int k = 0;
    for(int i = 0; i < fileStruct.Length; i++)
    {
        if (fileStruct[i])
        {
            // Save both the token and the parameter value.
            output[i] = paramKeys[k] + " " +
                currentConfiguration[paramKeys[k]];
            k++;
        }
        else output[i] = "";
    }

    // Write the output to file.
    System.IO.File.WriteAllLines(configFile, output);
}

// Read the configuration from file.
public static Dictionary<String, String> ReadConfiguration()
{
    // Pre-define parameter limit.
    int parameterNo = 50;

    System.IO.StreamReader file = new
        System.IO.StreamReader(configFile);
    int i = 0, k = 0;
    String line;
    String[] tempParamKeys = new String[parameterNo];
    bool[] tempFileStruct = new bool[parameterNo * 2];
    Dictionary<String, String> parameters =
        new Dictionary<String, String>();
    while((line = file.ReadLine()) != null)
    {
        // If file line is a parameter (not blank) save.
        tempFileStruct[i] = !String.IsNullOrWhiteSpace(line);
        if (tempFileStruct[i])
        {
            // Load both the token and parameter value.
            String[] item = line.Split();
            tempParamKeys[k] = item[0];
            parameters.Add(item[0], item[1]);
            k++;
        }
        i++;
    }
    file.Close();

    // Save a parameter list.
    paramKeys = new String[k];
    Array.Copy(tempParamKeys, paramKeys, k);

    // Save the file structure.
    fileStruct = new bool[i];
    Array.Copy(tempFileStruct, fileStruct, i);
```

```
    // Return parameter collection.
    return parameters;
}

// Create a new CSV file to save resonant frequency data.
public static void CreateNewMonitorFile(String description,
    String bias)
{
    currentMonitorFile =
        DateTime.Now.ToString("yyyy-MM-dd HH.mm.ss ") + "(" +
        description + ", " + bias + "V).csv";
    FileStream file = File.Create(dataDirectory + "\\" +
        monitorDirectory + "\\" + currentMonitorFile);
    file.Close();
    file.Dispose();
}

// Create a new CSV file to save the frequency sweep data.
public static void CreateNewSweepFile()
{
    currentSweepFile =
        DateTime.Now.ToString("yyyy-MM-dd HH.mm.ss") + ".csv";
    FileStream file = File.Create(dataDirectory + "\\" +
        sweepDirectory + "\\" + currentSweepFile);
    file.Close();
    file.Dispose();
}

// Save sweep data to the current sweep file.
public static void ExportSweepData(Double[][] data, Double[] fit,
    String description, String amplitude, String dc)
{
    String row1 = "";
    String row2 = "";
    String delim = ",";

    // Save measurement information.
    row1 += DateTime.Now.ToString("MM/dd/yyyy HH:mm:ss") + delim;
    row1 += description + delim;
    row1 += amplitude + delim;
    row1 += dc + delim;
    row2 += fit[0] + delim;
    row2 += fit[1] + delim;
    row2 += fit[3] + delim;
    row2 += delim;

    // Save the data.
    for (int i = 0; i < data.Length; i++)
    {
        row1 += data[i][0].ToString();
        row2 += data[i][1].ToString();
        if(i + 1 < data.Length)
        {
            row1 += delim;
```

```
                row2 += delim;
            }
        }

        // Append the new information/data to the current sweep file.
        StreamWriter sw =
            File.AppendText(dataDirectory + "\\" + sweepDirectory + "\\"
            + currentSweepFile);
        sw.WriteLine(row1);
        sw.WriteLine(row2);
        sw.Close();
        sw.Dispose();
    }

    // Append a resonant frequency data point.
    public static void ExportMonitorData(Double time, Double frequency)
    {
        StreamWriter sw = File.AppendText(dataDirectory + "\\" +
            monitorDirectory + "\\" + currentMonitorFile);
        sw.WriteLine(time.ToString() + "," + frequency.ToString());
        sw.Close();
        sw.Dispose();
    }
  }
}
```

```
using System;
using System.Collections.Generic;

namespace SetupControl
{
    // This class stores the current system configuration.
    static class Configuration
    {
        // Data structure for the current configuration.
        private static Dictionary<String, String> _currentConfiguration;

        public static Dictionary<String, String> CurrentConfiguration
        {
            get
            {
                // If Configuration isn't loaded, load...
                if (_currentConfiguration == null) LoadConfiguration();
                return _currentConfiguration;
            }
            set
            {
                _currentConfiguration = value;
            }
        }

        // GPIB address of the function generator.
```

```
public static String GeneratorAddress
{
    get { return _currentConfiguration["<GeneratorAddress>"]; }
    set { _currentConfiguration["<GeneratorAddress>"] =
            value.ToString(); }
}

// Serial port for the ADC device.
public static String ADCPort
{
    get { return _currentConfiguration["<ADCPort>"]; }
    set { _currentConfiguration["<ADCPort>"] = value.ToString(); }
}

// Serial port for the frequency counter.
public static String CounterPort
{
    get { return _currentConfiguration["<CounterPort>"]; }
    set { _currentConfiguration["<CounterPort>"] =
            value.ToString(); }
}

// Set the sweep drive amplitude.
public static Double Amplitude
{
    get { return
            Double.Parse(_currentConfiguration["<Amplitude>"]); }
    set { _currentConfiguration["<Amplitude>"] = value.ToString(); }
}
// Set the sweep start frequency.
public static Double StartFrequency
{
    get { return Double.Parse(
            _currentConfiguration["<StartFrequency>"]); }
    set { _currentConfiguration["<StartFrequency>"] =
            value.ToString(); }
}

// Set the sweep end frequency.
public static Double StepFrequency
{
    get { return Double.Parse(
            _currentConfiguration["<StepFrequency>"]); }
    set { _currentConfiguration["<StepFrequency>"] =
            value.ToString(); }
}

// Set the sweep end frequency.
public static Double EndFrequency
{
    get { return Double.Parse(
            _currentConfiguration["<EndFrequency>"]); }
    set { _currentConfiguration["<EndFrequency>"] =
            value.ToString(); }
```

```
}

// Set the sweep drift correction factor.
public static int DriftFactor
{
    get { return Int32.Parse(
              _currentConfiguration["<DriftFactor>"]); }
    set { _currentConfiguration["<DriftFactor>"] =
              value.ToString(); }
}

// Delay between consecutive sweep measurements.
public static int MeasurementDelay
{
    get { return Int32.Parse(
              _currentConfiguration["<MeasurementDelay>"]); }
    set { _currentConfiguration["<MeasurementDelay>"] =
              value.ToString(); }
}

// Number of samples for each frequency measurement.
public static int SampleNumber
{
    get { return Int32.Parse(
              _currentConfiguration["<SampleNumber>"]); }
    set { _currentConfiguration["<SampleNumber>"] =
              value.ToString(); }
}


// Continuously take frequency sweeps.
public static bool Continuous
{
    get { return Boolean.Parse(
              _currentConfiguration["<SweepContinuous>"]); }
    set { _currentConfiguration["<SweepContinuous>"] =
              value.ToString(); }
}

// Append sweeps to the figure.
public static bool Overlay
{
    get { return Boolean.Parse(
              _currentConfiguration["<SweepOverlay>"]); }
    set { _currentConfiguration["<SweepOverlay>"] =
              value.ToString(); }
}

// Save sweep measurements to file.
public static bool SaveSweep
{
    get { return Boolean.Parse(
              _currentConfiguration["<SweepSave>"]); }
    set { _currentConfiguration["<SweepSave>"] = value.ToString(); }
```

```
}

// Check sweep measurement information before saving data.
public static bool SweepCheckSave
{
    get { return Boolean.Parse(
              _currentConfiguration["<SweepCheckSave>"]); }
    set { _currentConfiguration["<SweepCheckSave>"] =
              value.ToString(); }
}

// Set the lower frequency bound for sweep fitting.
public static Double FitMinFrequency
{
    get { return Double.Parse(
              _currentConfiguration["<FitMinFrequency>"]); }
    set { _currentConfiguration["<FitMinFrequency>"] =
              value.ToString(); }
}

// Set the upper frequency bound for sweep fitting.
public static Double FitMaxFrequency
{
    get { return Double.Parse(
              _currentConfiguration["<FitMaxFrequency>"]); }
    set { _currentConfiguration["<FitMaxFrequency>"] =
              value.ToString(); }
}

// Set the lower Q bound for sweep fitting.
public static Double FitMinQ
{
    get { return Double.Parse(_currentConfiguration["<FitMinQ>"]); }
    set { _currentConfiguration["<FitMinQ>"] = value.ToString(); }
}

// Set the upper Q bound for sweep fitting.
public static Double FitMaxQ
{
    get { return Double.Parse(_currentConfiguration["<FitMaxQ>"]); }
    set { _currentConfiguration["<FitMaxQ>"] = value.ToString(); }
}

// Set the lower amplitude bound for sweep fitting.
public static Double FitMinAmplitude
{
    get { return Double.Parse(
              _currentConfiguration["<FitMinAmplitude>"]); }
    set { _currentConfiguration["<FitMinAmplitude>"] =
              value.ToString(); }
}

// Set the upper amplitude bound for sweep fitting.
public static Double FitMaxAmplitude
```

```
        {
            get { return Double.Parse(
                        _currentConfiguration["<FitMaxAmplitude>"]); }
            set { _currentConfiguration["<FitMaxAmplitude>"] =
                        value.ToString(); }
        }

        // Set the monitor interval for real-time frequency measurements.
        public static int MonitorInterval
        {
            get { return Int32.Parse(
                        _currentConfiguration["<MonitorInterval>"]); }
            set { _currentConfiguration["<MonitorInterval>"] =
                        value.ToString(); }
        }

        // Save monitor measurements to file.
        public static bool SaveMonitor
        {
            get{ return Boolean.Parse(
                      _currentConfiguration["<MonitorSave>"]); }
            set { _currentConfiguration["<MonitorSave>"] =
                     value.ToString(); }
        }

        // Check monitor measurement information before saving data.
        public static bool MonitorCheckSave
        {
            get { return Boolean.Parse(
                        _currentConfiguration["<MonitorCheckSave>"]); }
            set { _currentConfiguration["<MonitorCheckSave>"] =
                        value.ToString(); }
        }

        // Load the configuration from file.
        public static Dictionary<String, String> LoadConfiguration()
        {
            _currentConfiguration = Files.ReadConfiguration();
            return _currentConfiguration;
        }

        // Save the configuration to file if set.
        public static void SaveConfiguration()
        {
            if (_currentConfiguration != null) Files.WriteConfiguration();
        }
    }
}
```

```
using System;
using System.Windows.Forms;

namespace SetupControl
{
    // Main configuration form for monitor measurements/instruments.
    public partial class MonitorConfigForm : Form
    {
        public MonitorConfigForm()
        {
            InitializeComponent();

            // Retrieve configuration settings.
            tb_CounterPort.Text = Configuration.CounterPort;
            cb_CheckSave.CheckState = (CheckState)
                Convert.ToInt32(Configuration.MonitorCheckSave);
        }

        // Save the new configuration parameters and close Form.
        private void Save_Click(Object sender, EventArgs e)
        {
            // Store the new parameters.
            Configuration.CounterPort = tb_CounterPort.Text;
            Configuration.MonitorCheckSave =
                Convert.ToBoolean((int)cb_CheckSave.CheckState);
            // Save the configuration to the config file.
            Configuration.SaveConfiguration();
            // Re-initialize the external instrument connections.
            Counter.ReInitialize();
            // Re-check if measurement should be enabled.
            Program.MainHandle.EnableMeasurement();

            Close();
        }
    }
}
```

```
using System;
using System.Windows.Forms;

namespace SetupControl
{
    // Main configuration form for sweep measurements/instruments.
    public partial class SweepConfigForm : Form
    {
        public SweepConfigForm()
        {
            InitializeComponent();

            // Retrieve configuration settings.
            tb_GenAddress.Text = Configuration.GeneratorAddress;
            tb_SerialPort.Text = Configuration.ADCPort;
```

```
            tb_Delay.Text = Configuration.MeasurementDelay.ToString();
            tb_Samples.Text = Configuration.SampleNumber.ToString();
            cb_CheckSave.CheckState = (CheckState)
                Convert.ToInt32(Configuration.SweepCheckSave);
            tb_MinFreq.Text = Configuration.FitMinFrequency.ToString();
            tb_MaxFreq.Text = Configuration.FitMaxFrequency.ToString();
            tb_MinQ.Text = Configuration.FitMinQ.ToString();
            tb_MaxQ.Text = Configuration.FitMaxQ.ToString();
            tb_MinAmp.Text = Configuration.FitMinAmplitude.ToString();
            tb_MaxAmp.Text = Configuration.FitMaxAmplitude.ToString();
        }

        // Save the new cConfiguration parameters and close form.
        private void Save_Click(Object sender, EventArgs e)
        {
            // Store the new parameters.
            Configuration.GeneratorAddress = tb_GenAddress.Text;
            Configuration.ADCPort = tb_SerialPort.Text;
            Configuration.MeasurementDelay = Int32.Parse(tb_Delay.Text);
            Configuration.SampleNumber = Int32.Parse(tb_Samples.Text);
            Configuration.SweepCheckSave =
                Convert.ToBoolean((int)cb_CheckSave.CheckState);
            Configuration.FitMinFrequency = Double.Parse(tb_MinFreq.Text);
            Configuration.FitMaxFrequency = Double.Parse(tb_MaxFreq.Text);
            Configuration.FitMinQ = Double.Parse(tb_MinQ.Text);
            Configuration.FitMaxQ = Double.Parse(tb_MaxQ.Text);
            Configuration.FitMinAmplitude = Double.Parse(tb_MinAmp.Text);
            Configuration.FitMaxAmplitude = Double.Parse(tb_MaxAmp.Text);
            // Save the configuration to the config file.
            Configuration.SaveConfiguration();
            // Re-initialize the external instrument connections.
            Generator.Initialize();
            Acquisition.ReInitialize();
            // Re-check if measurement should be enabled.
            Program.MainHandle.EnableMeasurement();

            Close();
        }
    }
}
```

```
using System;
using System.Windows.Forms;

namespace SetupControl
{
    // The main entry point for the application.
    static class Program
    {
        // Serves as the public handle for the application form.
        public static MainForm MainHandle;

        [STAThread]
        static void Main()
        {
            Application.EnableVisualStyles();
            Application.SetCompatibleTextRenderingDefault(false);
            MainHandle = new MainForm();
            Application.Run(MainHandle);
        }
    }
}
```

```
using System.Windows.Forms;

namespace SetupControl
{
    // Form grays out other windows to dedicate resources to measurement.
    public partial class GrayOut : Form
    {
        public GrayOut()
        {
            InitializeComponent();
        }
    }
}
```

Vita

Ethan Keeler was a National Science Foundation (NSF) Graduate Research Fellow at the University of Washington (UW) where he earned a PhD, having studied electrical engineering, optics, and micro-systems. He also received a Master of Science, Electrical Engineering. During his tenure, he was president of the student chapter of the Optical Society (OSA), was a finalist for the Yang Research Award for the top electrical engineering PhD student, and has won several research presentation awards and travel grants.

Prior to seeking the weight of single cells and attending UW, Ethan completed a Bachelor of Science, Electrical Engineering, from Montana State University (MSU) where he worked to realize silicon-based near-infrared polarization devices on the nano-scale. These structures operated in reflection with promising compatibility with MEMS optical imaging devices. While at MSU, Ethan served as the chair of the MSU IEEE student branch and president of Tau Beta Pi (TBP). He was awarded the Montana Society of Engineers (MSE) Gold Medal Award for the top engineering student in his graduating class.

His next adventure takes him to Washington, DC, having been awarded an IEEE Congressional Fellowship to convey what he has learned throughout the course of his PhD to help members of Congress navigate pressing scientific and technological issues.